Microstructural Alterations of Commercial Metallic Alloys by Friction Surfacing

Von der Fakultät für Ingenieurwissenschaften, Abteilung Maschinenbau und
Verfahrenstechnik der
Universität Duisburg-Essen
zur Erlangung des akademischen Grades

einer

Doktorin der Ingenieurwissenschaften

Dr.-Ing.

genehmigte Dissertation

von

Stefanie Hanke
aus
Karlsruhe

Gutachter: Univ.-Prof. Dr.-Ing. Alfons Fischer
Univ.-Prof. Dr.-Ing. Stephan Huth
Tag der mündlichen Prüfung: 26.06.2014

Kurzfassung

Das Reibauftragschweißen ist in seinen Grundzügen bereits seit etwa 70 Jahren bekannt. Der Prozess ist dennoch nicht erschöpfend erforscht und wird selten industriell eingesetzt. Die zunehmende Knappheit von Energie und Ressourcen treibt aktuell die Auslotung alternativer Fertigungsmethoden voran, wodurch das Interesse am Reibauftragschweißen wieder belebt wurde. Die Vorteile des Prozesses sind dadurch bedingt, dass in der festen Phase gefügt wird. Die metallurgischen Vorgänge hierbei sind für die meisten Werkstoffe nicht untersucht. Ziel der vorliegenden Arbeit ist das Verständnis der Mikrostrukturentwicklung vier verschiedener Werkstoffe während des Reibauftragschweißens, sowie der daraus resultierenden Eigenschaften der Schichten unter tribologischer Beanspruchung. Hierfür wurden in erster Linie Elektronen-Mikroskopie und Verschleißprüfung herangezogen. Die untersuchten Werkstoffe sind die Aluminiumlegierung 6082, eine NiAl-Bronze (CuAl10Fe5Ni4), ein Werkzeugstahl (≈X50CrMoV5-1) sowie die Legierung Cr60Ni40.

Die Aluminiumlegierung durchläuft dynamische und statische Rekristallisation. Da es sich um eine ausscheidungshärtende Legierung handelt, und die Temperaturen beim Reibauftragschweißen nicht mit denjenigen einer gezielten Wärmebehandlung übereinstimmen, wirkt sich der Prozess negativ auf die Schichthärte aus. Die übrigen drei Werkstoffe durchlaufen wesentliche Phasenumwandlungen. Die Bronze nimmt bei der erreichten Temperatur eine krz Struktur an, aus welcher beim Abkühlen kleine globulare und nadelförmige kfz α Körner kristallisieren, gefolgt von der löslichkeitsbedingten Ausscheidung globularer κ-Phasen. Der Werkzeugstahl erreicht den kfz Austenit-Zustand, mit anschließender martensitischer Umwandlung während des Abkühlens. Beim Auftragen mehrerer überlappender Lagen wurden sowohl Anlass-, als auch Sekundärhärtungsvorgänge beobachtet. Die als nicht schweiß- und umformbar geltende Legierung Cr60Ni40 besteht während des Prozesses aus einer Cr- und einer Ni-reichen Phase. In den Schichten existieren anschließend ein übersättigter kfz Mischkristall und eine Cr-reiche krz Phase mit feinen Ni-Ausscheidungen. Die Übersättigung von Mischkristallen, eine Einformung von Phasen und Kornfeinung durch Rekristallisation wirken sich bei allen untersuchten Werkstoffen positiv auf die Verschleißbeständigkeit unter Kavitation aus. In Gleitverschleißuntersuchungen zeigen die Schichten ein vergleichbares Verhalten wie der jeweilige konventionelle Werkstoffzustand.

Für die Anwendbarkeit des Reibauftragschweißens sind die Materialeigenschaften bei den erhöhten Prozesstemperaturen relevant. Insbesondere muss es möglich sein, ein ausreichendes Materialvolumen in der Pinspitze zu plastifizieren. Ist dies der Fall, eröffnet das Reibauftragschweißen Möglichkeiten neuartiger Materialkombinationen, sowie Beschichtungen mit einer im Vergleich zum konventionellen Auftragschweißen vorteilhaften Mikrostruktur.

Abstract

The process of friction surfacing has been known in its basic arrangement for around 70 years, but only a limited amount of scientific studies has been carried out, and industrial use is marginal. Lately, the emerging shortness of energy and resources draws attention to alternative production routes, and interest in the friction surfacing process has revived. The process' advantages base on the fact that the deposited material does not undergo the liquid state, but instead is "forged" onto the substrate. Little is understood of the metallurgical mechanisms involved.
This work aims at revealing some of these mechanisms by electron-microscopy investigations, and at evaluating the microstructure resulting from friction surfacing as to the coatings' behaviour under tribological loading. The materials tested are 6082 aluminium alloy, NiAl-bronze (CuAl10Fe5Ni4), tool steel (≈X50CrMoV5-1) and the alloy Cr60Ni40.

The aluminium alloy, which is most easily processed by friction surfacing, undergoes dynamic and static recovery. It is a precipitation hardening alloy, and since the temperatures occurring during friction surfacing do not match the thermal sequence for artificial ageing, the material's hardness is adversely affected. The other three alloys undergo major phase transformations during processing. The bronze assumes a high temperature bcc structure while being deposited. During cooling, small globular or acicular fcc α grains crystallise, followed by precipitation of second (κ-) phases in spherical shape, due to decreasing solubility. The tool steel completely converts into its fcc austenite state, followed by martensitic transformation during cooling. When several layers are deposited overlapping each other, both tempering and secondary hardening effects arise. The non weldable and non deformable Cr60Ni40 alloy consists of a Cr- and a Ni-rich phase during processing. In the coatings, an fcc supersaturated solid solution and a bcc phase rich in Cr, incorporating fine Ni-precipitates, prevail.
Supersaturation of solid solution, spheroidisation of second phases and low grain size due to recrystallisation were found to be very beneficial for the wear resistance of all alloys against surface fatigue under cavitation. Sliding wear tests revealed comparable behaviour of the conventional and the friction surfaced material state.

For the feasibility of friction surfacing, a material's properties at the temperatures reached during the process are essential. In particular, it must be possible to transfer a sufficient volume of stud tip material into an adequate plasticised state. This opens up possibilities to join novel material combinations and achieve coatings with advantageous microstructures compared to conventional techniques.

Table of Contents

1 Introduction

Technological developments are commonly driven by the ambition to save resources; particularly materials, energy, time and costs. In the field of materials science this does not necessarily mean the development of new materials, but rather the improvement of properties and functionality of components by changing available materials' structures.

The desire to design more lightweight structural components for example initiated the development of new joining techniques and a more sophisticated design, matching precisely the loading at each location of a component. Such developments are, amongst others, the introduction of thermal spraying techniques to apply thin layers of wear resistant steel to cylinder liners in aluminium automotive engines, replacing the thicker bulk inserts from grey cast iron that are used otherwise [1] [2], or the invention of tailored blanks [3] [4]. Thermomechanical production techniques aim at generating an advantageous microstructure for the intended application already during forming, thus avoiding additional heat treatments, for example ausforming [5] or hot pressing [6]. Similarly, a current focus in research is the optimization of surface finishing in the last production step, influencing the surface material's structure in a way that leads to a reduction or prevention of wear of components during run-in [7].

In the process of friction surfacing, as well as in related processes like friction stir processing or friction stir welding, thermomechanical processing is deployed to join materials and/or to change their properties by “stirring” them around in a plastified, but not yet liquid state. This combines the two advantages of achieving homogenisation and refinement of the microstructure through a high degree of shear deformation, and generating a joint without entering the liquid state and encountering the problems that come along with the latter (gas pores, necessity to confine liquid…) [8] [9] [10].

Solid state processes allow the joining of materials which are regarded to be difficult or not weldable by conventional techniques. Aluminium alloys are known to be problematic in welding due to their stable passive films, high thermal expansion and sensitivity to heat input with regards to their mechanical properties. NiAl-bronze is weldable, as is a 0.6 wt.% C tool steel, but being materials applied in the cast state, they inhibit a coarse and inhomogeneous microstructure containing significant amounts of carbides and other precipitates. During fusion welding, the material is remelted and considerable efforts are needed to avoid cracks and internal stresses, including pre-, intermediate and post-weld heat treatments. The lower heat input during friction surfacing, since the liquidus temperature is not reached, may allow to omit some or all of the additional heat treatment steps when components from such cast materials need to be surface welded for repairing or for geometry adjustments. In addition, a refined microstructure with improved wear and fatigue properties can be expected from the thermomechanical processing. The high-temperature alloy Cr60Ni40 is regarded to be non weldable, due to its brittleness. Its application as a hard, high-temperature wear and corrosion resistant coating on a more ductile substrate would allow to design components with a functional Cr60Ni40 surface on a bulk material less brittle or prone to fatigue failure.

In the present work, friction surfacing is applied to the four material types mentioned above, and the structure and properties of the coatings are discussed.

1.1 Friction Surfacing

Friction surfacing is a friction welding process which was first patented in 1941 [11], with which metal coatings can be applied in solid state. In particular some materials which are considered to be difficult to weld or even being non-weldable, can be surfaced onto self-mating and non self-mating substrates [12] [13] [14]. It was early recognised as a possibility to repair or recondition worn or damaged materials [15] and to produce coatings from difficult material combinations. Those combinations include the following: white cast iron on steel [16], Hastelloy, Stellite 6 and Inconel 625 on mild and austenitic stainless steel [17], HSS steels and MMCs (Al_2O_3/low alloy steel) on mild steel [18], producing MMCs by filled studs (H13 + ZrO_2/Al_2O_3) [19], steel on aluminium [20], HSS steel from powder methods for coating knife edges [21], Al on Al [22] as well as Mg on Mg [23].

1.1.1 Process Description

Friction surfacing is a solid-state joining method, in which the required heat is generated by friction and the bonding is achieved by an applied forging pressure. The single layer procedure begins with a pre-heating phase during which a rotating stud made from the coating material is pressed with a defined axial force onto the substrate to be coated. The friction in the contact causes heating of both stud and substrate material. When the heat flow into the system and the surroundings is adequate, the temperature maximum is located within the stud tip, and the acting frictional torque causes the thermally softened material to flow. Now, the relative motion between the rotating stud and substrate no longer occurs within the interface between them, but within a shear plane in the softened stud material, which is referred to in literature as “quasi-liquid layer” [24] [25] [26] [27]. When this state is reached, the welding phase starts by superimposing a transversal movement, either by guiding the rotating stud over the substrate, or by shifting the substrate’s position. Along the trajectory, part of the softened material from the stud tip is transferred onto the substrate and leaves a coating of a width similar to the stud diameter. This is not a continuous process, but it has been observed that discrete layers are deposited in slabs, each after a certain amount of stud rotations [27]. Since the soft material at the outer edge of the stud cannot carry the axial forging force, a lack of fusion is present in a narrow region along the edges of each coating layer, which is characteristic for friction surfacing. A portion of the soft material, from the periphery of the stud, is squeezed out of the contact zone by the axial force, and is pushed upwards around the stud forming a flash [15] [26] [28] [29].

A schematic presentation of the process is given in Figure 1. The length of a single coating layer is limited by the availability of coating material from the stud, i.e. the stud length, which may additionally be effectively reduced by the size of the flash, which can move up towards the stud clamping [26] [29] [30].

1.1.2 Process Characteristics

Thickness and width of the coating layer, as well as the bonding quality, are affected by the process parameters, most important axial force, rotational and translational speed. Additional factors like the surrounding temperature and atmosphere, cooling or heating measures also influence the outcome of the process [28] [29] [31] [32]. The effects of process parameters were discussed already by Tyayar in 1959 [24]. It was found that the efficiency of the process, i.e. the fraction of the stud actually deposited, changes with the rotational speed of the stud. Still, the parameters rotational speed, axial pressure and translational feed rate are interconnected, and a certain window exists only within which the process is stable. Particularly if the rotational speed is too high, the temperature of the plastified material within the stud tip gets too high, with the result that no bonding takes place [24] [32]. It is generally described

that within the range of parameters suitable to produce bonded coatings in a stable process, the efficiency (output) as well as the coatings' thickness and width decrease with increasing axial pressure and rotational speed. This tendency is found in [26] for stainless steel (SUS403; X10Cr13; 1.4006) on steel plates from a material denoted as SPCH1 in a parameter range of axial pressure (25-75 MPa), rotational speed (1500-5200 min^{-1}) and translational speed (3-12 mm/s), in [28] for AISI440C (X105CrMo17; 1.4125) stainless steel on low carbon structural steel (SM490A), using constant axial pressure of 49 MPa and translational speed of 1 mm/s and varying the rotational speed (600-2400 min^{-1}) and for aluminium coatings [22] (stud and substrate from 5052 alloy), for a parameter range of 20-40 MPa axial pressure, 16.7-50 min^{-1} rotational speed and 5-11 mm/s. Additionally, the ambient atmosphere plays a role. The pressure needed for sufficient bonding may be reduced by welding in vacuum, which at the same time increases the bond strength for a tool steel (0.95 wt.% C) on a mild steel plate since the formation of small oxide particles in the bond zone is inhibited [25]. When welding under water, it was found that the coatings are thinner and of greater width, while the efficiency of the process is higher and is hardly affected by the process parameters. For coating a low carbon structural steel (SM50C) with a martensitic stainless steel (AISI440C; X105CrMo17; 1.4125), using axial pressures of 25-75 MPa, rotational speeds of 800-2400 min^{-1} and translational speeds of 0.5-2 mm/s, the efficiency was up to four times higher when friction surfacing was conducted under water [29].
Coating layers can be applied on top of each other or in an overlapping manner, in order to obtain higher thickness or width [24] [25] [33].

The process of friction surfacing often results in a fine and homogeneous microstructure within the coating, since the material is applied in a quasi-solid state under a high degree of plastic deformation, followed by rapid cooling [12] [23] [30] [34] [35]. Since the process takes place under considerably high pressure and temperature, severe plastic deformation takes place followed by a steep cooling gradient. The overall relatively small heat input reduces the risk of cracking, burn-off losses or voids [15] [28].

1.2 Severe Plastic Deformation by Friction Surfacing

As mentioned earlier, friction surfacing is a solid-state process, during which the coating material is deformed at high temperatures and under a substantial normal pressure. Considering that each slab of stud material undergoes several rotations before it is transferred to the substrate, and assuming that the thickness of the plastified layer is comparable to the coating thickness, in the range of 1 mm or less for the materials presented, some analogies to the severe plastic deformation process of e.g. high-pressure torsion are recognizable, in which a disc shaped sample is clamped between two anvils and distorted by the rotation of one of them [36] [37].

1.2.1 Severe Plastic Deformation

Severe plastic deformation (SPD) processing refers to various deformation processes, which introduce very high strains to bulk samples under hydrostatic pressure and without significantly changing the overall sample dimensions or introducing defects (cracks, voids…). The aim of these processes lies in refining the grain structure to ultra-fine or nanometre grains, in order to use the advantages such fine structures can possess, e.g. increased strength, improved fatigue behaviour and the ability of superplastic flow due to grain boundary sliding in forming operations [38] [39] [40] [41]. Typical SPD processes (amongst others) include high-pressure torsion (HPT), equal channel angular pressing (ECAP), accumulative roll bonding (ARB) and hydrostatic extrusion (HE) [42] [43]. The common feature of these processes, which is the cause for the achieved grain refinement, is that dynamic restoration processes take place in the microstructure at high degrees of deformation under hydrostatic pressure, and particularly so at elevated temperatures. These processes are commonly summarized under the term dynamic recrystallization (DRX) [44]. To preserve the fine grained microstructure and particularly in order to investigate the crystallographic features of DRX, rapid quenching (e.g. using liquid nitrogen) is applied after SPD processing.

1.2.2 Dynamic Recrystallisation

As in static recrystallization (SRX), which takes place after plastic deformation of a material has been terminated, different modes and mechanisms can contribute to dynamic recrystallization (DRX). Analogous to the static situation, the main types to distinguish are discontinuous and continuous dynamic recrystallization [44] [45]. Discontinuous recrystallization occurs in two stages: nuclei formation by dislocation accumulation (recovery) followed by migration of grain boundaries into the surrounding deformed material. Continuous recrystallization on the other hand is really a form of strong material recovery which does not require an incubation stage and takes place homogeneously throughout the strained material. It does not involve migration of high-angle boundaries, but a continuous increase of lattice misorientiation of substructures formed by accumulated dislocations (e.g. cell structures) [45] [46]. The specific difference between the static and dynamic processes is that in the latter deformation carries on during the recrystallization process, leading to immediate new strains within the freshly formed crystals and with that to some differences in the kinetics and physical events underlying the process. Another effective difference due to the ongoing deformation during recrystallization in the dynamic situation becomes obvious when the processed materials are subjected to an additional annealing treatment after deformation. While static (discontinuous) recrystallization at the best will result in new grains of various sizes fairly free of dislocations, in samples that have undergone dynamic recrystallization during deformation the already existing grains will only undergo limited coarsening. Mechanisms found during subsequent annealing of such materials are dominated by recovery processes, mainly redistribution and annihilation of dislocations, leading to an increase of grain boundary misorientations [44] [45]. A schematic representation of the basic microstructural differences between the discussed deformation and recrystallization types according to [44] is given in Figure 2.

In SPD processes which allow monitoring of the according parameters, the onset of dynamic recrystallization may be determined by a drop in the torque or force needed to achieve the continuing deformation. In the earlier phase of deformation, strain hardening due to an increasing number of dislocations and other defects occurs, with a concurrent increase in flow stress needed for deformation [38] [39] [40]. In the case of discontinuous dynamic recrystallization (dDRX), the formation and accumulation of dislocations (recovery) will at some stage have introduced enough energy in the material to trigger recrystallization. The newly formed grains are initially free of defects and will undergo strain hardening again from the start. In the steady state, the flow stress is determined by a balance of strain hardening from deformation and softening due to recrystallization. The steady state stress may be constant if the rates of hardening and softening are in the same range, or it may be oscillating, e.g. if the introduction of deformation proceeds slower than the recrystallization grain growth rate (i.e. dislocations are consumed faster than they are generated) [38] [39]. Besides the process parameters, this behaviour depends also on the initial grain size of the processed material [44]. For continuous dynamic recrystallization (cDRX), also a decrease in flow stress may be found, but it does not oscillate and since recovery processes do not need an incubation time, the microstructural evolution is rather homogeneous throughout the sample and continuous in processing time [44].

1.2.2.1 Types of Dynamic Recrystallization

Whether dynamic recrystallization occurs, and by which mechanisms, depends on several factors. Obviously, higher strains and temperatures (relative to each material's melting point) will aid the onset and accelerate the progression of restoration processes. The applied strain rates also have an effect. The most relevant material properties are the lattice structure, the shear modulus, the stacking fault energy and the presence and type of both alloying atoms in solid solution as well as second phases [45] [47].

Generally, dynamic recrystallization takes place when dislocations and/or grain boundaries have the possibility to migrate during the deformation process. The driving force for this migration is generated from the lattice distortions caused by the introduced strain. Still, a certain activation energy must be provided, and the boundary or dislocation migration may be retarded by other features within the microstructure (e.g. hard second phases) [40] [42] [44].

Factors determining the discontinuous or continuous type of recrystallization can be traced back to the climb and cross-slip ability of dislocations within the crystals. In a material with low stacking fault energy (and therefore a large split distance of dislocations) in combination with a high shear modulus, the mobility of dislocations is very limited. If in addition foreign atoms in solid solution, or fine, dispersed second phases are present, the blocking of dislocation movement is further enhanced. Such materials have a very limited ability for recovery, will undergo distinct strain hardening, and when sufficient energy is available within the crystals, may recrystallize by dDRX, starting from nuclei of strain localization e.g. at bulged grain boundaries or deformation twins. Materials displaying this kind of behaviour are e.g. Cu, Ag and stainless steel [47] [48].

At high stacking fault energy, in materials with low shear modulus and possibly high purity, dislocations may move more freely and faster in reaction to the internal stresses from macroscopic deformation, and recovery can occur more easily. These materials form cell structures during deformation, which become more pronounced and develop sharper and denser cell walls with increasing strain. When the misorientation across cell walls of these sub structures attains values above ≈ 15°, they are identified as high-angle boundaries (HAB), and recrystallization by strong recovery (= cDRX) has taken place. This mechanism is typically found in aluminium alloys and bcc metals [44] [49] [50].

Due to the high number of influencing factors, local differences within one sample, the mixed occurrence or a transition between the above mentioned mechanisms within one material with changing processing parameters are possible [51].

1.2.2.2 Microstructure Evolution during Dynamic Recrystallization

The grain size obtained by SPD depends on the processing parameters as well as material properties. For a certain set of parameters, dynamic recrystallization results in a constant, stable grain size when a sufficient amount of strain has been introduced [44] [45].

The obtained size of grains depends again on the factors and mechanisms discussed above. In cDRX the grain size is fairly equal to the sub-grain structure formed by the dislocation cell structure, since grain boundary migration does not occur. So, at low deformation temperatures, high strain rates and the presence of alloying elements a high degree of strain hardening is obtained and the formed dislocation cells are small, which leads to a low stable grain size [45] [51]. In dDRX, the obtained stable grain size is also very sensitive to the applied strain rate and the deformation temperature, which can be easily correlated to the acting flow stress. If this value is high, the grain size may be expected to be low, since the balance of strain hardening and recrystallization softening is shifted towards the strain accumulation. This implies the presence of a high number of nuclei and as a result a higher fraction of small grains. The grain size in dDRX is typically not as uniform as in cDRX, due to the two-stage type of the process. Single grains may be in different states of their growth, being still small if they have formed recently, and larger and containing new dislocations at later stages of growth. For this reason, in materials undergoing dDRX substructures are usually smaller than the grains defined by HABs [44] [50].

Fine grains formed during SPD often exhibit grain boundaries with diffusive diffraction contrast in TEM, indicating their non-equilibrium state. High internal stresses are generated near grain boundaries during SPD, detectable by high-resolution TEM as an elastically distorted layer along them. The distorted crystallographic planes can be removed by static recovery during a subsequent heat treatment [44] [52]. In continuously recrystallized materials, only limited grain coarsening occurs during an additional heat treatment, which is dominated still by recovery mechanisms, in particular the transformation of the non-equilibrium grain boundaries into equilibrium ones. Materials which have undergone dDRX may show some rapid grain growth during an annealing treatment, since here the migration of HABs is possible, and no incubation stage to form nuclei for grain growth is needed, as is the case in the heat treatment of conventionally deformed materials [47].

If multiphase materials are treated by SPD, additional factors may influence the recrystallization behavior, and only few studies are available to this topic. While the above mentioned effects of solid solution elements and second phases hold true, phase transformations during the deformation can also accelerate recrystallization mechanisms, if they release additional energy. This depends on type, size, distribution (mean free path) of the second phases as well as the type of phase transformation taking place [38] [47] [53].

1.3 Wear Testing

1.3.1 Cavitation

Cavitation is a physical phenomenon caused by fluctuations of pressure in liquids, and therefore associated with components operating in or with agitated liquids, e.g. pumps, valves or propellers. Wear is brought about by gas bubbles forming when pressure falls below the vapour pressure, and imploding again on a components' surface [54]. Damage caused by cavitation usually begins with local plastic deformation of the material, where it is hit by such a micro jet. Small dimples are the result and with continuing loading the surface roughness increases. The progression of wear under cavitation loading strongly depends on a particular material's properties. Multiple impacts can lead to further severe plastic deformation, strain hardening, crack initiation and propagation, and finally loss of material [55]. Cavitation additionally influences a material's corrosion behaviour. Different mechanisms have been reported in this context, including the mechanical removal of the passive layer, differing erosion rates of phases with unequal electrochemical potential and corrosion fatigue [56] [57].

1.3.2 Sliding Wear

The deterioration of surfaces on contacting bodies which perform a relative motion tangential to each other is referred to as sliding wear [58]. In order to investigate the mechanisms which lead to changes and removal of the surface material, model tests with simple contact geometries are conducted under controlled laboratory conditions. In a pin-on-disc set-up, for example, the face of the pin slides along a circular path at a certain radius on the disc surface (unidirectional sliding). In a ball-on-flat design the motion includes changes in direction, when a tightly fixed ball slides in a bidirectional manner along a straight line on the flat counterbody (reciprocating sliding). Other contact geometries may be used as well (e.g. cylinders), considering the possibility to anticipate the dimensions and shape of the actual contact area, initially as well as with the onset of material removal. It must be born in mind that the real contact area is composed of the discrete contact points of the microscopic surface roughness peaks, and therefore is significantly smaller than the nominal contact area which is anticipated from the macroscopic sample geometry.

Each tribological system is defined by its components, which are the contacting bodies, lubricating and surrounding media as well as the type of relative movement and load [54].

It is generally accepted, that material deterioration due to wear can be accounted for by four major groups of mechanisms [54].

Adhesion

Adhesive wear is initiated by microscopic weldments between contacting peaks in the surface topography, due to high pressures and friction induced short temperature rise. With ongoing relative motion, the joints are torn apart and separation may occur outside the former contact surface, leading to transfer of material from one body to the other and a roughening of the surfaces. The repeated occurrence of such events may lead to strain hardening of the roughened surface which may initiate the onset of grooving (abrasion) and surface fatigue mechanisms [59].

Abrasion

The obvious wear appearance at the presence of abrasive wear are grooves, which are typically caused by the carving of a softer material through the roughness peaks of a harder surface. Material removal is brought about either directly by chipping, or by fatigue mechanisms if grooving takes place by plastic deformation and the repeated action causes strain hardening [59].

Surface Fatigue

Fatigue mechanisms in the surface and in the subsurface material can be caused by oscillating mechanical loads from e.g. a repeated sliding contact. Cracks may be initiated, typically underneath the surface in the depth of the highest shear stress caused by the friction force. Crack growth towards the surface leads to the delamination of flake shaped wear particles [59].

Tribochemical Wear (Tribooxidation)

The application of normal and friction forces induces energy into a material's surface, most easily understood as frictional heating. The energy, in combination with the removal of protective films and the initiation of fine cracks leads to an activation of the loaded surfaces which enforces the accelerated progression of chemical reactions with the surrounding media [59]. Tribochemical reaction layers usually consist of oxides or hydroxides which may by brittle and spall off during the ongoing tribological loading. On the other hand, stable tribochemical layers may aid the prevention of adhesive wear by separating the metal surfaces and avoiding a direct contact [59]. Lately it has been shown that thin surface films may have an effect on materials' mechanical reaction to the tribological load as well [60] [61].

In real life tribosystems, often several different wear mechanisms occur concurrently or in different regions on the same surface, due to the complex interactions within the systems.

Sliding wear of metallic bodies has been extensively studied. In [62] an overview of the observable wear appearances is given. In the beginning of the wear process, changes in surface topography are dominant (run-in). Without a lubricating medium, frequently adhesive material transfer between the surfaces is found, due to microscopic welds between roughness peaks, with subsequent breaking of the joints leading to a roughening of the surfaces. At the presence of an adequate lubricant on the other hand, a smoothening of the surfaces may take place by plastic flow or the removal of oxide films. If adhesion can be avoided in the ongoing wear progress, by lubrication or the formation of suitable tribochemical surface films, in many tribological systems a steady state with a low wear rate is reached, with material removal dominated by delamination of oxidized surface films or the discontinuous breaking off of particles by surface fatigue mechanisms [62] [63].

At high loads, in dependence of the testing (sliding speed, contact pressure…) and material parameters (hardness, deformation properties…) a transition between low, fatigue and chemically dominated wear, towards adhesion and grooving by abrasive mechanisms is possible in the steady state wear stage [64].

1.4 Aim of this Work

When applying coatings by friction surfacing, the microstructure of the obtained coatings can be expected to differ significantly for different materials. Amongst others, it will be influenced by the crystal structure of a material, its stacking fault energy, its initial state or any potential phase transformations initiated by the introduced strain and heat, including the final cooling.

The examined aluminium alloy has an fcc structure, which does not change at increased temperature until the melting range is reached. Still, it contains hardening precipitates, which react sensitively to temperature changes by dissolution as well as reprecipitation and growth.

The NiAl-bronze consists of an fcc solid solution phase and various types of precipitates at room temperature. The Cu-Al system contains a eutectic point at 567°C, which is slightly shifted by the addition of Ni and Fe in this alloy, and various domains predicting different combinations of second, partly intermetallic phases. The heat from friction surfacing will increase the temperature into a regime in the phase diagram, in which a bcc high-temperature phase is expected, but it is not sure whether the room temperature fcc phase will completely transform. So, in this alloy system deformation of one or two different types of solidus occurs, of which only one is stable after cooling to room temperature.

The tool steel is available in the soft annealed state before being processed by friction surfacing. It therefore contains bcc ferrite and a certain number of carbides. During processing, a transformation into fcc austenite with a significantly increased solubility for carbon is expected. In this state the deformation will take place, and during subsequent cooling, again phase transformations into phases stable at room temperatures will occur. These transformations will highly depend on the quenching, and with a decrease in cooling rate, martensite (with retained austenite), bainite (with cementite) or ferrite with newly distributed carbides may form.

The Cr-Ni system is a simple eutectic one. Similar phase transformations are expected for the Cr60Ni40 alloy, as for the NiAl-bronze, although in this case it is sure, that deformation will take place at a temperature well within the two-phase regime underneath the eutectic point. So, within the Cr60Ni40 alloy deformation is applied to both fcc Ni-dominated, and bcc Cr-dominated solid solution. At room temperature the solubility of Ni in bcc Cr reduces almost to zero, so the resulting microstructure in the coatings will also be affected significantly by the cooling rate, which determines possible diffusion processes. Additionally, this material is very brittle and not weldable or deformable by conventional methods without generating cracks.

To evaluate the strength and stability of materials processed by friction surfacing, wear tests were conducted, since the resistance to tribological loading is a significant property for coatings.

The aluminium alloy 6082 is not intended for wear applications, it is rather a structural material, e.g. intended to be applied locally to reinforce mechanical stability in aircraft structures. Nonetheless, cavitation tests were conducted for a quick evaluation of mechanical as well as chemical/corrosive properties. Typical applications for the examined NiAl-bronze are ship propellers or pump components, for which cavitation is an expected type of loading. The tool steel CP4M/GP4M has its standard use as deformation tools, which undergo relative sliding to the steel sheets which are formed, so sliding wear testing was chosen for this material. Components from Cr60Ni40 alloy are installed e.g. in highly loaded engines or in refinery or combustion operations. Both relative sliding and surface fatigue by impacts on the surface may occur in such surroundings, the latter being particularly of interest for this brittle material. Both cavitation and sliding wear testing was conducted on this material.

The aim of this work is to disclose the microstructure alterations obtained in different materials by the thermomechanical process of friction surfacing, and to investigate and discuss the mechanisms through which these changes were attained. This includes the microstructural analysis as well as the discussion of possible deformation, restoration and phase transformation processes.

In addition, the consequences of these alterations for the applicability of the processed materials as functional coatings are demonstrated. Considering possible uses of the alloys, thermal stability and wear resistance are investigated and discussed in comparison to conventionally produced material.

2 Materials and Methods

2.1 Surfacing Materials

2.1.1 Aluminium Alloy 6082 (stud)

The main alloying elements in 6082 aluminium alloy (AlMgSi1Mn) are Silicon and Magnesium (composition acc. to [65] see Table 1) and it is regarded as weldable and suitable for corrosive environments. Its toughness can be increased by precipitation hardening, i.e. formation of Mg_2Si phase. Of the 6000-series alloys, 6082 is the most common one, because of its high toughness and good workability. Main areas of application are in food processing, mining, construction as well as automobile- and ship-building [66].

Generally, possible mechanisms to improve the mechanical properties of aluminium alloys are grain refinement, strain-, solid solution- and precipitation hardening, depending on alloy composition. In the alloy 6082, hardening is most efficiently achieved by a fine dispersion of coherent precipitates generated during a controlled ageing treatment after solution annealing at 10 – 20 K below the eutectic temperature (520 – 540°C) [67]. The solution annealing temperature and the quenching rate have a significant influence on occurring recovery and diffusion processes, which again affect the subsequent hardening behaviour. Size and distribution of precipitates – and with that mechanical properties - are determined by lattice defects present to serve as nuclei, and the ageing treatment temperature and time. Overageing is induced at high temperatures and long tempering times by growth and transformation of the fine coherent hardening precipitates into larger semi- or incoherent second phase platelets [68] [69]. Due to these complex interactions, a precise control of strain and temperature are required to attain the maximum possible hardness. While the alloying elements Mg and Si are important to form precipitates, Cu leads to solid solution hardening and is advantageous for high-temperature strength and creep resistance. However, due to its difference in electrochemical potential to the less noble Al, it is detrimental for the corrosion resistance of an alloy. This has the most potent effect if Cu-containing second phases are formed, e.g. during inadequate heat input, which may lead to the forming of local galvanic cells with the risk of pitting corrosion [67].

2024 (Substrate)
As substrate material the aluminium alloy 2024 (AlCu4Mg1) was used. Its main alloying element is Cu, which brings about good mechanical properties, including high strength and ductility, but is detrimental for the corrosion resistance. This alloy is applied in aircraft industry, particularly for structural components [66].

2.1.2 CuAl10Fe5Ni4 Bronze (stud and substrate)

Coatings were generated from the NiAl-bronze CuAl10Fe5Ni4 (CW307G; 2.0966), as used for maritime components and pumps, on self-mating substrate.
NiAl-bronzes are usually chosen for their good corrosion properties in sea water, their resistance against cavitation erosion (e.g. for ship propellers) and their sufficient mechanical properties. They contain up to

11 wt.% aluminium, and few percent nickel and iron (Table 2), which allows heat treatments comparable to those of steel [70].

Large parts are usually cast and exhibit an inhomogeneous microstructure containing fcc α-phase which is rich in copper, sometimes a bcc β-phase, and several types of precipitates (named κ_{I} through κ_{IV}), containing an increased amount of iron and / or nickel [71].

Different surface treatments have been investigated to improve material properties of the cast components. These include standard methods like laser, induction and flame hardening, which can all lead to improved resistance against corrosion and cavitation erosion. This improvement was on the one hand attributed to an increase in hardness and on the other hand to the achieved homogenisation of the microstructure. The beneficial effect of the latter was explained by the fact that material failure due to corrosion as well as cavitation erosion often begins at interfaces between different phases [72] [73] [74].

Friction stir processing, which generates a microstructure similar to the one of friction surfacing layers, has also been suggested for surface treatment of cast NiAl-bronze components. It was shown that the achieved homogeneity and the fine grained microstructure are advantageous for the mechanical properties of the bronze, and that small voids and casting defects near the surface can be closed [75].

For larger casting defects as well as worn or damaged surfaces, where new material has to be added, the above described methods are not applicable. Standard fusion welding methods have up to now been employed for repairing components, if at all possible. Adequate mechanical properties can be achieved, but typical additional measures, e.g. subsequent heat treatment and non-destructive testing to detect welding defects, are necessary [76] [77].

For such cases, friction surfacing could be a useful alternative, since it allows depositing material which immediately possesses a favourable microstructure. The possibility of welding under water could be an additional gain.

2.1.3 Tool Steel X50CrMoV5-1 / CP4M® (stud and substrate)

The cast cold work tool steel investigated in this study is provided by Doerrenberg Edelstahl GmbH, Engelskirchen, Germany under the brand name GP4M and is similar to X50CrMoV5-1 (1.2345). It has a high toughness and at the same time a good hardenability, which makes it suitable for highly loaded forming tools for high strength steel sheets. Its carbon content is 0.6 wt.% and it contains 5 wt.% chromium, as well as molybdenum and vanadium. At a tempering temperature of about 550°C secondary hardening up to 62 HRC can be obtained [78]. The studs from which the coatings were applied onto the cast and hardened substrate are from the same alloy, in the soft annealed state (brand name in wrought state: CP4M) with a hardness of 226 ± 3 HV10.

2.1.4 Cr60Ni40 Alloy (stud)

The alloys of Cr60Ni40-type (ASTM A560) inhibit an outstanding high-temperature corrosion resistance and, therefore, were applied in the past for refinery furnaces [79] and applications with comparable operational demands. They have a high strength, but are quite brittle due to the high Cr-content. Values required by the ASTM standard [80] for mechanical properties and chemical composition are given in Table 3. Cr60Ni40 is regarded to be non-deformable and non-weldable, therefore being only available as castings.

A second large field of applications for Cr-Ni alloys is as thin film resistors in microelectronics. For this reason, the structure and electrical properties of alloys with various Cr-Ni-ratios have been extensively studied in thin sputtered films, leading to the identification of several non-equilibrium phases [81] [82] [83] [84].

For the binary Chromium-Nickel system, usually three equilibrium solid state phases are denoted, being each fcc Ni- and bcc Cr-rich solid solutions as well as an ordered Ni_2Cr intermetallic phase below 590°C [81] [85]. A eutectic exists which is reported by different authors ranging from 46 to 49 wt.% Ni and 1327 to 1345°C [79] [85] [86]. A calculated phase diagram from [87] is presented in Figure 3. Additionally, several non-equilibrium phases are reported, most frequently identified as tetragonal σ-phase or cubic δ-phase. One reason for the multitude and the partly non-conclusive discussion of phases in Cr-rich Cr-Ni-alloys is the low solubility of Ni within Cr at room temperature. While at the eutectic temperature approximately 38 wt.% Ni can be dissolved, this value drops rapidly with temperature to 10 wt.% at 1075°C and 2 wt.% at 800°C, with a further decrease down to room temperature. Exact numbers for the solubility of Ni in Cr at room temperature are not given [81] [82] [83] [84] [85].

Nimonic 80A (substrate)

This high-temperature alloy contains about 70 wt.% Ni, 20 wt.% Cr and additions of < 3 wt.% of Ti, Al and Fe. Other denominations for this material are ASTM B 637 and 2.4631 or 2.4952.

2.2 Process Parameters for Friction Surfacing

A fully hydraulic driven (marine specification) stud welding machine type RH 3000 (Proserv Offshore Ltd., Kintore, UK) was used to prepare the coatings at Helmholtz Zentrum Geesthacht, Germany. The translational movement was realised by the machine table, which is operated by a spindle drive suitable for the high perpendicular loading from the process downforce.

Due to the overlaying rotational and translational movement, the process of friction surfacing is asymmetric. The directions of the relative movements of stud and substrate material either add up (retreating side) or oppose each other (advancing side). To produce multiple layers, overlapping was arranged at the advancing side of the coating in process.

The substrate was prepared for all surfacing trials by grinding with 120-grit abrasive paper to remove oxide films or scales, followed by degreasing with acetone.

At the beginning of the process, the rotating stud was pressed onto the substrate and kept for a certain period of time (1 to 2 min, depending on the material). In this period, the substrate was warmed by the frictional heat and the material in the stud tip was sufficiently plasticised. The latter was assessed by measuring the shortening of the stud under the applied pressure, which was 3 mm in the preheating phase.

The flash could not be removed during surfacing with the available equipment, so the maximum coating length possible was determined by the flash reaching the clamping of the stud, when the process had to be stopped.

6082 Aluminium Alloy

Coatings were generated from 6082 studs of 20 mm diameter on 2024 alloy substrate of 10 mm thickness. Process parameters chosen were 0.67 m/min traverse speed, 3500 min^{-1} rotational speed of the stud and an axial nominal pressure of 18.5 MPa. Only single layer coatings were investigated.

NiAl-Bronze

Friction surfacing was performed with studs of 20 mm diameter and 90 mm length, on plates having dimensions of 300 x 100 x 10 mm. Surfacing parameters were 0.3 m/min traverse speed, 50 MPa normal pressure and a rotational speed of the studs of 4000 min^{-1}. Single layer surfacing has been performed in air and submerged in tap water.

CP4M Tool Steel

The coating material was available in the soft annealed state, in studs of 90 mm length and 15.3 mm diameter. The material to be coated in the present study was in the cast and hardened state, cut into plates of 200 x 100 x 10 mm. For the surfacing process, the rotational speed of the studs was varied between 3500 and 4000 min^{-1} and the axial pressure was 109 MPa. Within a range of the transversal speed between 0.3 and 0.85 m/min, a smooth and stable process could be achieved.

The multilayer coatings were prepared with a rotation of 3500 min^{-1}, a transversal speed of 0.33 m/min, an overlap of 7 to 9 mm and partly with reduced axial pressure.

Cr60Ni40

For the coating process, sheets from Nimonic 80A alloy with a thickness of 10 mm were used as substrate material. The studs from Cr60Ni40 had a diameter of 20 mm. Single and multiple overlapping coatings were prepared, with a rotational speed of the studs of 3500 min^{-1} and a normal pressure of 50 MPa. The translational movement was then applied at a speed of 0.33 m/min. Wider coatings were produced by overlapping several layers with an offset of 10 mm.

An overview of the process parameters used to apply single layer coatings from the different materials is given in Table 4.

2.3 Wear Tests

A summary of all wear testing methods carried out in this work is presented in Table 5.

2.3.1 Cavitation

Cavitation testing was carried out following ASTM G 32-03 [88] with some modifications. In the set up a sample was fixed in a rigid holder and immersed into distilled water to a depth of 12 to 15 mm below water level. A double walled container was used in order to keep the water temperature at 25 ± 3°C by a cryostat (Haake K20, Fisons Instruments GmbH, Karlsruhe, Germany) throughout each experiment. An ultrasonic generator was used to excite a sonotrode to oscillate at 20 kHz with an amplitude of 19 µm during the experiments. The exchangeable flat tip of the sonotrode had a diameter of 16 mm and was positioned 0.5 mm above the sample. The fast oscillation of the sonotrode induces cavitation in the gap between the sample surface and the sonotrode tip. In this set-up, the sonotrode tip is exposed to the same loading as the sample, and therefore also experiences wear. The tips used in the present study are made from the stainless steel X13CrMnMoN18-14-3 (1.4452; “P2000”) and were replaced and refurbished after 6h of cavitation testing. Each experiment was run in certain intervals, after which the sample was removed from the test rig, cleaned with acetone in an ultrasonic cleaning bath, thoroughly dried and then weighed. Each weight measurement was repeated 5 times on a scale with a precision of 10^{-4} g (AC211S, Sartorius AG, Goettingen, Germany). Additionally, the wear appearances were investigated by scanning-electron-microscopy (SEM) and confocal white-light microscopy (CLM).

2.3.1.1 Sample Preparation from 6082

Single layer aluminium FS coatings in the as-coated state as well as after heat treatment were cut into samples of 20 x 20 mm dimensions, in order to fit into the cavitation test rig. They were carefully ground plane to remove the surface rings from the coating process, while ensuring coplanarity of the surface to the bottom of the sample. The test surface was then polished with a diamond suspension of 3 µm grain size, so that the surface was not mirror finished but left with shallow polishing marks. One as-coated and two heat treated samples were tested.

2.3.1.2 Sample Preparation from NiAl-Bronze

20 x 20 mm samples were cut from plates with a friction surfacing layer (Figure 5) as well as from uncoated substrate material. All samples were plane ground using 800-grit abrasive paper followed by polishing with diamond suspension with 3 µm grain size. Four samples with coatings and three from the as-cast material were tested.

2.3.1.3 Sample Preparation from Cr60Ni40

Samples for cavitation testing were prepared from cast and heat treated material as well as triple-layer Cr60Ni40 coatings. They were cut to sizes of about 25 x 25 mm, and 10 mm thickness. All samples were ground to be plane and then polished with diamond suspensions down to a grain size of 3 µm. Three samples of each state were tested.

2.3.2 Reciprocating Sliding

A ball-on-flat setup was used, in which the flat, which is made from the coated or uncoated samples, was positioned vertically and fixed to the traverse of the machine via a load cell. The ball was rubbed against the flat in reciprocating sliding also in vertical direction. Standard bearing balls (100Cr6; 1.3505; AISI 52100) of 10 mm diameter were used as counter bodies. All tests were run lubricated, and the lubricant was fed into the contact by continuous dripping. The sliding motion was realised by a servo hydraulic machine in which the balls execute the movement. The normal force with which the balls were pressed onto the flats was realised by springs in a system of rods. Always two ball-on-flat systems were tested in one experimental run, to realise a closed distribution of the applied normal force (Figure 7).

During the experiments, normal and friction forces were measured. After the tests were finished, the samples were cleaned and the wear volume of each sample was determined using confocal microscopy (µSurf, NanoFocus AG, Oberhausen, Germany). Additionally, scanning-electron-microscopy was used to identify the wear mechanisms.

2.3.2.1 Parameters for CP4M

For reciprocating sliding wear tests, coated as well as uncoated samples were cut into pieces of 40 x 20 - 30 mm and the surface of the coatings was ground until a reasonable area was plane. These surfaces were then polished using diamond suspension down to a grain size of 1 µm (Figure 6).

The test parameters included a frequency of 6 Hz and an amplitude of the reciprocating motion of 2 mm. Thus the average relative velocity was 2.9 m/min and the number of cycles for one experimental run was 50,000, 500,000 or 1,000,000. The normal forces applied were 60 N, 180 N or 550 N, which correspond to static initial mean contact pressures of 1,230 MPa, 1,770 MPa and 2,570 MPa respectively, according to the Hertz'ian contact model. Tests with one parameter set were repeated three to four times. The lubricant used was Anticorit PL 3802 39 S (Fuchs Europe Schmierstoffe GmbH, Mannheim, Germany), which is an anti-corrosive forming prelube for sheet metal deformation processes. Cleaning of the samples was done using a mixture of acetone and petroleum ether (50:50) in an ultrasonic bath.

2.3.2.2 Parameters for Cr60Ni40

For reciprocating sliding wear tests samples with three overlapping layers were cut to a size of 30 x 20 mm and the surface of the coatings was ground until a reasonable are was plane. These surfaces were then polished using diamond suspension down to a grain size of 1 µm. Samples from cast Cr60Ni40 were taken from the same centrifugally cast material as the studs for the coating process, and were prepared for the wear tests with the same method as the coatings.

All tests were run at room temperature and lubricated with Silicon oil (M50, Carl Roth GmbH, Karlsruhe, Germany) to avoid oxidation in the contact. The oil has a viscosity of 45-55 mm^2/s and a density of 0.96-0.97 kg/m^3 according to the manufacturer's data sheet. The test parameters included a frequency of 6 Hz and an amplitude of the reciprocating motion of 3 mm. Thus the average relative velocity was 4.3 m/min and the number of cycles for one experimental run was 12,500 or 25,000. The normal forces applied were 45 N or 60 N, which correspond to static initial mean contact pressures of 1,110 MPa and 1,220 MPa with a nominal contact radius of 0.11 mm and 0.12 mm respectively, according to the Hertz'ian contact model. Each set of parameters was tested two or three times. After the tests were finished, the samples were cleaned in acetone in an ultrasonic bath.

2.4 Metallography and Microscopy

Samples were prepared from single- and multilayer coatings for examination of the microstructure by light and electron microscopy, as well as hardness measurements.

For light microscopy and scanning-electron microscopy (SEM), standard preparation techniques were applied, consisting of mechanical grinding, mechanical or electrochemical polishing and etching (partly also by electrochemical methods).

For transmission-electron microscopy (TEM), also mainly manual preparation techniques were used, during which thin samples are cut and mechanically ground to thin foils. The final thinning was either accomplished by electrochemical methods or by ion milling.

In confocal white-light microscopy (CLM), the surface topography of samples was measured, therefore the only necessary preparation step is a thorough cleaning of the surfaces.

For 3-point bending tests, coated and uncoated samples were machined to a defined geometry in order to gain comparable results for bending strength and to achieve a reliable evaluation of the coatings' bonding strength.

2.4.1 Light- and Scanning-Electron-Microscopy

Two reflected-light microscopes were used to observe polished and etched samples, model BX41TF, Olympus Optical Co. Ltd., Tokyo, Japan and Nikon Eclipse ME600, Nikon GmbH, Düsseldorf, Germany.

Scanning electron microscopy (SEM) was carried out at Gemini Leo 1530 equipment (Carl Zeiss AG, Oberkochen, Germany) with a field emission gun. Energy dispersive X-ray analysis (EDS) was accomplished by an Apollo X10 detector (EDAX Inc., Mahwah, USA) and for electron backscatter diffraction (EBSD) imaging a Digiview IV CCD camera (EDAX Inc., Mahwah, USA) was used.

2.4.1.1 Metallographic Preparation

6082 Aluminium Alloy

Samples for metallographic examination were cut and cold embedded (Scandiplex, SCAN-DIA Hans Tempelmann GmbH, Hagen) before being mechanically ground using SiC grinding paper (800 and 1200 grit (FEPA)). Polishing was accomplished by diamond suspensions with grain sizes from 9 to 1 µm, followed by a final polishing step with Colloidal Silica Suspension of 0.6 µm grain size.

For electrochemical etching to reveal the microstructure Barker's electrolyte was employed, consisting of 200 ml H_2O and 10 ml HBF_4 (fluoroboric acid; 35%). A voltage of 24V was applied to an area of 2 cm^2 for 120 s. The etching effect induced by this method becomes visible in the light microscope with a quarter-wave plate ($\lambda/4$) to polarise the light.

For electron-backscatter-diffraction imaging (EBSD) in the SEM, the polished surface to be investigated must be free of residual deformation from the preparation process, which is often found in a thin surface layer particularly on soft materials. Samples were therefore electrochemically polished using A2 electrolyte (Struers GmbH, Willich, Germany), applying a voltage of 30V for 20 s on an area of 1 cm^2.

NiAl-Bronze

After cutting, samples were hot mounted (Epomet, Buehler GmbH, Düsseldorf, Germany) and ground plane using 320, 500 and 800 grit (FEPA) SiC paper. Polishing was accomplished using different polishing cloths and diamond suspension with grain sizes of 9 µm, 3 µm and 1 µm. The downforce during polishing was not higher than 25 N per sample, since otherwise pitting of the treated surface may occur.

A two-stage etching method was applied to reveal the microstructure. As a first step, the cleaned samples were immersed for 2 sec into a solution from 40 ml distilled water, 40 ml ammonium hydroxide and 2 ml hydrogen peroxide (30%). Directly afterwards they were rinsed in water and immersed for again 2 sec in the second solution, containing 60 ml distilled water, 30 ml phosphoric acid and 10 ml hydrogen peroxide (30%), followed by cleaning in acetone in an ultrasonic bath.

CP4M Tool Steel

Steel samples, both from as-cast and coated material, were cut into adequate dimensions and hot mounted (Epomet, Buehler GmbH, Düsseldorf, Germany). Due to the high hardness and wear resistance of the material, grinding was started with SiC paper of 80 grit (FEPA), if necessary. Finer papers used after the initial rough grinding were of 180 and 320 grit, at 30 N downforce per sample. Polishing was carried out on polishing cloths using diamond suspensions of 9 µm, 6 µm, 3 µm and 1 µm grain size.

Different etching methods were used, since plenty are available for carbon steels. Most frequently, Nital solution (ethanol with 3 to 5% nitric acid) and a colour-etching method according to Marble (50 ml hydrochloric acid (32%) and 25 ml saturated aqueous copper sulphate solution) were applied at room temperature, while the residence times for optimal results varied between the samples.

Cr60Ni40

The studs used to produce the coatings by friction surfacing were machined from commercially available cast and heat treated components. Cross sections were prepared by standard metallographic methods from such material. To reveal the microstructure the polished samples were etched with V2A etching solution, containing 100 ml HCl, 100 ml H_2O, 10 ml HNO_3 and 1 ml Dr. Vogels' etchant (Buehler GmbH, Düsseldorf, Germany), which contains propanol and thiourea. Cross sections of the single and overlapping coatings were prepared with the visible plane perpendicular to the welding direction by means of the same method.

2.4.1.2 Hardness Measurements

Hardness measurements were carried out by the Vickers' method [89], in which a pyramidal shaped indenter is pressed onto the surface with a chosen force. The hardness is evaluated from the two diameters of the indentation imprint left after withdrawal of the indenter, measured using optical methods. The size of the imprint depends – besides the hardness of the tested material – on the chosen normal force, and hardness scales are available for each load level. Different forces were chosen for the different materials and samples in order to realize at least three imprints with adequate distances within each layer cross section.

Hardness measurement equipment for low to medium loads (Zwick GmbH & Co. KG, Ulm, Germany) was used, and polished samples were fixed in a device to ensure horizontal orientation of the surface. Imprints were placed at distances > 1.5 times the measured diameter to each other.

2.4.2 Transmission-Electron-Microscopy

In transmission-electron-microscopy (TEM), samples are examined by an electron beam which penetrates the material, and an image is recorded on the "back" side of the sample. For this reason, fine microstructural features within the crystal structure (dislocations, stacking faults…) can be pictured, but also very thin samples are needed. Sample preparation may be conducted by the Focused Ion Beam method, which cuts a sample thin enough and ready for examination. Traditional methods – more gentle towards the material with regard to energy input – are comparable to conventional metallographic preparation, including cutting, grinding and polishing to produce small, disc shaped thin foils (usually Ø 3 mm). The final preparation step for TEM samples is the local thinning to generate a hole – preferably in the center of the sample – by ion milling or electrochemical methods. The rim of this hole is then thin enough (≈ 100 – 200 nm) to be penetrated by the electron beam. In bright field imaging, intact crystalline areas are then depicted bright and disturbances in crystallinity cause dark regions on the image. Diffraction of the electron beam may be deployed to analyze the crystal structure and orientation [90] [91].

A Phillips EM 400 microscope with an accelerating voltage of 120 kV was used for the investigations (Philips Electronics Nederland B.V., Eindhoven, Netherlands).

2.4.2.1 Thin Foil Preparation

Samples were prepared into the shape of discs with 3 mm diameter and a thickness of 90 µm. Cutting (Accutom-50, Struers GmbH, Düsseldorf, Germany) was conducted in a way to later be able to place the point of interest in the material in the centre of the disc. Slices of around 200 µm thickness were cut from the bulk material. Coatings were cut off of the substrate parallel to the interface; if their thickness was too low the cutting plane was shifted into the substrate, which was then removed by grinding. For grinding, samples were glued onto the plane surface of a steel holder. SiC paper was used, up to grit 1200 (FEPA), and partially polishing with alumina suspension was applied. Both sides of the cut samples were treated to achieve a smooth surface finish.

When a thickness of 90 µm is reached, the samples are cleaned and 3 mm discs are punched from the foils, followed by final thinning.

The electrochemical method applied was electrochemical jet polishing (TenuPol-3, Struers GmbH, Düsseldorf, Germany) using A2 electrolyte (Struers GmbH, Willich, Germany). The available ion milling equipment was a DuoMill 600 and a Precision Ion Polishing System (PIPS) by Gatan GmbH, München, Germany, both deploying Argon ions.

2.4.3 Confocal-White-Light-Microscopy

Three dimensional surface topography measurements were conducted by confocal white-light microscopy (μSurf, NanoFocus AG, Oberhausen, Germany). The obtained measurements were evaluated using a corresponding software tool (μsoft analysis). Wear volumes were determined by defining the original surface plane by a three-point method in the software, and the automated calculation of material volume missing below this plane (wear pits) and volume above this plane (ridges from material push-up or adhering particles).

2.5 Bending Test for Bonding Quality

Three-point-bending tests were carried out to gain information on the bonding strength of the coatings, and their behaviour in the case of a fracture. The samples were placed in a three-point bending rig with cylindrical bearings of 5 mm radius and a distance of 105 mm between the outer bearings.

Single-layer coated and uncoated material was machined to 8 samples of 200 mm length, 6.2 mm width and, depending on the coatings, 10 to 11 mm thickness. The bending force was applied to the uncoated bottom side of the samples in order to apply tensile stresses on the coating during bending and was increased until fracture.

3 Results

3.1 Macroscopic Features of Friction Surfacing Layers

Photographs of single and multiple friction surfacing layers are presented in Figure 8. From the rings visible on the coatings' surfaces the welding direction can be deduced, since they form in the shape of semi-circles behind the moving stud. The direction of the stud movement over the substrate is indicated by arrows in Figure 8. The rings are quite uniform on the Al- and NiAl-bronze coatings, while on steel and particularly on Cr60Ni40 alloy the coatings have a less regular appearance. On all materials it is visible that the start of a coating layer is wider, where the stud was held in position while rotating during the preheating phase. With the onset of the translational movement, a deflection of the stud towards the advancing side takes place, due to the asymmetry of the process. This can be observed most pronounced on the steel samples (Figure 8 (c)).

In Figure 9 to Figure 13 cross sections perpendicular to the welding direction are presented for the four different materials. It is obvious, that they vary in width, thickness and shape.

The layer on the aluminium sample in Figure 9 has a thickness of 1 mm and a width of around 16 mm. At both edges a lack of fusion is visible, where the layer is not bonded to the substrate. This is a typical feature of friction surfacing and is due to the cylindrical geometry of the stud. Along the outer edge, the soft material in the heated stud tip does not accommodate the applied normal force and instead flows upwards to build a flash. Therefore, the downforce is not transformed into a contact pressure sufficient for bonding at the outer edge of the stud. The width of the bonded region is 11 mm.

The cross section presented in Figure 10 shows a NiAl-bronze layer on self-mating substrate. Single layer coatings were found to have a thickness between 0.60 and 0.80 mm in the centre, depending on process parameters. The width of the layers is around 24 mm, with a bonded region of around 20 mm.

A metallographic cross section of a CP4M sample is shown in Figure 11, showing coating layer, heat affected zone (HAZ) and substrate material. On both sides of the coating the characteristic lack of fusion is present. The thickness of all steel coatings lies around 0.40 to 0.45 mm, the bonded width between 7 and 9 mm, with a lack of fusion of 0.3 mm (advancing) to 1.0 mm (retreating) on each side, depending on process parameters. A cross section of a four-layer coating is presented in Figure 12. The layers have been placed with a stud displacement of 7 mm, and can be clearly distinguished by their fusion lines and HAZs. The lack of fusion of the 1st and 2nd layers have been closed by the application of each following layer.

A light-optical image of the etched cross section through a single layer Cr60Ni40 coating is presented in Figure 13. The Nimonic substrate was not affected by the etchant. At both edges along the coating the lack of fusion is visible. The coating layers have a thickness of around 0.25 mm and a gross width of 10.9 ± 0.9 mm, of which 8.7 ± 0.7 mm are bonded to the substrate. These data were obtained from six different single layer coatings, each measured in three positions.

3.2 Microstructure and Hardness

3.2.1 6082 (coatings) and 2024 (substrate) Aluminium Alloys

The microstructure of single-layer coatings from 6082 alloy on 2024 substrate is presented in Figure 14 to Figure 19. In the polished state (Figure 14), the precipitates are visible and from this the bonding line between coating (upper half of images) and substrate (lower half) can be distinguished. The precipitates visible in the coating are evenly distributed and up to 10 µm in size. In the 2024 substrate less precipitates are found, and these are elongated and in a size range of up to 10 µm thickness and up to 40 µm in length. The bonding line does not show any defects, apart from the lack of fusion characteristic for the friction surfacing process, at the edges of each coating layer (Figure 14 (b)). After electrochemical etching (Barker's reagent) pits are present, where particularly the smaller precipitates have been dissolved (Figure 15 (a)). In the microscope the grains in the 2024 substrate can be distinguished by their different colours when the light is polarised. They are elongated with lengths of 60 to 150 µm and a thickness in the range of 20 to 50 µm. Within the coatings, grains cannot be distinguished clearly due to the decreasing resolution of the deployed microscope when using polarised light. The bonding line is quite straight in some regions (Figure 14 (a)), while in others it is wavy due to deformation of the substrate surface (Figure 15).

The images in Figure 16 present the data of an EBSD measurement of the microstructure of a 6082 FS coating. The colours of the grains as shown in Figure 16 (a) represent their different orientations as indicated by the inverse pole figure at the bottom of the image (IPF). It is noticeable that in several regions neighbouring grains are of similar colours (i.e. of similar lattice orientation). Additionally, very small grains (1 – 2 µm) are found frequently in positions where they are surrounded by 4 or more larger grains. In Figure 16 (b), the standard deviation of the orientations measured on all single points within each single grain is coded by the colours given in the chart adjacent to the image (GOS). It can be seen that the grains are partially elongated, particularly in the upper part of the image (close to the coating layer's surface). Still, the misorientation within these grains is rather low, with black and blue coloured grains in Figure 16 (b). The degree of misorientation within single grains varies significantly, with values up to 4° (yellow grains). The grain size was determined from four different EBSD measurements and was found to be 2.4 ± 1.6 µm. The elongated shape of the grains was accounted for by measuring grain diameters in two directions and has a corresponding influence on the grain size deviation.

The EBSD maps presented in Figure 17 show a different region on the same sample. Here, the grains are less elongated, as can be seen in the inverse pole figure (IPF) map in Figure 17 (a). The second image, Figure 17 (b), shows a kernel average misorientation map (KAM), in which the average angle of misorientation between each measurement point and the points in five surrounding circles is presented. A schematic of three surrounding circles around a measurement point is shown in the upper right corner in Figure 17 (b) for clarification. Grain boundaries can be distinguished by the green lines, where the orientation between the measurement points changes. Still, they are not sharp lines, but quite broad and contain white points which represent pixels for which no orientation could be determined. In some cases, where a green line seems to indicate a grain boundary, the difference in orientation between the two neighbouring grains is very low, and sometimes only one grain is identified (see arrows and red box / Figure 18 (a)). The detail shown in Figure 18 (red box in Figure 17) is an image quality map, in which points with a clear, distortion-free measurement pattern have a bright grey shade, and the less clear ones are shaded darker. In addition, the change in orientation of the pattern measured for neighbouring points is indicated in blue, if the angle of lattice rotation between them is greater than 15°, in green if it is between 5° and 15°, and in red if it is below 5°. By this method, blue lines are certain to represent high-angle grain boundaries, while green and red lines can show low-angle grain boundaries and sub-structures within grains. Where the straight red line is placed as a marker, the image quality map and the presentation in Figure 17 (b) imply the presence of a grain or sub-grain boundary; still the automatic analysis does not depict a coloured line. In Figure 18 (b) the change in orientation angle of the measured points along the red marker line is presented. From the point-to-origin curve it can be seen, that an overall change in angle of orientation of around 2.5° is present, and therefore, accordingly, a low-angle grain boundary. The point-to-point curve clarifies, that this change takes place over a distance of around 0.25 µm, which is the reason why the substructure is not automatically identified by the software.

Images from TEM investigations of 6082 friction surfacing layers are presented in Figure 19 and Figure 20. The grains displayed in Figure 19 are in a size range of few micrometres or less. Dislocations are visible, partly entangled and blocked by precipitates. Precipitates of 300 – 500 nm diameter can be seen in Figure 19 (b) and one of the large precipitates also visible by light microscopy is shown in the bottom right corner of Figure 19 (d). A large fraction of precipitates found in all images is in the size range of several 10 nm and seems to be globular. They are spread evenly throughout the grains and neither a preferred precipitation at grain boundaries nor a precipitate-free seam along them have been found. Small phases or lattice defects of sizes below 10 nm, which could be beneficial for the hardness, are also visible in Figure 19 (b-c). In Figure 19 (b) dislocations accumulate at a precipitate of around 300 nm diameter, and at a nearby triple-point. A thin line of aligned dislocations, possibly forming a low-angle boundary (arrow) is visible on the left side in Figure 19 (c), seemingly separating two regions with differing amounts of accumulated strain. A low-angle grain boundary can be seen in Figure 19 (d) (arrow). In Figure 20 (a) a larger grain containing a gradient in dislocation density (from upper right to lower left corner) is visible, while in Figure 20 (b) dislocations interfering with precipitates are present in the grain in the lower half of the image.

Figure 21 shows the hardness profile of a single layer 6082 FS coating sample, measured in two series in the centre of a cross section. Just below the surface, at 50 µm depth, the coating has a hardness of around 90 HV0.2, which drops slightly to a quite constant and homogeneous hardness of 86 ± 2 HV0.2 deeper within the coating thickness. The unaffected 2024 alloy substrate has a hardness of 137 ± 4 HV0.2. Underneath the coating, in the centre of the layer width, the substrate material is slightly softened to a value of 128 ± 4 HV0.2. This heat affected zone (HAZ) reaches into a depth of around 1.4 mm below the coating/substrate interface.

3.2.1.1 Heat Treatment

Since the hardness in the 6082 FS coatings was found to be quite low initially (81 ± 4 HV5) despite the low grain size, heat treatment was conducted to ascertain whether the alloy can be hardened. Coated samples were treated with three different parameter sets: 170°C for 4h and 8h, and 190°C for 4h, followed by quenching in tap water at room temperature. After the 4h treatments, the 6082 coatings had a hardness of 100 ± 3 HV5 (170°C) and 100 ± 6 HV5 (190°C). After 8h at 170°C the hardness was 86 ± 3 HV5, similar to the one initially after coating. Within the substrate the hardness increased from originally 139 ± 5 HV5 to 142 ± 3 HV5 (4h) and 143 ± 2 HV5 (8h) at 170°C and to 156 ± 4 HV5 at 190°C and 4h.

In Figure 22 and Figure 23 the microstructure of a sample treated for 4h at 170°C is presented, since this would be the mildest one of the tested methods. Comparing the images before and after the heat treatment it is obvious that both in the coating and in the 2024 substrate underneath, phases with a reddish colour in the light microscope have appeared, which were not present before. In the 6082 coating, additionally a coarsening of the other visible precipitates has occurred.

3.2.2 NiAl-Bronze

Metallographic images from NiAl-bronze FS layers and their self-mating substrate are presented in Figure 24 to Figure 27.

The substrate was in the cast state, in which it is usually applied. It consists of the Cu-rich solid solution α-phase, which is of bright appearance after etching, lamellar regions of eutectoid decomposition of the high-temperature β-phase into α- and κ_{III}-phase, globular κ_{II}-phases and some small κ_V- or κ_{IV}-phases which precipitate within the solid solution α-phase (Figure 24).

In Figure 25 the cross section of a NiAl-bronze FS layer on self-mating cast substrate is depicted. The complete layer thickness is visible, as well as part of the heat affected zone (HAZ) in the substrate. The distribution of α- and decomposed former β-phase is significantly finer in the coating than in the cast material. The morphology of the microstructure within the coating changes from the surface towards the substrate. No defects were found in the bonding lines. The transition between coating and substrate is presented at higher magnification in Figure 26, the dashed line in the figure designating the bonding line. The transition is slightly wavy, and can only be recognized by the change in microstructure. While the coating contains globular α-grains, in the HAZ a needle-shaped structure of martensite or bainite prevails. Also, the globular κ_{II} precipitates of grey colour are only found in the substrate, not within the coating.

The microstructure within the coating layers contains lamellar as well as globular α grains, surrounded by the decomposed β-phase, which does not show the eutectic lamellae anymore (Figure 27). Close to the surface of the layer, the α-phase is of acicular shape (Figure 27 (a)), and in lower regions, closer to the substrate, the fraction of globular shaped grains increases (Figure 27 (b)). Precipitates, which are visible by light-microscopy in the as-cast material, where not found in the coating layers. Looking at the brown-coloured regions of decomposed β-phase between the α grains at a higher magnification, it is visible that they are composed of a high amount of globular phases, with sizes in the range of 100 nm (Figure 28).

In Figure 29 to Figure 31 further TEM images of NiAl-bronze FS coatings are presented. The various phases in the microstructure can be distinguished in Figure 29, showing α grains with straight grain boundaries, and regions of decomposed β-phase, consisting mainly of spherical phases. Elongated precipitates along the grain boundaries are also found frequently. In Figure 30, a strip of α-phase, possibly a twin, is shown bordering on a region of spheroidised β-phase (a). More of the latter is shown in Figure 30 (b), with globular phases of a size of around 100 nm. Dislocations in an α grain, interacting with small lattice defects, well below 100 nm in size, are visible in Figure 31 (a). Stacking faults are an additional feature found within solid solution, as seen in Figure 31 (b).

The TEM images presented in Figure 32 were taken within the heat affected zone of the NiAl-bronze underneath an FS coating. While the martensite laths in Figure 32 (a) show microtwinning, the lamellae seen in Figure 33 (b) could also be bainitic with precipitates, particularly in the upper left corner [92].

Microhardness distributions measured on a single layer NiAl-bronze FS coating are displayed in Figure 33. It can be seen that the average hardness within the coating material is slightly higher (251 ± 16 HV0.1), than that of the unaffected substrate material in the cast state (228 ± 27 HV0.1). Within the HAZ, the hardness is comparable to that of the coatings; peaks of more than 300 HV0.1 can be attributed to the martensite or bainite formation within this region (see Figure 26).

3.2.3 CP4M (coatings) and GP4M (substrate) Tool Steel

The substrate material (GP4M) of the steel FS coatings is cast and hardened, a state in which it is used for e.g. deformation tools. It shows some coarse inclusions - eutectic carbides formed during solidification – as well as some Ti carbonitrides and small (<1 µm) phases rich in Molybdenum, embedded in a martensitic matrix (Figure 34). The hardness was measured on three different substrate sheets (on which 7 different coatings were generated), being 683 ± 43 HV10.

The microstructure within the studs before friction surfacing represents the soft annealed state (226 ± 3 HV10), a ferritic matrix containing a large number of small carbides (Figure 35).

After the material has been applied by friction surfacing, it has assumed a very fine and homogeneous martensitic microstructure. No large carbides are present (Figure 36).

TEM investigations show the typical structure of plate martensite and retained austenite (Figure 37). Precipitates within the martensite are of sub-µm size (Figure 38). While in Figure 38 (a) a carbide of around 100 nm diameter is visible, the diffraction pattern in Figure 38 (b) reveals carbides of $M_{23}C_6$–type, oriented in a cube-cube relationship to the martensite matrix, which cannot be visually identified on the image. In this same picture, twinning within martensite plates can be observed.

By light and electron microscopy, the bonding of the coatings to the substrate was found to be of good quality. Aside from occasional oxide inclusions, no voids or cracks were found. Regions with a brighter appearance after etching are visible throughout the substrate, as so within the HAZ, where they show appearances of deformation (Figure 39), although no further major changes of the microstructure are obvious by light microscopy. The interface between coating and substrate is a sharp line for the FS coatings.

Microhardness measurements were conducted on cross sections. The measurement series were started close to the coating surface, and were continued through the HAZ until the measured values stabilised in the unaffected substrate material. An example for a single layer coating is presented in Figure 40 and one for a double layer coating in Figure 41, each showing two measurement series in the centre of the cross section on one sample. The hardness within the single layer coating is 800 ± 36 HV0.2 and in the unaffected substrate material 723 ± 44 HV0.2. Within the HAZ, the hardness directly underneath the coating is close to 800 HV0.2 too, but decreases down to a value of 500 HV0.2 at a depth of about 1.5 mm below the coating (Figure 40). The double layer coating consists of two layers placed in an overlapping manner with an offset of the studs' position of 6 mm. Therefore, two layers are passed through in the presented hardness profile in Figure 41. Still, the hardness evolution is similar as for the single layer coating. The hardness within the coating is 814 ± 27 HV0.2, followed by a high hardness of 870 HV0.2 in the uppermost part of the HAZ. The hardness then drops rapidly to lowest values in the range of

540 HV0.2 around 1 mm below the coating (≈ 1.8 mm below the sample's surface). The average hardness value of the substrate was measured to be 662 ± 32 HV0.2 in this sample.

In Figure 42 and Figure 43, results from a four layer coating are presented. Figure 42 (a) is a schematic representation of the positions towards each other, on which the four layers were placed. Due to the acting forces and apparently insufficient stiffness in the process set-up, the fourth layer was not deposited where it was aimed to be, but the stud was deflected during the process and pulled onto the previous layer, as indicated by the arrow in the figure. This can be clearly seen on the macroscopic image of the sample's cross section in Figure 42 (b). Hardness profiles measured in the regions marked by the red boxes in Figure 42 (b), are presented in Figure 43. On the left side of the cross section, layer 2 shows a low hardness of 627 ± 7 HV0.2, which stays on a comparable level in the upper region of the HAZ. The lowest hardness of just above 450 HV0.2 was found in a depth of 1.65 mm (≈ 1 mm below the coating). The hardness profile closer to the centre of the cross section crosses the layers 4, 3 and 2, which all together have a thickness of around 1 mm and an average hardness of 787 ± 40 HV0.2. The following 1.2 mm can be identified as HAZ, with the lowest value only about 0.4 mm below the coating. The profile measured on the right side of the cross section passes through layer 3 and layer 1. It is not clear, whether layer 4 also reaches this position. The overall thickness here is also in the range of 1 mm, and the average hardness is at 828 ± 39 HV0.2. Two heat affected zones can be distinguished in this position, one each from layer 1 and layer 3, illustrated by the W-shape of the hardness profile between 1 and 3 mm distance from the surface. Still, the depth to which the substrate material is affected by the heat input (≈ 1.5 mm below the coating) is only slightly larger than in the centre position where three layers are present. The unaffected substrate material of this sample has a hardness of 657 ± 57 HV0.2.

3.2.4 Cr60Ni40 (coatings) and Nimonic 80A (substrate)

Since the Cr60Ni40 coatings were clad on Nimonic substrate, samples were prepared from the unaffected material in the studs used for the process, as a reference for the state in which the material is typically used for components subjected to high-temperature wear and corrosion. The microstructure in the studs shows the dendritic structure being characteristic for the cast state (Figure 44 (a)). The darker regions are rich in Cr, while the regions with a brighter appearance show the lamellae of the eutectic solidification (Figure 44 (b)). Within the Cr-rich regions, a needle-shaped internal structure becomes visible after etching. Here, Ni-rich phases are present as well (Figure 44 (b), Figure 45 (b)). Presumably these stem from segregation processes during cooling, which can be attributed to the low solubility of Ni in Cr, as mentioned earlier. The chemical composition of the different phases was analysed by EDS in the SEM. Within the areas with needle-shaped internal structure the Cr:Ni ratios varied between 57:43 and 61:39 in wt.%. On the Ni-rich phases within these areas a Cr:Ni composition of 48:52 was detected. For the eutectic areas the measured Cr:Ni ratios ranged from 47:53 to 50:50. Spherical and lamellar non-metallic inclusions are found throughout the samples (Figure 45 (a), Figure 46). They were analysed by EDS measurements as presented in Figure 47 and Table 6. The lamellar inclusions were found to be rich in O and Mn, and the globular ones mainly contain O, Si, Mn as well as small amounts of S and Ti. Both types of inclusions show a significant amount of Cr (≈ 40 to 60 wt.%) when examined by EDS, while very little Ni (≈ 1 or 15 wt.%) is detected. Though it must be expected that the material surrounding and underneath the measurement areas contributes to the measurement signal too, the discrepancy between the detected Cr and Ni values supports the assumption that some Cr is incorporated in the inclusions as well.

Within the Cr60Ni40 FS coatings, darker and brighter regions are visible by light microscopy, showing the material flow during the coating process (Figure 48). Further grain boundaries are visible in the darker etched areas as well as small precipitates within the brighter ones (Figure 49). Fine needle-shaped precipitates become visible within the more strongly etched phase (Figure 48 (b), Figure 50). Measurements of the local chemical composition of the material were obtained by EDS in the SEM and, with some local variations, average ratios of Cr to Ni in the two main phases were found, as indicated in Figure 50. In the more strongly etched regions, the average ratio in wt.% of Cr to Ni was found to be 63:37, and in the constituents less affected by etching, it is 52:48. Additionally, approximately 1.2 wt.% of Fe were found in all constituents. Mn, Si and Ti were only found in the spherical non-metallic inclusions, which are still present as seen in the cast and heat treated state.

In Figure 51 to Figure 55, the microstructure of Cr60Ni40 coatings is shown in images from transmission-electron microscopy. In Figure 51 it is visible that the grains in the coating are locally very small, in the range of several 100 nm to several µm. The two phase regions can be distinguished, since one – the Cr-rich one – shows the internal substructure, while the other (Ni-rich) is easily penetrated by the electron beam and is of bright appearance in the images. The Ni-rich regions show no signs of eutectic lamellae, which have been dissolved and not precipitated again. Instead, the fcc structure of Ni still dictates the crystallographic structure of this phase, though highly supersaturated with Cr. Dislocation density gradients are visible in both images in Figure 52, and deformation seems to accumulate at grain (twin) boundaries. In Figure 52 (a), the straight boundary in the centre of the image has a corrugated appearance, typical to sub-grain boundaries formed by parallel dislocation arrangement. The ledge in the boundary visible in Figure 52 (b) might have been caused by grain boundary slip during deformation [92]. The very straight grain boundaries and the presence of twinning (Figure 53 (a)) are typical features of austenitic crystal structures. In Figure 53 (b) it is also visible that dislocations have arranged themselves to a sub-grain structure (polygonisation), pointing to a recovery process during cooling. The Cr-rich crystals in the coating still contain the internal substructure (Figure 54), but less bulky Ni-rich crystals from segregation processes (see also Figure 48 (b)).

Electron diffraction in the regions with internal structure was very difficult, and when possible resulted in a complex pattern, as presented in Figure 55. The analysis of the pattern succeeded for a Chromium bcc structure, as indicated in Figure 56 (black lines), while the second phase observed in the pattern (red lines) was not identified. It was compared to parameters for the ordered Ni_2Cr phase (orthorhombic, Pt2Mo-type) forming in the Ni-Cr system below 590°C [85], besides the Ni fcc and Cr bcc crystal. In addition, a hexagonal intermediate phase found to form by disintegration during cooling in an alloy containing 34.4 wt.% Ni was considered [93], since the diffraction and bright field images in the reference look very similar to the ones found in the present study. Still, the parameters do not match.

The substrate, Nimonic 80A, is affected by the heat and shear stresses generated during the friction surfacing process within a certain region underneath the coating. In light-microscopical images in Figure 57, this can be seen by signs of deformation (arrows) and slip bands (encircled).

Hardness measurements were conducted on single layer cross sections by the Vickers' method using a weight of 5 kg (HV0.5). The first measurements were placed 50 µm below the coating surface and the following ones were placed at distances of 100 or 200 µm advancing into the substrate material. In Figure 58 measurements in the centre of three different coatings are presented. The hardness is highest within the coatings and ranges from 420 to 550 HV0.5. Underneath the coatings, a steep drop in hardness to 270 HV0.5 is found within the heat affected zone. The hardness stays at this low value down to a depth of around 0.5 mm, before it continuously rises back to the original substrate hardness of about 400 HV0.5 in a depth of 1.5 mm below the surface.

3.2.4.1 Heat Treatment

In order to assess the stability of the microstructure of Cr60Ni40 FS coatings under increased temperature – since this is a material intended for high-temperature applications – a set of various heat treatment parameters was tested. A single FS coating layer on Nimonic substrate was cut into pieces of approximately 10x10x15 mm (including the substrate), and the samples were treated at 500, 550, 600, 650 and 700°C for each 2, 5 and 10h. After each heat treatment step, the hardness was measured and the microstructure was observed by light microscopy. Results for the evolution of hardness – over heat treatment time for three different temperatures and over temperature for the three heat treatment durations – are presented in Figure 59 and Figure 60 respectively. The shaded background of each displayed measurement series represents the standard deviation of 15 hardness measurement values. The hardness values show large scattering due to the two different types of phase regions in the microstructure, and the low size of the indents under the applied load of 0.2 kg (HV0.2).
Figure 59 shows that different recovery and hardening mechanisms seem to take place at the different temperatures. To ensure clarity of the diagram, the curves for 550 and 650°C were omitted; they follow the curve of 600°C heat treatment temperature. The difference in hardness between the phases is up to 400 HV0.2 in the coatings without heat treatment. After 2h at 500°C, there is a slight increase in average hardness of 30 HV0.2 detected, which is negligible considering the large standard deviation of the measured values. The hardness decreases with longer heat treatment times at 500°C down to 508 HV0.2 after 10h. At the same time, the scattering of the values decreases to a standard deviation of ± 58 HV0.2. At temperatures above 500°C, after 2h already a significant drop occurs both in hardness values and their scattering. For the temperatures 550, 600 and 650°C, this first drop is followed by an increase in hardness after 5h heat treatment, followed by a slight drop after 10h to meet the hardness of the 500°C samples at values around 500 HV0.2. At 700°C, after 5h the hardness stays at the low value reached already after 2h of around 437 ± 33 HV0.2, followed by a drop down to 395 ± 24 HV0.2 after 10h. For all temperatures above 500°C it is clear that the difference in hardness values of the two main phases decreases significantly with the heat treatment time, down to a standard deviation of approximately ± 25 HV0.2 after 10h.

The same data is presented in Figure 60, now illustrating the evolution of hardness over the different temperatures. The average hardness after 2h and 5h is the same for 500°C and 700°C (580 and 440 HV0.2 respectively), and for both temperatures the value after 10h is lower (510 HV0.2 (500°C) and 400 HV0.2 (700°C)). At the heat treatment temperatures 550, 600 and 650°C, the samples have the highest hardness after 5h treatment duration. The standard deviation has a tendency to be lower for higher heat treatment temperatures, although this trend is not as pronounced as for the heat treatment durations.

Light-microscopical images of samples treated at 550°C and 700°C are presented in Figure 61 to Figure 63. After 2h at 550°C, when the hardness of the sample has dropped from 560 ± 205 HV0.2 to 505 ± 121 HV0.2, no changes in the microstructure are visible by light microscopy (Figure 61 (a)). In the sample treated at 700°C for the same duration, a large number of precipitates become visible throughout the coating material, in a size range of few micrometers (Figure 61 (b)), at a hardness of 438 ± 76 HV0.2. After 10h, precipitates are also visible in the sample treated at 550°C, arranged in what looks like a network, presumably along grain boundaries of the Ni-solid solution crystals (Figure 62 (a) and Figure 63 (a)), at 480 ± 28 HV0.2. The sample treated for 10h at 700°C shows a homogeneous distribution of dark and bright phases, with sizes in the range of 3 – 5 µm (Figure 62 (b) and Figure 63 (b)) and the lowest achieved hardness of 395 ± 25 HV0.2.

Figure 64 and Figure 65 present SEM images taken in different regions on a sample treated for 10h at 700°C. The structure of the two phase regions present before the heat treatment is still recognisable in some places (Figure 64 (a), also Figure 63 (b)). Looking at the former Ni-solid solution at higher magnifications, it becomes visible that lamellar precipitates have formed, similar to a eutectic decomposition (Figure 64 (b)). In other regions, the Ni-austenite based and the Cr-rich phase regions are intermixed with small grain sizes in the range of few micrometres (Figure 65 (a), also Figure 62 (b)). At higher magnifications, the inner structure of the Cr-rich phase becomes visible, as well as few lamella within the Ni-austenite (Figure 65 (b)).

3.3 Bonding and Possible Defects

3.3.1 Appearance of Bonding Lines

6082 on 2024 Aluminium Alloy

In cross sections of the aluminium samples, a narrow seam of few micrometres within the substrate along the bonding line shows a somewhat differing reaction to etching than the other regions of the material (Figure 66). From light-microscopical images it is not clear if this is due to a feature of the microstructure, or a preparation artefact. Still, deformation in the substrate surface material can be discerned by a wider area of uneven colouring of the upper parts of some 2024 grains (Figure 66 (b)).

In Figure 67, an EBSD measurement across the bonding line of a 6082 FS coating on 2024 substrate is presented. The grain orientation image in Figure 67 (a) shows the difference in grain size between the coating and the substrate. White pixels are shown for points for which the orientation could not be determined in the measurement. White regions are found predominantly along grain boundaries, along the bonding line, and in the 2024 grain adjacent to the coating. From the kernel average misorientation map in Figure 67 (b) it can be seen, that strain accumulation within the substrate grain adjacent to the coating is significant, while the first row of grains in the coating seems to be less deformed. It can therefore be assumed, that the white, unmeasurable region along the bonding line is part of the substrate 2024 alloy. The TEM image across the bonding line of an aluminium sample in Figure 68 supports this assumption. A high dislocation density can be seen within the substrate grains (left side of the image), while the coating grains – which can easily be identified by the visibility of small precipitates – have the usual size in the range of few micrometres, pointing to a recrystallized state. Still, some of them are of dark appearance in the image, too, showing that they also contain defects in their crystal structure. An interesting feature in Figure 68 is that there seems to be a band of quite constant width, both on the substrate and on the coating side of the bonding line, with straight boundaries to the rest of the material. On the substrate side, the band has a width of 1.2 µm, and on the coating side, where it is not as clearly discernible, it has a width of around 2.3 µm (see arrows).

NiAl-Bronze

In case of the self-mating NiAl-bronze FS coatings, bonding is not realised along a sharp line. The change in microstructure between substrate (heat affected zone) and the coating is obvious (Figure 69 (a)), but at higher magnifications, no discreet transition is found. The coating can be identified by globular α grains and the fine spherical phases in the decomposed former β-phase. Besides the needle structure of the martensite in the heat affected zone, the substrate can be distinguished by the presence of grey coloured spherical inclusions, which are not found in the coatings (arrows in Figure 69 (b)).

CP4M on GP4M Tool Steel

In the steel FS samples, both the coating and the substrate have a martensitic microstructure. Due to the hardness of the substrate material, the bonding line is very straight, but it does show signs of the heat input in the shape of slightly larger austenite regions in the first few micrometres below the coating (Figure 70 (a)). The bonding between overlapping layers is visible in etched cross sections as thin lines, possibly due to small oxide particles present within them, as is also occasionally the case in the bonding line to the substrate (Figure 70 (b)). In Figure 71 (a) the light-microscopical image of an etched cross section of a triple-layer coating is presented, showing the bonding line between layers 2 and 3. While the two layers can be discerned by a different morphology of the martensite, the bonding line consists of an up to 15 µm wide seam of different colouring. In the SEM it was found that this seam contains small oxide inclusions (Figure 71 (b)). The primary carbides present in the cast and heat treated substrate seem not to have a detrimental effect on the bonding, when they are located at the substrate surface in the centre of a coating layer's cross section. While in Figure 72 (a) no reaction to the presence of a large carbide conglomerate can be seen at all, the one seen in the sample shown in Figure 72 (b) is protruding from the substrate surface. The bonding line in this case shows some small voids, possibly due to oxides that have been removed during etching, above the carbides as well as beside it. It is not clear, whether the protrusion of the carbides from the substrate's surface plane was caused by the surfacing process, or already earlier during the machining of the substrate sheet. Cracks associated with the presence of the large carbide conglomerates are discussed in chapter 3.3.3.

Cr60Ni40 on Nimonic 80A

In Cr60Ni40 layers on Nimonic substrate, along the bonding line between coatings and substrate, a seam of fine oxide particles prevails (Figure 73). When overlapping layers are applied correctly, the bonding between them can have different appearances, depending on the plane along which the cross section was taken, and whether the overlap was realised at the advancing (Figure 74 (a)) or the retreating side (Figure 74 (b)). In both cases, bonding between two layers can be achieved without any defects, besides again some small oxide inclusions, if the proper process parameters are applied. The lack of fusion at the edge of the lower layer is closed by heat and pressure from the process of applying the next overlapping layer.

3.3.2 Bending Tests

Three-point bending tests were carried out on single layer steel FS coatings as well as uncoated steel substrate material in the cast and hardened state.

The samples without coatings showed no differences in bending force at fracture or in deflection, compared to the coated samples. Fracture occurred at a bending force of 6.65 ± 1.12 kN with an average deflection of 1.06 ± 0.14 mm. The high scatter of the force at fracture and the linear progression of the force-deflection curves (Figure 75) are as expected for brittle materials. The slopes of the linear parts of the curves are in average slightly smaller for the three coated samples (6.72 ± 0.04 N/µm) than for the two uncoated ones (6.97 ± 0.02 N/µm). From the standard formulas for a beam with rectangular cross section in bending, the maximum stress in the samples' surface can be calculated by

$\sigma = \frac{M \times \frac{y}{2}}{I}$ with

$M = F \times z$ and $I = \frac{x \times y^3}{12}$,

where F is the force at fracture, z = 52.5 mm is the distance between the outer bearings and the point where the force was applied (in the middle of the sample) and x = 6.2 mm is the width of the rectangular cross section. The height of the cross section, y, varies between 10 and 11 mm for all samples, depending on the coatings' thickness. In the case of the uncoated samples, the thickness of the substrate material sheet is y = 10 mm. For the two uncoated samples presented in Figure 75, "cast 1" and "cast 2", the maximum stress at each samples' surface is therefore 2773.21 MPa and 4237.53 MPa respectively. The values for the coated samples can be considered to lie within this range. Since not necessarily the complete width of the coating on a sample machined for the bending tests is bonded to the substrate (see Figure 76), a calculation of the maximum stress in the surface in the presented way would not be exact.
No plastic deformation of the samples could be detected after the experiments, and the fracture surfaces are all flat. Heat affected zone as well as the coating show a smoother fracture surface, than the cast substrate material (Figure 76). No signs of delaminations were found on any of the coated samples.

3.3.3 Welding and Bonding Defects

Cracks in the substrate material were found in two steel FS samples. In both, the cracks originate at the inner edge of the undercut caused by the lack of fusion at the sides of the layers. The crack underneath the two-layer coating in Figure 77 (a), with a length of around 350 µm, propagated almost perpendicularly to the former surface plane into the substrate. No obvious cause for the crack is visible in the microstructure on this cross section. The cracks presented in Figure 77 (b) follow a conglomerate of large primary carbides. Other types of cracks were not found in the examined samples from steel FS coatings.
In Figure 78 and Figure 79, images from a four layer steel FS sample are shown. The structure of the overlapping layers of the same sample is also presented in Figure 42 (a). It can be seen that the two lower layers were applied leaving a gap between them, which was filled by the third layer. The SEM picture in Figure 79 present details of the lack of fusion seen also in the middle of Figure 78. Obviously, pressure and heat generated during the application of the third and fourth layer were not sufficient to completely bond the applied layers and the substrate.

If the offset between overlapping layers is too large - in case of the Cr60Ni40 alloy more than 10 mm - no bonding is achieved between the overlapping coatings, and the lack of fusion of the lower layer is not closed (Figure 80 (a)). In this case, also a thick oxide layer has formed on the lower layer, of grey appearance in the image. Water spray cooling of the Cr60Ni40 studs was tested during some surfacing trials in order to minimise the flash and, therefore, increase the coating efficiency. As a result of the increased cooling rate, vertical cracks (segmentation cracks) appeared in the coatings (Figure 80 (b)). Without water spray cooling and with a smaller distance between overlapping layers, multilayer coatings free of defects were achieved with the Cr60Ni40 alloy.

3.4 Wear Behaviour

3.4.1 Cavitation

3.4.1.1 6082 Aluminium Alloy

The wear of samples subjected to cavitation was monitored in predefined intervals by measuring the weight loss and by examining the surface topography and the wear appearances. In Figure 81 (a) a picture of a worn sample from 2024 substrate material is presented as an example. Along the dashed line, a surface topography profile was measured using confocal microscopy, which is shown in Figure 81 (b). The depth of the wear scar is locally in the range of 70 µm or even deeper, while in other regions peaks within the worn area are as high as the original sample surface level. Although obviously a significant amount of material has been removed by wear, it was not possible to determine a weight difference – particularly at the earlier stages of the wear – with the available scale, due to the low density of the material. The progress of the wear was therefore evaluated by identifying the maximum wear depth in the wear scar after each cavitation interval. Such data is presented in Figure 82 for three different 6082 FS coated samples. The three presented curves of local maximum wear depth versus test duration were measured on one coated sample in the original state after friction surfacing, and two samples which were heat treated to increase the hardness (see also chapter 3.2.1.1). The wear depth of all three samples increases quite constantly and without any incubation time. The increased hardness of the heat treated samples does not lead to an improved wear resistance. On the contrary, after 120 min test duration both heat treated samples have deeper cavities than the untreated one.

The appearances of the worn surfaces were pictured by scanning-electron microscopy. Images from two samples (one as-coated and one heat treated) after 120 min cavitation duration are presented in Figure 83 and Figure 84. Both show completely roughened surfaces, with cavities and extrusions, pointing to a ductile material behaviour without visible cracks. No significant difference in wear appearances is recognisable between the heat treated and the untreated sample. Light-microscopical images of a cross section polish through a worn heat treated sample were prepared. In Figure 85 (a) the outer edge of the worn area can be seen above the lack of fusion of this coating layer. The picture in Figure 85 (b) shows the roughened surface in the centre of the worn area. At higher magnification can be seen that extrusions from the surface have been deformed and folded back onto the surface (Figure 86).

3.4.1.2 NiAl-Bronze

Weight loss due to cavitation erosion on NiAl-bronze FS coatings as well as uncoated substrate material in the as-cast state, up to a test duration of 7.5 hours, was measured with a precision of 10^{-4} g. In Figure 87, graphs for two coated and two cast material samples are presented. Although scattering of the measured values was observed, it can be stated that the incubation time, i.e. the period of time in which no weight loss can be detected, is in average about twice as long for the coated samples, as for the as-cast material. The average wear rate in the period between end of incubation time and end of each experiment is for the samples with friction surfacing layer 11 ± 6 µg/min and for the untreated substrate material 20 ± 7 µg/min.

The topography of the eroded surfaces after exposure to cavitation for 105 min and 410 min was measured by means of confocal microscopy. The results for the samples “cast 1” and “coating 1” from

Figure 87 are shown in Figure 88. After 105 min, i.e. at the end of the cast sample's incubation period, the surface roughness is already distinctly higher for the as-cast material. For measurements after longer test durations it was no longer possible to use the same z-axis resolution for coated and uncoated samples, due to the further divergence of roughness. In the measurements after 410 min, the z-axis was chosen to match the distance between the highest and the lowest point on the scanned surface section. The cavities on the as-cast sample are therefore maximum 20 μm deep, while those on the coating have a maximum depth of about 9 μm. It can also be seen, that the cavities on the coating are more evenly spread over the surface than on the as-cast material, where larger areas have been worn. This can also be seen in the 2D presentation of the measurements after 410 min in Figure 89.

In Figure 90 to Figure 92, SEM images of worn surfaces of coated and uncoated samples after exposure times to cavitation of 60, 180 and 410 min are presented. After one hour, on all materials dimples of few micrometres in size, mostly due to pure deformation are present. On the as-cast material, some precipitates seem to have fallen off, leaving cavities in the surface. Also it can be seen, that some precipitates have been pressed into the surrounding material, which at the same time seems to cause them to detach from it (Figure 90 (a, b)). On the coated sample, at the bottom of some larger cavities, cracks are visible (Figure 90 (c, d)). After 180 min, which according to the weight loss curves should be approximately the end of incubation time of the uncoated material, the complete surfaces are damaged. Some areas (e.g. on the right on the image in Figure 91 (a)), seem to be rougher, than others, of which a detail is presented in the Figure 91 (b). In the latter, small particles seem to be torn off, but especially the larger κ_{II}-phase is still present. On the surface of the coated sample, the two phases present in the microstructure have become visible (Figure 91 (c)). One phase shows a fine roughness, while the other is smooth and still shows grinding marks from preparation (Figure 91 (d)). Although after 180 min this sample should still be within its incubation period, some material detachment is visible. This, as well as some extrusions, seems to be located mainly on the smooth phase. After 410 min, both the as-cast and the coating material show disruptions all over the loaded surface. On material regions protruding between cavities on the uncoated sample, all types of κ precipitates present in this bronze are visible (Figure 92 (a)). At the bottom of the cavities, cracks which seem to stem from grain boundary attack can be found (Figure 92 (b)). On the coating, some of the finely roughened areas visible after 180 min still seem to be present between the cavities. After 410 min, also deformed material is observed, as seen in the middle of Figure 92 (c).

Cross sections were prepared from both as-cast material and coatings after 410 min exposure to cavitation. Figure 93 shows light optical and scanning-electron micrographs of cross sections through the worn surface of as-cast samples. Wear seems to have been more severe on the α-phase (bright areas in the light optical and smooth ones in the scanning-electron micrographs). Sections holding κ precipitates, especially the lamellar κ_{III} from eutectoid decomposition (brown areas in the light optical micrograph), are protruding between cavities within the α-phase and have a more flat surface (Figure 93 (a, b, c)). Branching cracks within the α-phase, some of them opened, are found up to a depth of more than 10 μm below the worn surface (Figure 93 (d)). In the coating material, wear appearances were mainly found close to the loaded surface, at maximum in a depth of 5 μm (Figure 94 (a, b)). The material seems to be deformed within about 1 μm below the surface (Figure 94 (b)). Cracks seem to follow the interfaces between the two phases, at angles usually below 45° from the surface. Here also the α-phase seems to have been worn more severely than the regions of decomposed former β-phase containing spherical precipitates (Figure 94 (c)), but the α grains in the coating material are smaller, than the ones in the as-cast state.

3.4.1.3 Cr60Ni40

In Figure 95 to Figure 101, SEM pictures of worn surfaces of Cr60Ni40 samples after different intervals of cavitation testing are presented. Coated samples and as-cast material samples are shown in parallel in order to demonstrate the major differences of the wear appearances.

After 45 min the cast and heat treated samples show outlines of grains and non-metallic inclusions have been pulled out (Figure 95 (a)) while the coatings present only very small voids related to fine oxide particles (Figure 95 (b)).

After 120 min, inter- and transgranular microcracks lead to delaminations up to about 50 µm in size all over the worn surface of the cast and heat treated samples (Figure 96 (a), Figure 97 (a)). In addition plastic deformation can be seen within the eutectic areas (Figure 97 (b)). For the coatings the two main constituents become slightly distinguishable and few pull-outs are visible (Figure 96 (b)).

Delamination and plastic deformation proceed with advancing test duration. In the cast and heat treated state, after 180 min cracks no longer prevail at the phase boundaries, but are also visible within the Cr-rich phase (Figure 98 (a)). Still material removal is mainly brought about within the eutectic areas (Figure 99). Again the coatings show less cracks and pull-outs (Figure 98 (b)).

After 300 min it becomes visible, that for the cast and heat treated samples both main phases, the eutectic and the Cr-rich constituent, have been affected by cavitation. Size and number of delaminations increased significantly (Figure 100 (a)), while on the coatings they appear predominantly on one phase (Figure 100 (b)). This tendency persists even after 540 min. While on the cast and heat treated samples, the surfaces wear extensively, on the coatings one phase endures. Even now it still shows polishing marks from sample preparation (Figure 101). This most resistant phase could be identified by EDS with a Cr:Ni ratio of 63:37 as the Cr-rich constituent with internal needle-shaped precipitates.

In the light-microscopical images presented in Figure 102, this finding is confirmed. The cast sample in Figure 102 (a) clearly shows larger wear depth in the bright eutectic phase, than in the brown coloured Cr-rich one. In the cross section of the coating sample it is obvious, that here the size of single-phase regions is significantly lower, and they are evenly distributed (Figure 102 (b)), which leads to a lower size of the cavities in the surface

The weight loss measured in between the intervals of cavitation testing is presented for two exemplary samples in Figure 103. No incubation time within the first minutes of testing was found, and up to 120 min a steady wear took place, similar for both types of samples. Following this the curves decline with the weight approaching the original value again. This increase in weight was found on all samples and in a similar range both in magnitude of weight “gain” and time of testing, though slight differences were visible when shorter intervals where chosen for a cavitation test. A possible explanation for this behaviour could be that water has entered fine cracks and voids which formed in the first stages of loading, e.g. along phase boundaries (see Figure 98), leading to an increase in measured weight. It was not possible to eliminate this effect by heating or evacuating the samples before weighing, which might be explained by a capillary attraction of very fine cracks. With continuing cavitation the discontinuities on the surfaces become larger, disabling possible capillarity effects, and therefore leading to a measurable weight loss again (see Figure 100). Nevertheless, after 360 min of testing it becomes obvious, that the wear rate of the coating is lower than that of the cast and heat treated one. Thus after 420 min the coatings wear by an average of 13 µg/min, while the cast and heat treated samples show a higher rate at 37 µg/min.

3.4.2 Sliding Wear

3.4.2.1 CP4M and GP4M Tool Steel

Wear volumes of coated as well as samples from cast and hardened GP4M steel after sliding wear testing were determined using 3D confocal microscopy. Figure 104 shows a characteristic wear track on a cast and hardened sample after 500,000 cycles at 180 N normal force. The colours in the image represent the height of each surface point, as indicated by the shown colour scale. Grooves in sliding direction and some pits can be observed. From such measurements, the wear volume was determined by calculating the missing volume under the polished surface plane (of pink colour in Figure 104). Wear volumes from all executed experiments are presented in Figure 105. The positive numbers in the figure give the volume of pits and other depressions on the formerly plane surface, where material has been removed due to the wear. The negative values given are the volume of material that has been piled or pushed up and protrudes from the original surface plane. The latter can be e.g. accumulated wear particles or deformed material around the worn surface area. For a normal force of 60 N, no significant difference is found between the coatings and the cast and hardened material. The wear volume has a tendency to increase with an increasing number of cycles, but in the average it stays below 200,000 μm^3 after one million cycles. At 180 N and particularly at 550 N, the wear volume of the coatings is higher, while the volume of the piled up material is clearly lower than those of the cast and hardened samples.

Wear appearances found on coatings and cast and hardened samples are similar. At 60 N normal force, tribochemical layers dominate the wear appearances, even for long test durations (Figure 106). With increasing normal force, grooves parallel to the sliding direction appear and with increasing number of cycles, delaminations are found (Figure 107). Surface fatigue crack growth preceding the delamination of the affected material can be observed in Figure 108 (a). On some of the coated samples, locally small defects in the coatings' surface lead to a detachment of material already during the samples' preparation (Figure 108 (b)). An overall wear depth could not be identified, since the wear volume is determined mainly by the local delaminations. The maximum depth of the delaminations on all examined cast and hardened samples is 6 ± 3 µm, and on the coatings 4 ± 3 µm. The higher overall wear volumes of the coated samples are due to a higher number of delaminations on the coatings.

On the balls, all wear scars were found to be circular in shape, showing abrasive grooves, tribochemical layers and occasionally delaminations (Figure 109). The diameters of the wear scars on balls are shown for experiments at 60 N and 180 N and 500,000 as well as 1,000,000 cycles in Figure 110. They are comparable for experiments on cast and hardened and FS coating samples. The wear scar diameters show two levels, one for 60 N and one for 180 N, independent of the number of cycles. The same does not hold true for the shorter experiments, which indicates that on the balls material removal by abrasion takes place mainly within the first 50,000 cycles. The horizontal bars in Figure 110 represent measured wear scar widths on the corresponding flat samples, which match well the size of the ball wear scars. Assuming the balls' worn areas to be flat, nominal contact pressures acting at the end of the experiments can be calculated from the measured diameters. Average values for the diameters are used; 315 ± 38 µm for 60 N and 550 ± 47 µm for 180 N normal force. From this, the average nominal contact pressure for 60 N normal force results to 770 MPa, and for 180 N normal force to 760 MPa. These two values are quite similar, and significantly lower than values calculated from Hertz` theory [94] for the initial mean contact pressure for the unworn contact bodies. Those theoretical pressures are 1,230 MPa for 60 N and 1,770 MPa for 180 N normal force. Friction coefficients range between 0.06 and 0.1.

3.4.2.2 Cr60Ni40

A sample with a triple Cr60Ni40 FS coating after sliding wear testing is presented in Figure 111. On the plane ground and polished coating 5 tests have been conducted, of which one had been placed too close to the edge of the prepared surface plane and was interrupted. The balls have been sliding on the surface in vertical direction.

The average friction coefficients calculated from the measured normal and tangential forces are 0.32 ± 0.01 (60 N) and 0.29 ± 0.02 (45 N) and are independent of whether cast or FS coating material was tested.

Wear scars on the flats are trough shaped, as shown in the 3D topography image in Figure 112 (a). Grooves parallel to the sliding direction and a small amount of material build-up around the wear scar are visible. The volume of the trough (wear volume) can be determined from the measured topographical data, and the values for the different test parameters are presented in Figure 112 (b). Compared to these values, the volume of material build-up around the wear scars is negligible. The wear volume of the Cr60Ni40 material increases both with the normal force and the number of cycles. Both the cast material and the coatings behave in this way, while the coatings always show a slightly lower wear volume for each test parameter set, than the cast material under the same conditions. On the balls, the wear volume was too small to be determined by this method.

In Figure 113 and Figure 114 images from scanning-electron microscopy of a pair (flat and ball) of worn surfaces from a wear test with 60 N and 25,000 cycles are presented. The trough shaped wear scar on the flat shows at higher magnification grooves and some delaminations (Figure 113). Two spherical inclusions are also visible, which have not been damaged during the wear test (Figure 113 (b)). On the ball, within the elliptical wear scar, also some grooves are visible. At higher magnification it becomes obvious, that small beads of material adhere to the otherwise rather smooth ball surface (Figure 114). EDS measurements of the adhering material show that it contains high amounts of Cr and Ni, in comparison to more smooth regions in the wear scars on the balls (Table 7).

Cross sections were prepared from the worn Cr60Ni40 samples, with the polished plane parallel to the sliding direction. Light-microscopic images of samples from cast material and coatings are presented in Figure 115 and Figure 116 respectively. Deformation parallel to the sliding direction of the material closely underneath the surface is found on both cast and coating material. Presence and depth of deformed material vary locally along the wear scar and no obvious relation to the test parameters is observable. If present, the deformation on the cast samples reaches significantly deeper into the material (up to ≈ 50 µm) than on the coatings (up to ≈ 10 µm) (Figure 115 (a) and Figure 116 (b)). Also, lens-shaped layers of bright appearance after etching are visible locally underneath the worn surfaces of all samples. These white etching layers (WEL) have thicknesses up to 30 µm and particularly on the cast samples they contain cracks and are partly delaminated (Figure 115 (b) and Figure 116 (a)). Figure 117 shows an SEM image from the subsurface material on the etched cross section through a wear scar on a Cr60Ni40 coating. Underneath the Ni-layer applied for protection of the sample during cross section preparation, part of a WEL is visible, and underneath the two types of phases, one having been more strongly attacked by the etching procedure. EDS measurements were conducted on the three indicated areas, and the results are given in Table 8. It is obvious, that the WEL does not stem from adhesion of the steel counterbody, but consists of elements from the Cr60Ni40 alloy, with increased content of Si, as well as some C and O. From the Cr:Ni ratios it can be concluded that its composition corresponds to the Ni dominated austenitic phase (compare area 3), and not the Cr-rich one (area 2).

4 Discussion

4.1 Microstructural Alterations due to Friction Surfacing

4.1.1 6082 Aluminium Alloy

The aluminium alloy 6082 does not undergo phase transformation during the friction surfacing process, except for the possible dissolution and reprecipitation of small strengthening particles (mostly of Mg-Si type).

Although the initial microstructure of the studs used to generate the coatings is not known, it can be assumed that recrystallization towards a significant grain refinement to the measured value of 2.4 ± 1.6 µm has taken place during the friction surfacing process. In spite of the low grain size, the hardness in the coatings is only 80 – 85 HV5. The alloy 6082 is commercially available with a maximum hardness of 95 HB (≈ 110 HV15) in the T6 state, which is solution annealed and artificial hardened (precipitation hardening). The largest precipitates found in the 6082 FS coatings are up to 10 µm in size, but a high number are also in the ranges of several 100 nm or few 10 nm. Smaller lattice defects were also visible by TEM, but have not been identified. Generally, precipitates below 100 nm in size may be beneficial for the hardness [67]. 4 hour heat treatments of the coatings led to an increase in hardness up to around 100 HV5, which confirms that the coating material is initially not fully overaged. Precipitates found in the microstructure of 6082 alloy after standard artificial ageing are typically needle- or plate shaped Mg_2Si phases, which have been reported to have different lattice structures, depending on ageing temperatures (hexagonal [69] [95], cubic [96]). It is agreed though, that high temperatures and long times for annealing lead to the dissolution of thin coherent or semi-coherent needle-shaped phases, which are beneficial for the hardness, and foster the formation of incoherent rod-shaped or platelet Mg_2Si particles in the µm size range [67] [97] [98]. Within the FS coatings, predominantly spherical precipitates have been detected (Figures 12, 13).

In [99] the precipitation kinetics of different aluminium alloys have been studied. Here, standard heat treatment methods were used, by solution annealing at 540°C for 20 min, rapid quenching at different rates and a following artificial ageing treatment at 180°C for 4h. The critical quenching rate after solution annealing for 6082 alloy, for which no precipitation takes place, was found to lie above 1000 K/min, depending on small differences in alloy composition (higher content of alloying elements requires higher cooling rate). After such high cooling rates, the highest hardness was achieved by the following ageing treatment (110 to 130 HV1, depending on alloy composition) [99].

The translational speed during friction surfacing of 6082 alloy was 0.67 m/min for the samples discussed here. Considering that the stud diameter was 20 mm, the simple assumption can be made, that each point along the coating track was within the substrate/stud contact for 1.8 s. It also has to be kept in mind that a certain volume of the stud is heated up to the process temperature before it is deposited. Since the shortening rate of the stud is not known, the time at temperature of each material volume can only be guessed. The length of a single deposited layer was not more than 1 m, and with the named translational speed that results to a process time of less than 2 min for the steady state deposition stage. The cooling rate of the layer was not determined either, but the samples could be removed from the fixation with bare hands after few minutes. All these considerations lead to the conclusion, that it is quite probable that due to the short process time no complete solution annealing has taken place, although the additional energy introduced through plastic deformation will have accelerated solution processes.

It is reasonable to assume that during friction surfacing thin or small precipitates were dissolved, if they were present in the initial stud material at all, while larger ones were spheroidized due to the high degree of plastic deformation [98]. The subsequent cooling rate can be estimated to be in the range of several 100 K/min, which would allow some reprecipitation to take place. Still, the temperatures from which the cooling (and precipitation) starts are high, which may lead to the formation of unfavourable types of phases. Although it was possible to increase the hardness of the FS coating material by an ageing treatment at 170°C during 4h, phases of reddish colour formed (see Figure 22). These $CuAl_2$ phases are typically found after overageing, and are highly detrimental for the corrosion properties of the material [67].

4.1.1.1 Deformation and Recrystallization Mechanisms

The grains in the 6082 FS coating are partially flattened, particularly close to the coating surface, and are in the size range 2.4 ± 1.6 µm. For 6082 alloy deformed by HPT, lower grain sizes between 200 nm and 1 µm have been reported, fairly independent of the deformation temperature [100]. Still, 6082 is a widely used alloy, and investigations on friction surfacing and friction stir welding of this material are available. In [101] the grain size in friction surfacing layers was measured by optical microscopy to be 4.2 ± 1.8 µm, although the applied grain boundary etching procedure (Weck's reagent) may lead to unreliable results, since aluminium is difficult to etch. The hardness measured in theses coatings was ≈ 90 HV0.2, comparable to the values detected in this study (≈ 86 HV0.2). In [102] (friction surfacing) and [103] (friction stir welding) grain sizes of ≈ 2.6 µm and 2.3 – 2.8 µm are reported respectively.

While some sub-grain boundaries are visible by EBSD and TEM, these are seldom and most grains are surrounded by HABs. This fact and the low grain size imply that dynamic recrystallization has taken place during friction surfacing. The cooling rate and the time-temperature history of the material is not exactly known, and so it cannot be negated that there was possibility for static recrystallization to occur, too. Still, the partially high dislocation density (and gradients), and the high lattice distortion (up to 4°) within some grains point to an ongoing deformation during the crystallization of these respective grains.

The quite homogeneous grain size and the presence of lattice misorientation along the grain boundaries indicate a cDRX process, as expected for aluminium alloys [104]. A flat, non-equiaxed shape of recrystallized grains from severe plastic deformation was also found in accumulative roll bonding of different aluminium alloys and steels [43] and was discussed in [102] for a FS 6082 layer. In the latter work, EBSD analysis was conducted on the cross section of an FS stud within the formerly plastified tip material, as well as the corresponding FS layer. It was found that the grains in the stud are sheared in the process to very thin dimensions, and in the centre of the layer are stretched almost parallel to the rubbing interface. Substructures evolve and transform into HABs as the material approaches the substrate surface. These sub-grains and grains in the plastified stud tip material are slightly smaller (≈ 1.4 µm), than the grains in the applied layer (≈ 2.6 µm).

It can be concluded, that some limited grain growth may have taken place after the termination of the surfacing process. Still, transformation of cell structures into HABs seems to be the dominating mechanism, which is confirmed by the presence of several grains with similar orientations adjacent to each other. The accumulation of dislocations at triple points may have led to the formation of very small grains in between several larger ones. Although the grain size in dynamic recrystallization depends mostly on the deformation temperature and the strain rate, it has been shown that for 6082 alloy the strain rate is the most powerful determining factor, while the temperature has little effect [100] [105]. One possible reason for this finding could be the presence of second phases, which have a strong influence on strain hardening, but may reduce dislocation mobility at all temperatures before they are dissolved. An effective interaction of precipitates with dislocations is visible in Figure 19 and Figure 20.

As to the bonding it has to be stated, that no obvious mechanism was recognizable in the present study. While light-optical microscopy and EBSD imaging show, that the substrate material adjacent to the bonding line is plastically deformed, it does not undergo recrystallization. Since the temperature can be assumed to be similar to that of the coating material in direct contact, the introduced strain will not be sufficient to trigger recrystallization. Thin, sheared layers of both coating and substrate material along the bonding line have been observed by TEM, so mechanical mixing can be excluded from the possible bonding mechanisms.

4.1.2 NiAl-Bronze

The multiphase microstructure of the NiAl-bronze complicates the interpretation of the microstructural evolution during friction surfacing. Although the temperature during processing was not measured, the colour of the flash close to the interface with the substrate was bright red, indicating temperatures in the range of 850 to 950°C (Figure 118). According to phase diagrams from [106], a Cu-10Al-5Fe-5Ni alloy will completely attain the crystal structure of high-temperature solid-solution β-phase (bcc) in a temperature range between ≈ 920 to 1200°C. At lower temperatures it undergoes a decomposition into either $\beta + \gamma_2$ (intermetallic compound) or at slightly lower temperatures and Al-contents into the more stable $\alpha + \kappa + \beta$ configuration. At temperatures below 790°C, the remaining β-phase will decompose into $\alpha + \kappa$, too [106]. So, during friction surfacing the (at least partial) transformation of α-phase is certain, and the dissolution of the κ-phases in the high-temperature β-phase probably occurs only partially. The grain size of the globular α grains in the NiAl FS coatings is in the range of several µm, while the acicular Widmannstätten-phases have lengths up to several 10 µm. Compared to the former cast state of the material, a significant grain refinement has occurred. But, while it is well possible that DRX proceeded during deformation, the phase transformation and diffusion processes during cooling do not allow the definite identification of according microstructural features. The observed grain refinement could also be due to SRX from a high degree of deformation. Grains fairly free of dislocations and the presence of lamellar grain boundary precipitates point towards static processes. The presence of stacking faults and dislocations blocked by precipitates visible in some grains are indicative of ongoing recovery.

Interesting with regards to the progression of phase formation in the NiAl-bronze FS coatings is the distribution of the α grains relative to the regions composed mainly of small spherical phases. Obviously, the α grains have formed first, since they are of clear globular or acicular shape, while the dark-etching multiphase regions fill the volume between them. It is not probable that the small spherical phases were present during deformation, staying separated from the regions of later α grains. The above observations lead to the assumption, that during surfacing the material will have been mostly in the β-phase, containing possibly little κ-phase. The growth or transformation of α grains seems to have occurred earlier than the main κ-precipitation, with the result of α-phase containing only small amounts of precipitates. This may have been assisted by the enhanced mixing of alloying elements by the deformation, and the high cooling rates assumed for friction surfacing, which allow for supersaturation of the solid solution. The remaining β-phase with an increased content of solved alloying elements decomposed later during cooling into a very high density of small spherical phases, retained by a relatively low volume of α-matrix. The larger κ_{II}-phases from the cast state are not found in the coatings, since due to their size they would need more time to grow by diffusion processes, than there is available. The difference in shape of the α grains can be explained by variations in the cooling rates between the upper and lower regions of the coating layer, or by different peak temperatures, since the heat radiation into the air above the coating might not be of the same magnitude than the heat conduction into the machine table below.

The interface between the coating and the substrate is not a sharp line, and distinguishable only by the presence of martensite or bainite laths in the heat affected zone. It is quite wavy, pointing to some deformation of the substrate surface material during surfacing, before its phase transformation during rapid cooling. Still, macroscopic mechanical mixing can be excluded from the possible bonding mechanisms due to the phase morphology which is clearly different in the coating and the HAZ material. It is rather more likely, that bonding is achieved for these self-mating materials by self-diffusion and the achievement of a metallurgical bonding of the coating material to the surface of the substrate, which is activated by heat and frictional deformation during the coating process.

4.1.3 CP4M Tool Steel

The microstructure of the steel coatings is quite homogeneous and fine. This can easily be explained by the process of friction surfacing, in which the coating material is heated, heavily deformed and rapidly cooled.

The temperature reached during the process was not measured, but from the martensitic microstructure containing retained austenite it can be assumed that it must have been above austenitisation temperature. The maximum temperature during friction surfacing of a 1.5 wt.% C-steel was measured in [107] to be 1075°C, for rotational speeds of the stud of maximum 2500 min^{-1}, while no information is given about the translational speed. Still, the temperature is high enough for complete austenitisation. The deformation during the process is an additional aid to the solution of carbides and an even distribution of alloying elements in the deposited material. Since no former austenite grain boundaries are visible after the martensitic transformation in the coating material, no conclusions can be drawn from the microstructure as to the occurrence of dynamic recrystallization. But since the martensite plates have lengths only up to few micrometres, a low austenite grain size before transformation can be assumed.

The high hardness of the coatings in the range of 800 HV, and the low size and number of detected carbides point to a very high cooling rate which inhibits diffusion processes.

While the hardness of the presented single and the two layer coatings is very high (800 – 820 HV0.2), within the four-layer coating significant hardness fluctuations were found (627 – 828 HV0.2). The HAZ directly underneath the coatings frequently was found to be harder than the unaffected substrate material, and even the coating (≈ 870 HV0.2), but in a depth of about 1.5 mm, usually significant softening is found. This can be understood from this steel’s capability for both primary and secondary hardening to similarly high values. So, both an increase in hardness as well as a decrease may be caused from the heat input of applying one or more layers by friction surfacing, by secondary hardening if alloying elements are still in solution, or by overtempering of the martensite respectively [108].

Obviously, the samples’ size and the method are not representative for repair welding e.g. of large forming dies. Still, the complexity of the involved mechanisms becomes clear, and while the coatings are quite hard in all cases, the overlying hardening and softening effects must be regarded in order to avoid hardness fluctuations over a coated surface area, which might lead to an uneven wear progression during application.

The bonding line between coating layer and substrate is clearly visible from the change in microstructure. While some macroscopic deformation is visible in the HAZ, and the bonding line is wavy in some regions, again no mechanical mixing is visible. A slightly increased area amount of retained austenite and a very high hardness in the HAZ directly adjacent to the bonding line are supposedly mainly due to the heat input, and possibly the applied pressure. Again, the most probable bonding mechanism seems to be metallurgical bonding by (self-)diffusion processes.

Along the bonding lines of both substrate and coating as well as in between coatings frequently a seam of small oxide inclusions is found. Since the plastified material from the stud tip will be osculating densely to the counterface during the process, the interface can be assumed to be closed fairly airtight. So, the small oxide particles are assumed to stem from fragmentation of the oxide layers present on the materials' surfaces before coating. Due to the low size and globular shape, these particles have no significant negative influence on the bonding strength. Even more so, primary carbides in the surface of the cast substrate material seem to be bonded to the applied coating layer as well. These findings are supported by the conducted bending tests, in which no signs of coating delamination were found, and all samples – with and without coating – failed in a similar manner and within a shared scatter band of stress and strain at fracture, due to the brittleness of this hard steel.

Cracks found in CP4M FS coated samples were located in the substrate material underneath the lack of fusion close to the edge of the bonding line. It can be understood that here a step in the acting stress (and maybe strain) within the substrate material due to the friction forces occurs during the process. The load on the material may also be intensified by temperature gradients, leading to an increased risk of crack initiation within the brittle cast steel, particularly in the presence of large primary carbide conglomerates at this location.

In some multiple layer coatings, in which insufficient bonding was obtained, this was located in positions, where the acting pressure and/or rotational sliding speed during friction surfacing are expected to be low. This is generally the case in gaps between lower layers that are supposed to be filled, or in the centre of a layer applied overlapping the previous one. For geometrical reasons, in those positions plastified material may be squeezed in, but not be applied with a significant sliding motion between surfaces and with a lower pressure. When the offset between overlapping layers was chosen too large, the lack of fusion of the lower layer was not bonded to the substrate, as is the case for adequate positioned layers. In order to obtain metallurgical bonding by (self-)diffusion processes, an activation of the surfaces by increased temperature, relative sliding and a sufficient contact pressure (leads to slip between roughness peaks) and with that a sufficient contact area are needed. These mentioned parameters will determine the time necessary to achieve bonding [104].

4.1.4 Cr60Ni40

As discussed earlier, the microstructure of cast Cr60Ni40 alloys is quite complex despite the rather simple phase diagram. The dendritic microstructure consists of two types of areas, which obviously are mixtures of different phases. One exhibits eutectic lamellae and the chemical composition was found to roughly match the eutectic, with a slightly increased Ni content. The second one contains approximately 60 wt.% Cr, which equals roughly the composition of the Cr-rich bcc-crystal just below the eutectic temperature (Figure 3). The needle-shaped inner structure found in such regions was described in [109] as Ni-rich Widmannstätten precipitates, which form – possibly via an intermediate hexagonal β-phase [93] – during cooling with the decrease in Ni-solubility, and are assumed to be embedded in the remaining Cr-rich solid solution phase. The larger, Ni-rich precipitates, which are also found within the Cr-rich regions, seem to have formed earlier than the finer Widmannstätten needles, since they are more bulky in shape (Figure 45 (d)), and have a composition similar to the one of the eutectic regions. Even though in EDS measurements some process-related deviations in the quantitative results must be expected, it is clear that the cast material is not in a complete equilibrium state. Since this material was industrially manufactured by centrifugal casting, an economically sensible cooling rate would have been chosen.

During the process of friction surfacing forging temperatures are reached. The colour of the glowing flash during the process is light yellow, pointing to temperatures above 1200°C (Figure 4). At this temperature range, according to the phase diagram, the alloy in equilibrium should consist of two phases, the fcc Ni-crystals containing up to 47 wt.% Cr, and the bcc Cr-crystals with up to 38 wt.% Ni dissolved in them. The flow of two different phases during the application of the coating layer can still be seen in the coatings' macrostructure. Due to the rapid cooling, the composition of the two phases was frozen within the two types of phase regions found in the microstructure. The composition in the Ni-austenite was in average 52 wt.% Cr to 48 wt.% Ni and in the former Cr crystals it is 63 wt.% Cr to 37 wt.% Ni. This relation of composition implies that during friction surfacing, not the equilibrium Ni and Cr phases have formed. Instead, what is identified in the coatings as Ni-austenite still has roughly the eutectic composition. It can be assumed that during processing the eutectic lamellae were dissolved and a solid phase of eutectic composition was deformed, in parallel to a second phase of the composition of primary Cr-bcc phase. This is understandable taking into account that the process of friction surfacing proceeds within only a few minutes. Dissolution at high temperatures is enabled and enhanced by mechanical deformation, while during fast cooling only limited diffusion of the elements in solid solution into their equilibrium phases is possible.

While the Ni-crystals completely preserve their crystal structure during cooling, although being highly supersaturated, the bcc Cr-crystals decompose into the same Widmannstätten-phases as found in the cast material, only of finer morphology. The nature of the fine internal substructure could not be identified by TEM diffraction, only the bcc Cr was detected. From the macroscopic composition of these phase regions and the very low solubility of Ni in Cr at room temperature it is clear, that some kind of Ni-rich phase has segregated from the solid solution.

The grain size during friction surfacing can still be determined from the two types of phase regions in the coating material and it is quite low, in the range of several 100 nm to several µm. While the internal substructure of second phases in the former Cr bcc crystals does not allow to observe any deformation or recrystallization mechanisms within these regions, a number of features are visible within the austenitic Ni phase. Dislocation density gradients within grains, the presence of substructures formed by polygonisation and the presence of small twins point to a concurrent acting of deformation and recovery or recrystallization processes, which also explains the low grain size.

The microstructure described above is obviously not stable at elevated temperatures, when diffusion is enabled. The heat treatment experiments show several mechanisms, based on hardness measurements and light-microscopical observations.

While at the lowest heat treatment temperature – 500°C – a constant decrease in hardness over time was detected, the intermediate temperatures – up to 650°C – revealed a hardness maximum after 5h. This shows that after initial recovery processes, precipitation hardening presumably from the supersaturated solid solution austenite phase occurs. After 10h treatment a stable hardness of around 500 HV0.2 with a low variance is reached, except for the high temperature of 700°C, for which a drop in hardness to 400 HV0.2 implies overageing. This is supported by microstructural observations, which show that in a sample treated at 700°C, precipitations form quickly within the austenite phase and grow to a lamellar shape after 10h, leading to a very fine and homogeneous optical appearance of the microstructure. In comparison, at 550°C, the formed precipitates are significantly smaller and the two types of phase regions are still clearly discernible by optical microscopy after 10h heat treatment, in spite of a low spread of measured hardness values (± 25 HV0.2).

The bonding line between coating layers and substrate is macroscopically straight, and locally slightly wavy on a microscopic level. It can be discerned by the change in microstructures, and in the polished state by the different colours of the two alloys. Again, a seam of small oxide particles is present along the bonding lines, both between substrate and coating as well as between coating layers. When the offset between overlapping layers was too wide, in addition to the insufficient bonding of the lack of fusion of the lower layer to substrate and between the layers, a thick layer of oxide formed in the interface. Here, the contact was not adequately sealed from oxygen, because either the pressure was not sufficient or there were gaps present between the surfaces for geometrical reasons.
Although mechanical intermixing on a microscopic level cannot be ruled out, since it would be disguised by the seam of oxide particles, metallurgical bonding by diffusion is the probable major joining mechanism. It may act between the lack of fusion and the substrate during overlap coatings and also explain the fact that there seems to be no detrimental influence of precipitates from the coating present directly on the bonding line. Between coating layers, differences were found for the bonding appearances, between the realisation of overlap at the advancing or the retreating side. While for advancing side overlap a smooth bonding line with the familiar small oxide particles was found, during retreating side coating heavy intermixing of the two layers is visible from the flow lines of the different phase regions. Still, no voids or other defects were observed also for retreating side overlap coatings, although here more and larger oxide particles seem to be present.

The fact that segmentation cracks formed vertically within Cr60Ni40 FS coatings when water spray cooling was applied during the process shows that this brittle material reacts sensitively to the cooling rate. It does need a certain time at increased temperatures to reduce internal stresses from the deformation by relaxation or static recovery processes.

4.2 Effect of the Microstructure on the Wear Behaviour

4.2.1 6082 Aluminium Alloy

The samples from 6082 FS coatings, both heat treated and in the as-coated state, undergo severe wear under cavitation. Although only surface roughening was evaluated, which may also be caused by deformation and extrusions, particularly in the beginning of the loading, it is obvious from the profiles of the worn surface areas that a significant amount of material is being removed. Strain hardening may be expected to occur, but cross sections show plastic deformation of the surface material even after 120 min test duration. No incubation time was detected. The heat treated samples, of which the hardness was increased by about 20 HV5, show even higher wear depths, than the as-coated sample. This difference might be due to scatter of the values, or could be caused by the disruption of precipitates, which are larger in size after the heat treatment. In any case it can be concluded that the applied cavitation testing causes severe failure of this soft material.

4.2.2 NiAl-Bronze

The results clearly show that the NiAl-bronze FS coated samples have a better resistance against cavitation erosion in distilled water compared to the as-cast material. The difference can be explained by the acting wear mechanisms. During the first 1 to 2 hours of exposure, both as-cast and coating material show deformation, pitting and extrusions typical for cavitation. In both materials, crack initiation takes place at phase boundaries and at the bottom of cavities. After 180 min, the different phases in each material become visible on the worn surfaces, due to their differing reaction to the loading. Areas on the as-cast material containing a high amount of precipitates are roughening, but areas of pure α-phase already exhibit disruptions and obvious loss of material. This tendency persists to the end of the tests at 410 resp. 450 min and is apparent in the large heavily worn areas, as seen in the confocal microscopy measurements. Possibly, the precipitates do not only promote crack initiation, but in later stages interfere with crack propagation and stabilise the material. Branching cracks seen within the α-phase both on the worn surface and in the cross sections underneath point to an intergranular propagation. This and their advancing 10 µm below the surface, where the forces from cavitation should be quite low, indicates that material loss has been promoted by crevice corrosion or corrosion fatigue mechanisms, which lead to the detachment of whole grains or large particles. With the coating, more ductile features are observed. Extrusions are seen on the α-phase after 180 min of exposure and at later stages deformations around cavities are visible. Cracks also seem to initiate at phase boundaries between α- and decomposed β-phase regions. However, they propagate close to the surface at low angles to it and often within regions that seem to be deformed. Grain boundary attack has not been observed with coated samples.

The improvement in cavitation erosion resistance can therefore be attributed to the more ductile behaviour of the coating material and the absence of corrosion.

4.2.3 CP4M and GP4M Tool Steel

Despite the very fine martensitic microstructure present after FS, the wear behaviour of the cast and hardened state and the coatings is not too distinct. Still, the higher hardness and homogeneity of the coatings leads to some differences in the extent of the single wear mechanisms. Tribochemical layers are found on all samples. At 60 N normal force they dominate and delaminations are found to be more prominent after 1 million cycles. These delaminations are the result of surface fatigue and account for most of the wear volume measured. With increasing normal force, the delaminations become slightly deeper, from about 1 µm at 60 N to about 8 µm at 180 N. This can be explained by the distribution of stresses induced by the tribological loading. For low friction coefficients of 0.06 to 0.1, as measured in the present investigation, the maximum shear stress must be expected to be located in a certain depth underneath the surface, which increases with rising normal force [110]. This can cause fatigue cracks to initiate deeper inside the material. With increasing test duration, the number and size of delaminations increases, due to crack propagation with time. The higher wear volumes of the coatings, compared to the cast and hardened state, can be explained by their higher hardness, which indicates a lower ductility. This is detrimental to the fracture toughness and therefore to the resistance to surface fatigue. Occasionally, small defects in the surface were visible outside the wear scars, particularly in regions where two coating layers overlap (see Figure 107 (b)). Still, these can clearly be distinguished from the delaminations caused by the sliding wear. The grooves, which also appear on the worn surfaces, are probably caused by abrasion due to wear particles from the delaminated material. The higher hardness of the coatings is also the reason for a lower volume of piled up material around the worn surfaces compared to as cast samples, since less plastic deformation of the material must be expected.

It is known, that besides abrasive wear, adhesion is a major problem in sheet metal forming tools [111]. Wear takes place particularly at corner radii of the tools, along which the sheet material slides under high contact pressure. Often, depending on the forming application, a characteristic two-peak contact pressure distribution on one die radius leads to two localised wear regions [112]. Real acting contact pressures are difficult to determine, but can be assumed to be in the range of 100 MPa at the peaks [113]. Obviously, this value depends on the deformed materials' strength and thickness, as well as the geometry.

In the experiments discussed in the presented study, no adhesion was found on the worn surfaces. Also, the contact pressures during the tests are not known. From the dimensions of the worn surfaces after the experiments, the nominal contact pressure at the end of the test duration was estimated to be in the range of 765 MPa for 60 and 180 N normal force. In both cases, the size of the worn surface areas is independent of the test duration, which indicates that the wear of the balls mainly takes place during run-in within the first 50,000 cycles, and the sizes of the worn areas are very similar for the coated and uncoated samples. This supports the assumption, that during run-in wear takes place mainly on the balls until a contact situation is reached, in which the materials can resist the resulting contact pressure.

Assuming a wear volume of 200,000 μm^3 for 60 N normal force, for a test duration of 1 million cycles (see Fig. 9), and taking into account the width and length of the worn surface area on the samples, a theoretical overall wear depth of 0.18 µm can be calculated. This would equal to an average wear rate of 0.004 µm/h. With a wear volume of 600,000 μm^3 for 180 N normal force, the wear rate results to 0.012 µm/h. For 550 N normal force and a test duration of 50,000 cycles with a wear volume of 1,100,000 μm^3, a wear rate of about 0.44 µm/h would result. All of these wear rates imply that this tribological system runs under mild to ultra-mild sliding wear conditions. For 1 million cycles, the tripling of normal force from 60 N to 180 N also leads to a tripling of wear rates. For 550 N normal force, experiments were only run for 50,000 cycles, and the wear rate is more than proportionally increased, also suggesting that the wear does not proceed linearly over the test duration.

Taking into account, that the contact pressures are probably higher in the conducted experiments, than in real applications of metal sheet forming, and still only little abrasion and no adhesion takes place, a major discrepancy exists between the tribological situation in the experiments and in real forming dies. The main factor for this difference can be assumed to be the influence of the lubricant. In sheet metal forming, the used prelube is applied onto warm rolled metal sheets, firstly to protect them from corrosion. It is sprayed onto the sheets once to create a thin film, and the wax constituent in the lubricant ensures that a sufficient amount stays on the surface. In the following forming process, the thin film on the sheets lubricates the contacting parts. In the model experiments conducted, it was not possible to apply a thin film once before each sliding contact. Instead, the lubricant was steadily dripped into the contact. With this method, obviously a larger amount of lubricant is available within the contact. This can be assumed to have minimised abrasion and prevented adhesion mechanisms, therefore leading to very low friction coefficients, with low wear rates under surface fatigue mechanisms.

4.2.4 Cr60Ni40

The sliding wear behaviour of Cr60Ni40 observed in the present study is similar for cast material and coatings. The friction coefficient is effectively the same for all test parameters and both material states. No significant changes in wear mechanisms are found, and there is an increase in wear volume both with increasing normal force and test duration. Still, the coatings behave slightly better, always showing a lower wear volume than the cast material under the same test conditions, particularly for the longer test durations.

Taking into account the wear scar on cast Cr60Ni40 presented in Figure 112, it can be estimated that for a wear depth of approximately 70 µm and 25,000 cycles, the wear rate results to ≈ 2.8 nm per cycle, which is 1.4 nm per sliding contact under reciprocating sliding. Assuming the atom radius of Cr and Ni to be in the range of 140 pm, this means that with each sliding contact in average approximately 10 atoms have been removed. Considering this low wear rate, it is not probable that the grooves found on the wear scars on the flats are due to abrasive wear by microcutting, which would lead to higher wear rates. It can be assumed, that the grooving of the worn surface is instead caused by a ploughing mechanism, plastically deforming the material in the surface. Plastic deformation of the Cr60Ni40 alloy under frictional shear forces is possible, as seen in the cross sections (Figure 115 and Figure 116). After repeated deformation, fatigue mechanisms may lead to the removal of material (delaminations), particularly when WEL have been formed. The small beads of material adhering to the balls' surfaces, for which EDS measurements reveal that they originate from the flats, containing high amounts of Cr and Ni, lead to a high surface roughness and carry out the ploughing. Still, especially in the earlier stages of the tests, some abrasion probably took place on the balls, since they are slightly flattened. The elliptical shape of the wear scars on the balls is due to the fact, that more wear took place on the flats, leading to the trough shaped wear scars and an elliptical contact area.

Both cast and coating material show the ability to deform under the tribological loading, although the Cr60Ni40 alloy is considered to be brittle. Within the white etching layers, caused by adiabatic shearing, even more localised deformation has taken place. While the deformation gradient generally means that the material does not tend towards cracking by surface fatigue, the WEL are very hard and brittle and are therefore the cause for the observed delaminations.

The coatings, although they show the same mechanisms as the cast material, seem to be capable of more localised shearing. The deformation gradients are narrow under the worn surface, and wider WEL with less delaminations are present. This can be explained by the finer and more homogeneous microstructure. The smaller grains and the higher hardness may be a better support for the WEL and lead to a more even distribution of shear stresses from the friction force.

4.3 Nature and Application Spectrum of the Friction Surfacing Process

From the numerous alloys that have been joined by friction surfacing (see chapter 1.1) and the results presented in this work, it is obvious that this method opens up the possibility to produce coatings from materials and material combinations that cannot be realised by conventional surfacing techniques. The typical difficulties, including the oxide films on aluminium, the low viscosity of the liquidus of cast materials (NiAl-bronze, Cr60Ni40) and unwanted microstructure components after solidification (CP4M tool steel) are avoided, at the price of low welding speeds and relatively low output of coating material. The method will not replace standard techniques and applications, but it will be interesting to see which new materials and material combinations will be introduced into technical applications in the future, thanks to novel joining and processing techniques, as friction surfacing is. Some major aspects need to be regarded when considering to use the friction surfacing process.

It is a type of severe plastic deformation process at elevated temperatures. The high degree of deformation can only be accomplished by the aid of the frictional heating and the pressure on the plasticised material volume from the applied axial downforce. Since the plastic material in the stud tip is not restricted, some of it will necessarily leave the contact along the edges of the stud and form the flash.

The material may comprise different crystallographic phases during the coating process, than it does at room temperature, which can be easily recognised from corresponding phase diagrams. So, steel can be processed in its ductile, austenitic state, even when this is not stable at room temperature. Still, the high degree of deformation and the short process time may lead to the presence of non equilibrium phases during the coating process, by affecting solution and diffusion processes, as well as because of dynamic restoration processes.

Adhesion of the coatings on the substrate is achieved by (self-) diffusion and metallurgical bonding. The bonding line can usually be clearly distinguished from the change in microstructure between substrate and coating and does not show mechanical mixing. Still, it is often wavy on a microscopic level and the substrate may show macroscopic signs of deformation. This implies an intense interaction of the two surfaces, necessary to achieve sound bonding. Relative motion between contacting bodies removes oxide films and activates the surfaces. Bonding defects are found when the pressure was locally insufficient, leading to the lack of fusion at the edges of layers. Similarly, when applying an overlapping layer, the surface over which the stud is guided is not flat, and where the pressure is too low due to geometrical reasons, a lack of bonding may result. On the other hand, it is a fact that the lack of fusion of a layer may be closed by applying an overlapping layer with suitable process parameters. This shows that, if the temperature is high enough, relative sliding between the heated unbonded material of the lower layer and the substrate, which may well occur on a microscopic level under the forces from the application of the upper layer, is sufficient for bonding.
It can be concluded that for bonding quality the pressure is most relevant.

Most important to understand the basic mechanisms of friction surfacing, is to keep in mind how the necessary heat is generated and distributed. In the early phase of the process, directly after the stud contacts the substrate surface, dry friction acts between the solid bodies, with high friction forces and fast, localised heat generation. When the process parameters are chosen correctly, the heat will then raise the temperature in the stud material and due to thermal softening it starts to flow (see chapter 1.1.1). Now, rotational sliding between the stud material and the substrate surface diminishes and maybe even stops. Deformation now takes place within the plasticised stud material and heat is generated from internal friction. It is crucial for the success of the process to reach an adequate state of plasticised material, which depends on the heat balance, which in turn is determined by heat generation (rotational speed / axial pressure) and heat flow (translational speed / cooling measures). In addition, of course the involved materials play a role, specifically their heat conductivity and capacity, and their mechanical properties at elevated temperatures. It was found to be very difficult to produce coatings from grey cast iron, because this material quickly assumes a low viscosity which in turn does not allow adequate internal friction to occur (unpublished results from M. Beyer, Helmholtz Zentrum Geesthacht, Germany). On the other hand, the shifting away of the heat source from the interface into the stud allowed to generate coatings from steel on aluminium substrate as reported in [20], although the bonding did contain a significant amount of defects.

For wear and corrosion protection purposes, friction surfacing layers provide some general advantages, including homogenisation of alloying element distribution, refinement of grains and phases, spheroidisation of precipitates and solid solution strengthening by supersaturation. Only in the case of 6082 aluminium alloy no significant wear resistance was found after friction surfacing, which is presumably also the case for other microstructural states of this material. It is a structural alloy for aerospace applications and not intended for wear situations.

5 Summary

This work focusses on interpreting the microstructure evolution of four different commercial alloys during friction surfacing, and investigating the resulting effects on the wear behaviour.

Coatings were successfully generated from 6082 on 2024 aluminium alloy, NiAl-bronze (CuAl10Fe5Ni4) and CP4M tool steel (≈ X50CrMoV5-1) on self-mating substrate, as well as from Cr60Ni40 alloy on Nimonic 80A at Helmholtz Zentrum Geesthacht, Germany. Single or multiple layers were accomplished free of defects when suitable process parameters were chosen.

The microstructure of the materials was studied by light- and electron microscopy, before and after friction surfacing, and its evolution is discussed taking into account the high degree of deformation, estimated temperatures and cooling rates of the FS process. Cavitation and reciprocating sliding wear tests were applied to the coatings and to samples of conventional microstructures. The materials' reactions to the loading are compared and the effect of the microstructural changes obtained by friction surfacing on wear resistance are discussed, with respect to each alloys' range of applicability.

In the aluminium alloy 6082, no phase transformations occur during friction surfacing, except for the dissolution of hardening precipitates. Dynamic and static recovery bring about a low grain size of few micrometres. Nevertheless, the hardness of the coatings is not at its possible maximum. It can be assumed that no complete solution annealing took place due to short processing times, and after the material was applied precipitation started at high temperatures, which will have led to the formation of unfavourable phases. An artificial ageing treatment increased the hardness but brought about large, unwanted Cu-rich precipitates, both in coatings and substrate. So, post-cladding heat treatment is no realistic option, the more so for practical reasons, when components are being coated. Wear testing showed ductile behaviour and high wear rates under cavitation, but the structural 6082 alloy is not intended for wear applications.

For both the NiAl-bronze and the tool steel it can be concluded that the materials are in a single phase state at the temperature at which they are deformed.

In the case of the bronze, the high-temperature solid solution β-phase (bcc) prevailed when the material was deposited. Phase transformations from β to α + κ occur during cooling, which makes it difficult to draw conclusions on the deformation mechanisms. Still, a low grain size and traces of deformation in the crystal structure of the bronze α-phase imply that here also some dynamic restoration process were under way. It must be assumed though, that static recrystallization and recovery have played a role too. κ-precipitates in the coatings were found to be spherical and small (≈ 100 nm).

Regarding the wear behaviour, the NiAl-bronze FS layers showed good results. The lower size of the single phase regions, an expected higher toughness due to supersaturation of the α solid solution, as well as the small, spherical precipitates were found to be beneficial for the resistance against surface fatigue by cavitation, compared to the as cast state.

The steel was deformed during friction surfacing at temperatures in the austenite regime. This is clear both from the colour of the stud tip during the process, as well as from the microstructure found within the coatings. This consists of homogeneously arranged, fine martensite plates (length in range of 5 – 50 µm) enclosing retained austenite, and has a very high hardness (≈ 800 HV). Carbides found were always below 1 µm in size.

The steel FS coatings showed a similar wear behaviour as the conventional cast and hardened state under reciprocating sliding, dominated by tribochemical reactions and surface fatigue mechanisms. At very high contact stresses (550N normal force; 2,570 MPa Hertz' mean contact pressure) and at long test durations, when fatigue crack growth determined the wear rates, the high hardness of the coatings has a detrimental effect and leads to slightly higher wear volumes. In industrial metal sheet forming, where GP4M is used as tool material, adhesion and abrasive wear are expected to occur, contrary to the lab experiments conducted in this study, which can certainly be attributed (amongst other reasons) to the differing methods of applying the lubricant. Testing FS coatings from tool steel in the actual forming situation can be considered promising, since a high hardness and low size of phases are much more favourable to avoid adhesion and abrasion mechanisms, than fatigue.

Within the Cr60Ni40 alloy two different phases were present during the friction surfacing process. This can clearly be seen from the cross sections, which exhibit flow lines. From EDS measurements it can be concluded that eutectic phase regions transformed into a supersaturated fcc phase at the high temperature (≥ 1200°C). The second phase present during processing is a bcc Cr-rich one containing the maximum amount of Ni soluble at the eutectic temperature. While the latter decomposed during cooling into bcc Cr and fine, Ni-rich precipitates, the fcc austenite retained its microstructure to a supersaturated state at room temperature and precipitation of the alloying elements set in only when post-cladding heat treatment was applied. Grain refinement, the absence of the eutectic lamellae and the supersaturated solid solution phase significantly enhanced the wear resistance under cavitation (surface fatigue) and also slightly improved the wear behaviour under sliding wear (deformation, strain hardening and delaminations), compared to the conventional as cast state.

6 Outlook

It has been discussed earlier that friction surfacing is a niche process, compared to conventional high-throughput processes, but does have some specific advantages for certain applications. Still, there are some options to refine the process, tackle some of its drawbacks and extend some of its benefits.

The flash, which necessarily forms around the stud during the process, reduces the output and – more importantly – poses practical problems, e.g. by limiting the usable stud length or releasing chunks of hot metal into the surroundings due to the centrifugal force. As mentioned before, the pressure within the plasticised material, which causes the squeezing out of the flash material, is crucial for the cladding performance. While the problem may be partially solved by using a cutting device to remove the flash during processing, a possibility to avoid flash formation could be to constrain the plasticised material underneath the stud. This could be accomplished, e.g. by introducing a groove in the substrate surface, only slightly wider than the stud, which is then filled by the coating material. By this method, a geometrical situation is provided that allows to accommodate the pressure without material flowing out. Of course, this is not possible in all applications. Using a sleeve around the stud to retain material is also conceivable, but such a device will be subject to severe wear.

A powerful approach to tailor microstructures within the coatings could lie in a sophisticated heat management. For example, the precipitation behaviour in the 6082 aluminium alloy could be influenced in order to achieve a higher hardness. In combination with the low grain size achieved by dynamic recovery, exceptional mechanical properties might be within reach. Fast cooling to quickly lower the temperature below 200°C followed by measures to maintain the temperature at around 180°C for a sufficient period of time to form hardening precipitates may be a promising method [98] [99]. It must be considered though, that the coating process may be affected when cooling is applied concurrently. The degree of supersaturation and the size of precipitating phases may be influenced in all materials by controlling the cooling rate.

Measures for cooling or for holding the temperature after the coating has been applied influence temperature dependent, diffusion based phase transformation processes. In contrast, varying the temperature within the plasticised material during the surfacing process – within the operable window of process parameters – will affect the deformation behaviour. In the case of ongoing dynamic recrystallization, temperature changes will affect the rates of defect introduction and restoration, and with that the resulting grain size. Generally, with lower temperatures and resulting higher strength of the plasticised material, smaller grains may be expected. In addition, measures to influence the heat balance during processing (e.g. cooling or heating the stud and/or substrate) could affect the thickness of the "quasi-liquid layer" by shifting the shear plane (or volume) in the stud, in which the frictional heating is generated, closer to or further away from the substrate, which could be used to control coating thickness.

Drawing conclusions on the mechanisms acting during deformation from the microstructural features of the completed coatings, as done in this work, needs to rely on some assumptions. A more profound knowledge could be gained, if additional information was gathered during the processing. The evolution of the torque, in combination with concurrently measured temperature, could show the onset of dynamic recrystallization processes, if e.g. a drop in torque at constant temperature was detected. From a recorded shortening rate of the stud, the material volume involved in the process in a certain time interval could be estimated. Predictions on the resulting microstructure could be obtained from such information, and by consulting literature on severe plastic deformation at elevated temperatures, which is available for numerous materials.

Evidence found for the bonding mechanisms of the different material combinations is limited in this work. This is due to the fact that sample preparation for transmission electron microscopy was carried out by mechanical and ion polishing methods. The material along the bonding line and its vicinity was found to react differently to the polishing than the bulk coating and substrate material. Thinning was continued until sample stability deteriorated, since the material surrounding the bonding zone was removed readily by the applied methods. Except for the aluminium alloys, samples still were too thick along the bonding line to be penetrated by the electron beam of the used 120 kV microscope. It must be assumed that diffusion and/or deformation processes affected this material and increased its resistance to thinning. To further understand the bonding mechanisms, e.g. focused ion beam technique could be used to cut TEM samples directly from the bonding zone.

7 Figures and Tables

7.1 Figures

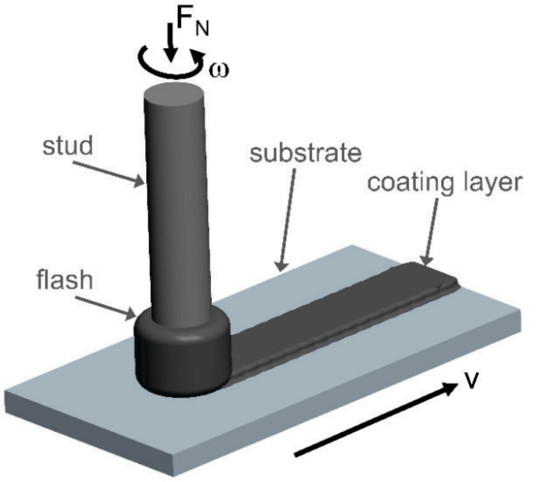

Figure 1: Scheme of the friction surfacing process.

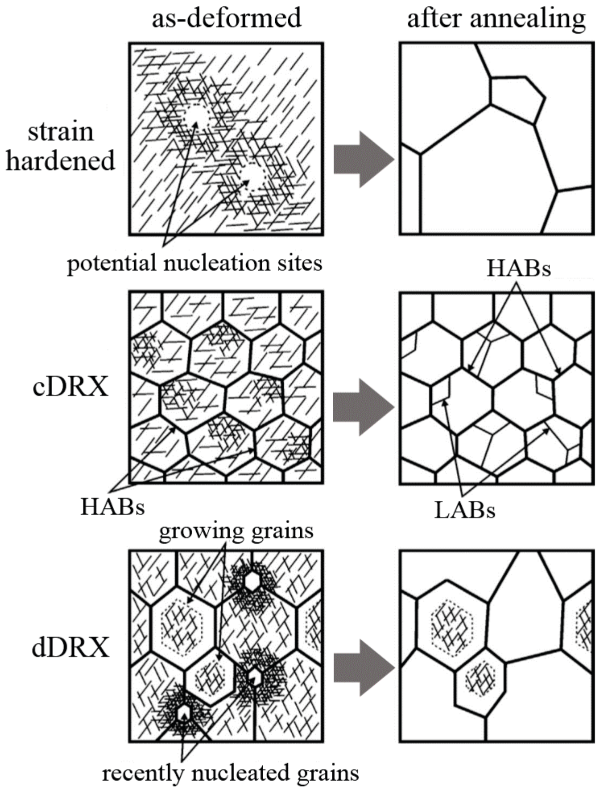

Figure 2: Scheme of basic microstructural differences between static recrystallization after pure strain hardening, continuous (cDRX) and discontinuous (dDRX) dynamic recrystallization according to [44]. (HAB – high-angle boundary, LAB – low-angle boundary).

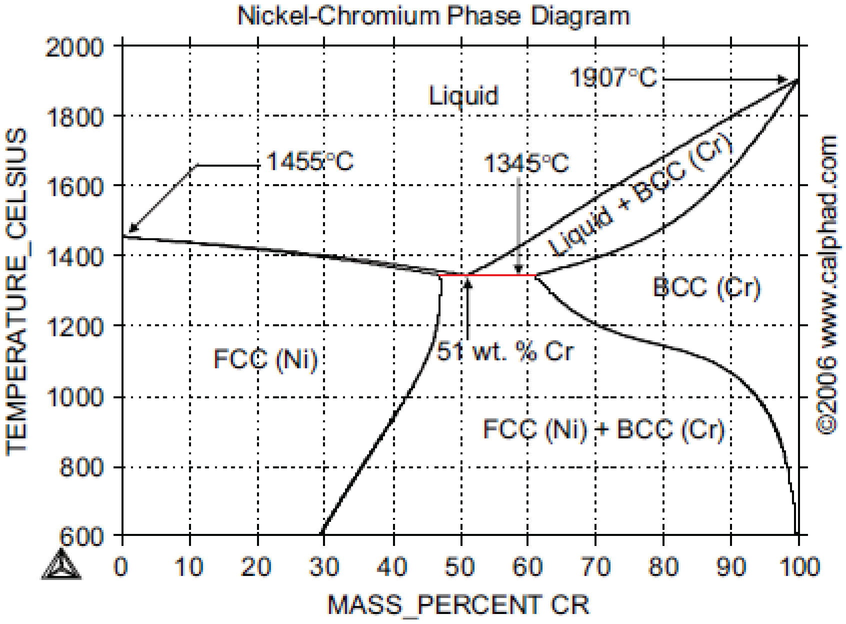

Figure 3: Phase diagram of Cr-Ni system [87].

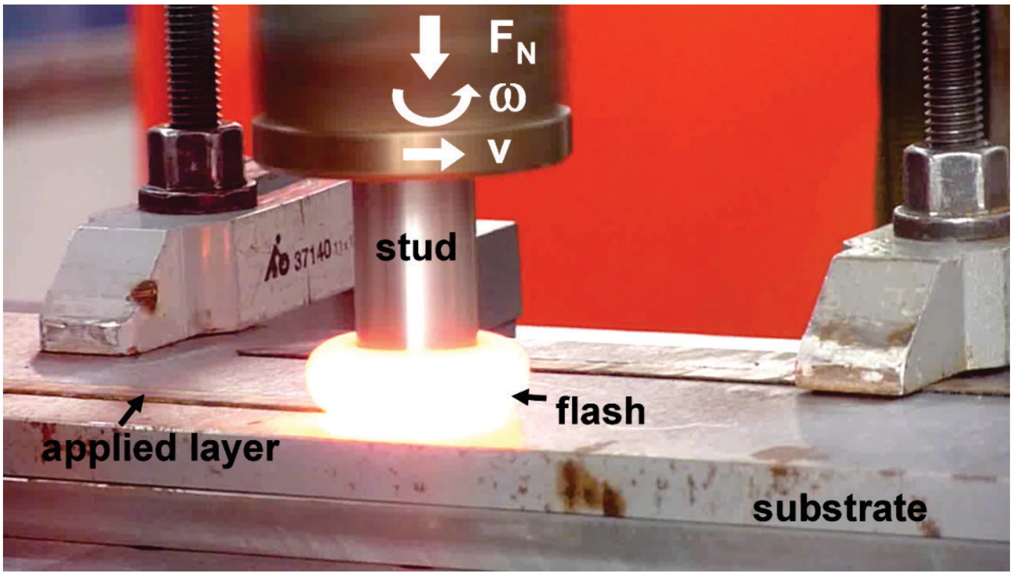

Figure 4: Detail of the friction surfacing process of Cr60Ni40.

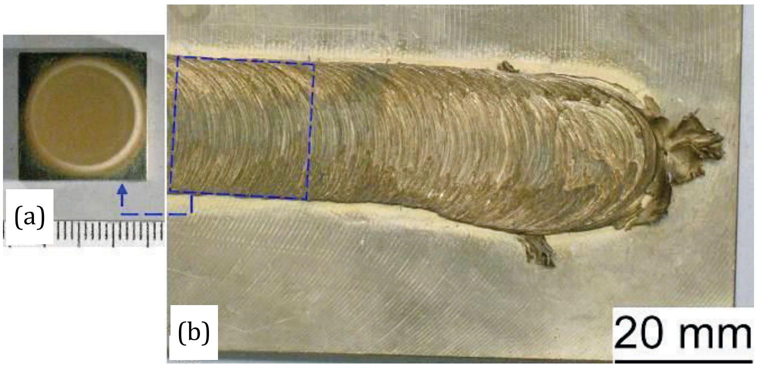

Figure 5: NiAl-bronze. Sample after cavitation test (a) and top view on part of single layer coating (b).

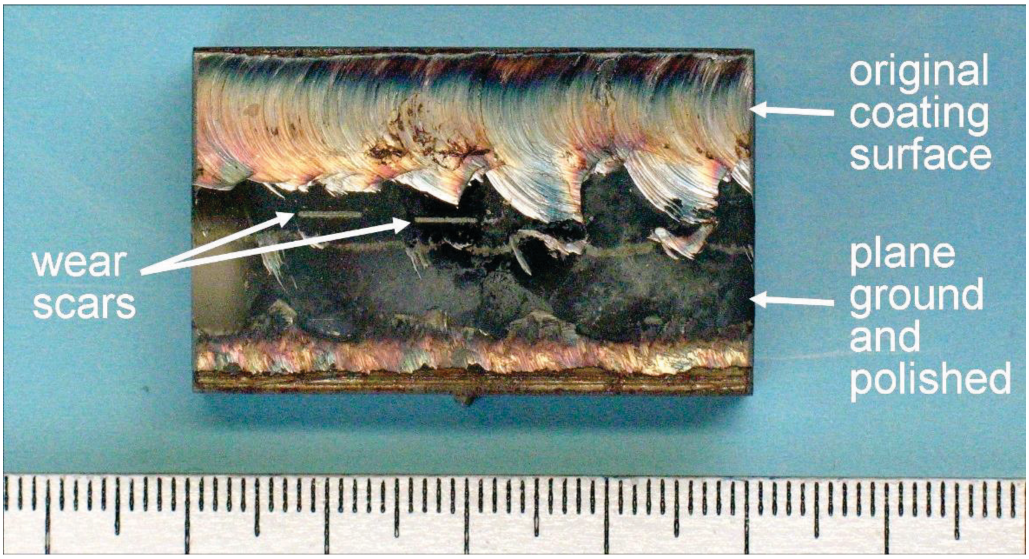

Figure 6: Sample from triple layer CP4M coating after sliding wear tests.

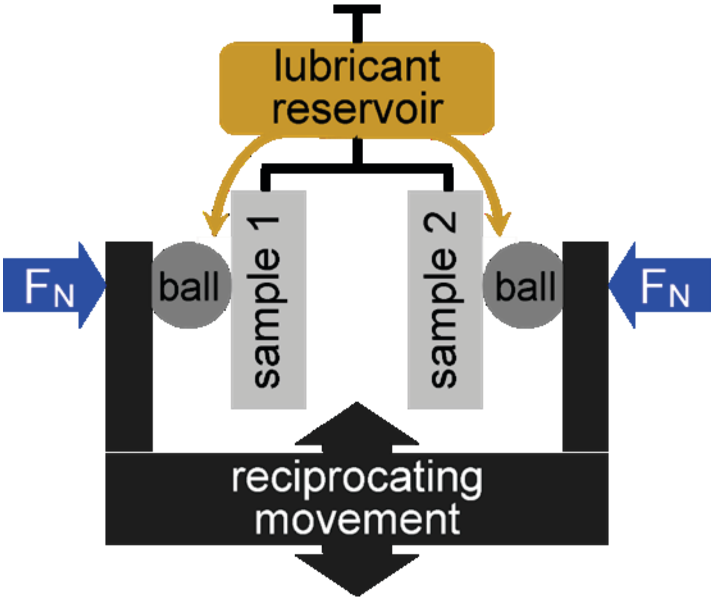

Figure 7: Scheme of the wear test-rig for reciprocating sliding.

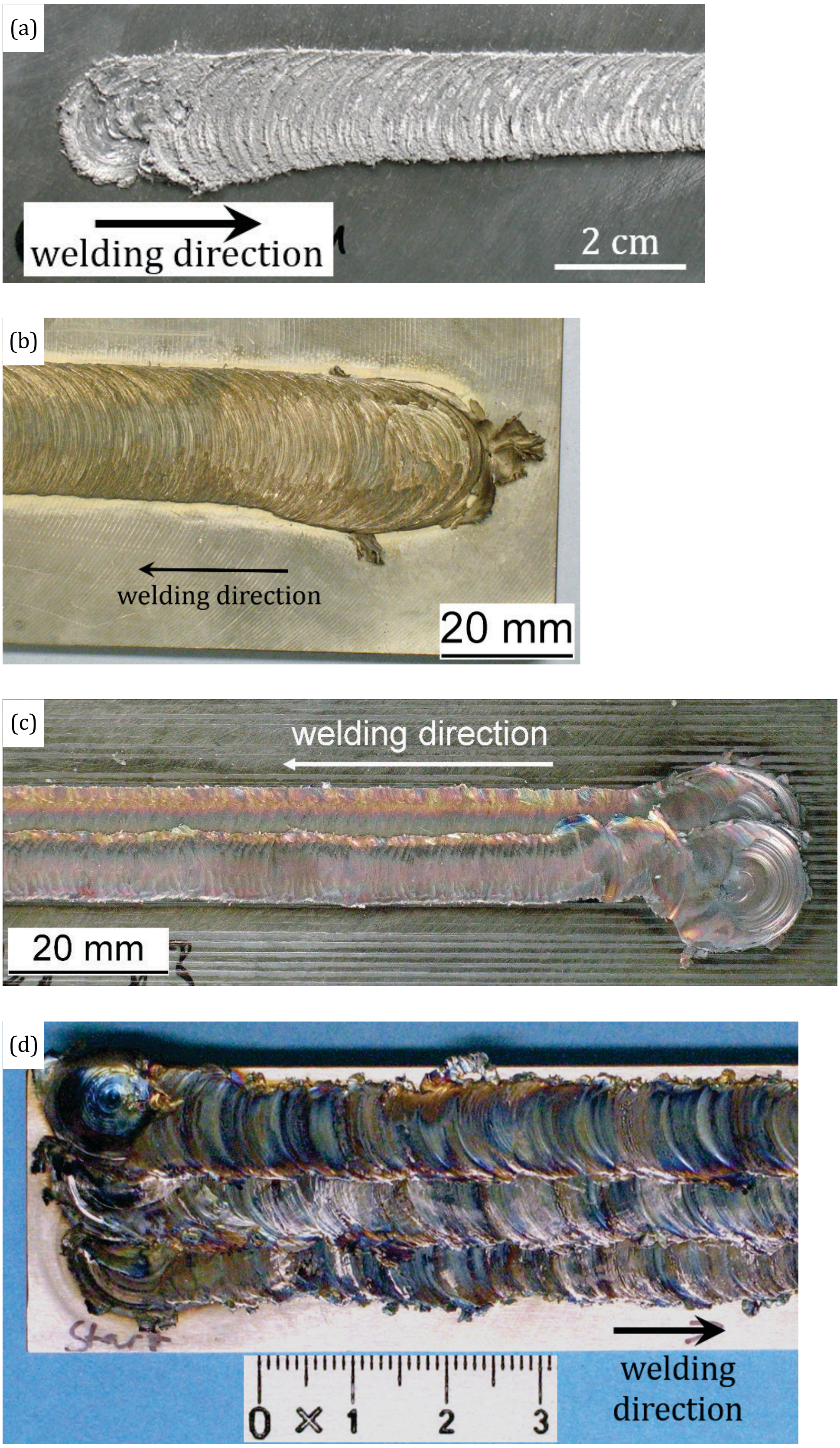

Figure 8: Macroscopic photographs of single layer coatings from aluminium (a) and NiAl-bronze (b), double-layer coating from CP4M steel (c) and triple layer from Cr60Ni40 alloy (d).

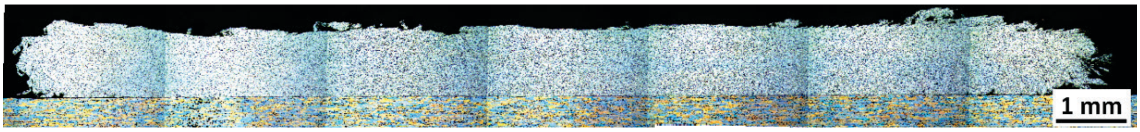

Figure 9: Cross section of a single layer 6082 FS coating.

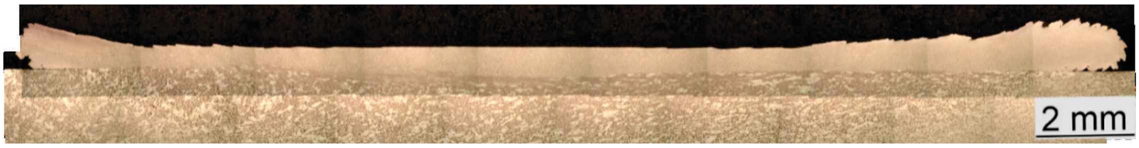

Figure 10: Cross section of a NiAl-bronze FS layer.

Figure 11: Cross section of a single layer CP4M coating, showing substrate, HAZ and coating with lack of fusion zones (arrows).

Figure 12: Cross section of a four-layer CP4M coating, also showing substrate and HAZs.

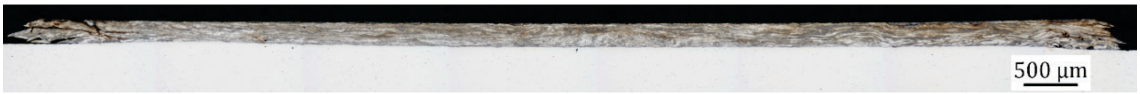

Figure 13: Cross section of a single layer Cr60Ni40 coating.

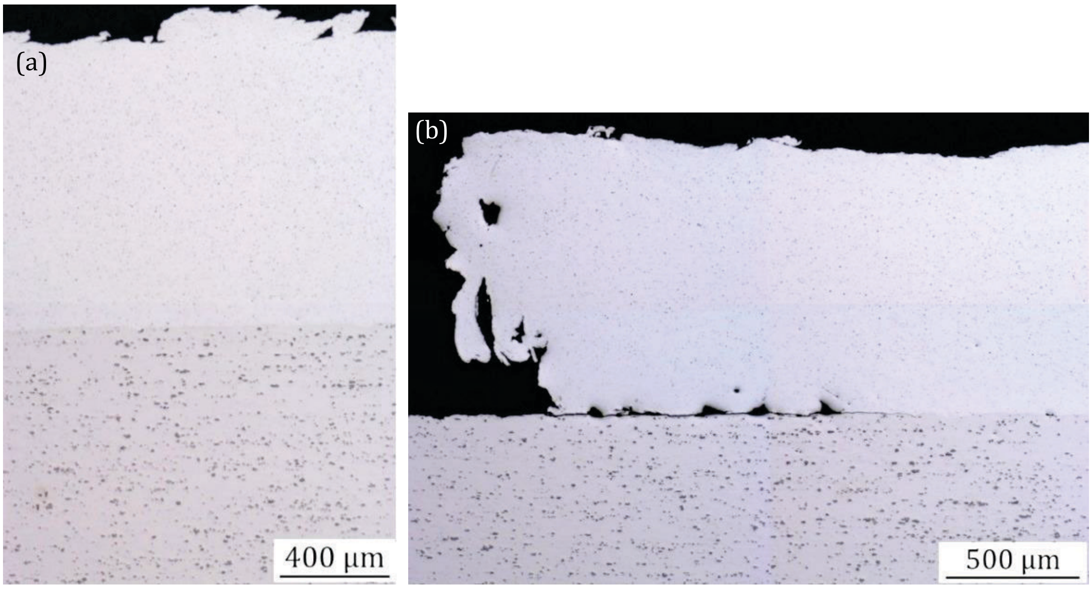

Figure 14: Cross section of a 6082 alloy FS coating on 2024 substrate, showing coating thickness and part of substrate in the coating middle (a) and the lack of fusion at the coating edge (b).

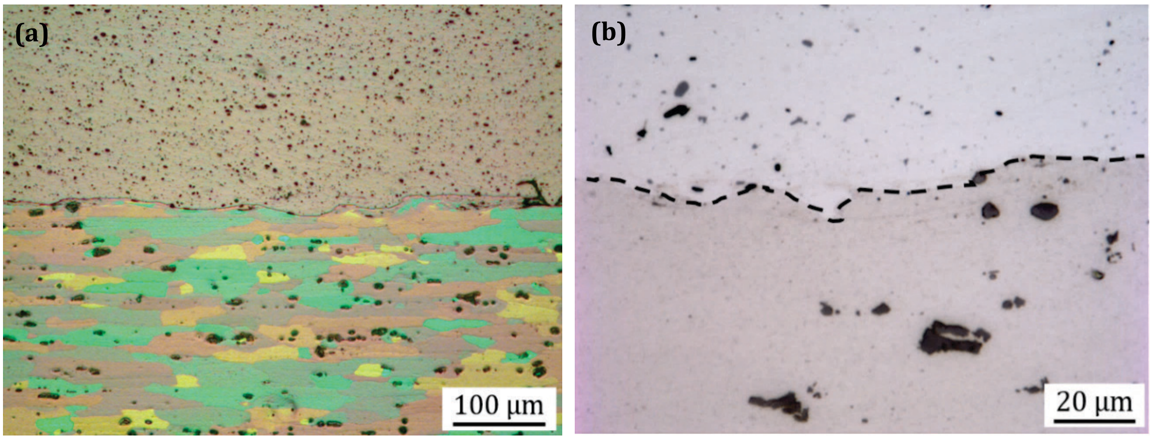

Figure 15: Cross section of a 6082 alloy FS coating on 2024 substrate. Etched, using polarised light (a) and in the polished state (b). The dashed line in (b) indicates the bonding line.

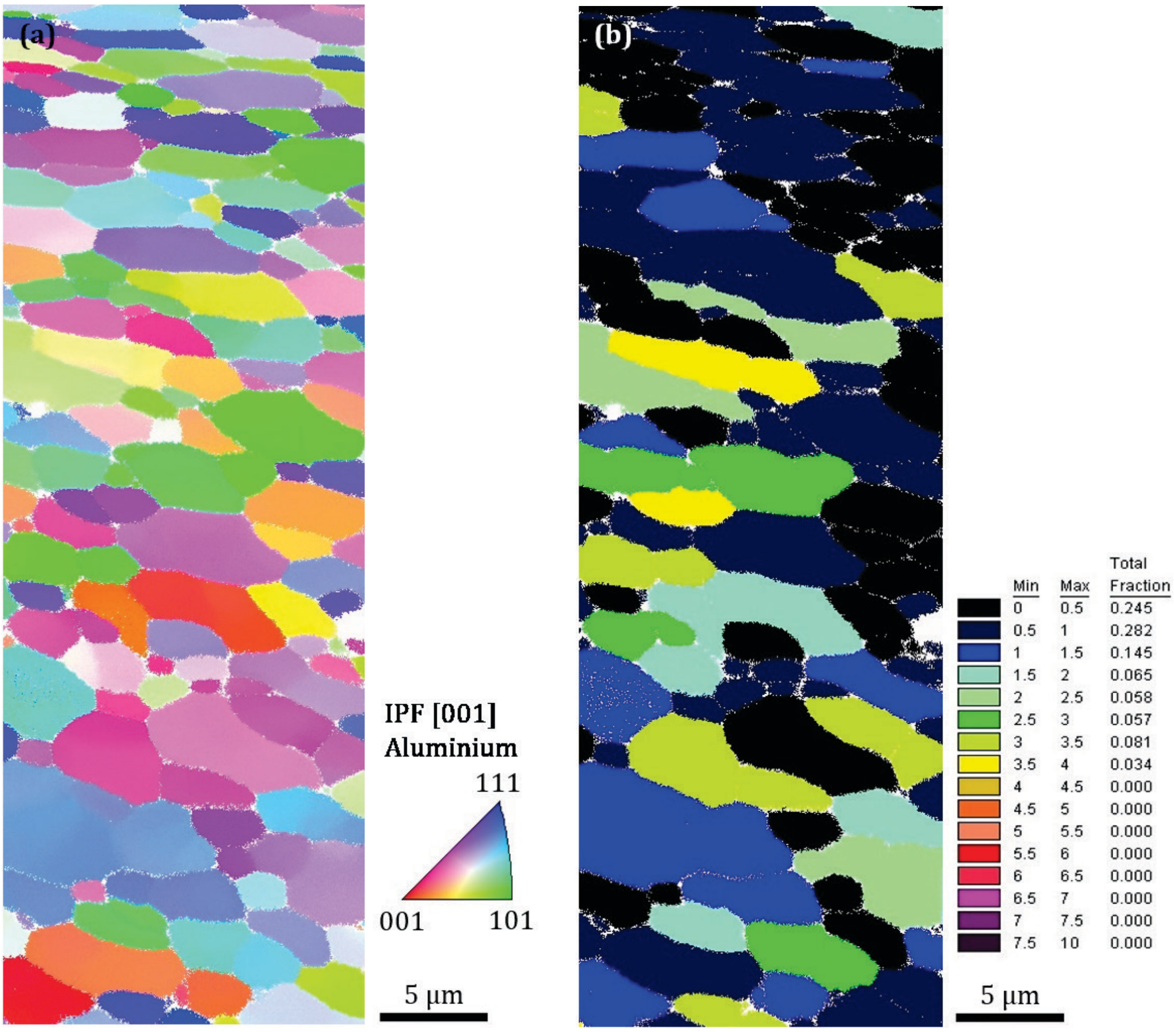

	Min	Max	Total Fraction
⬛	0	0.5	0.245
⬛	0.5	1	0.282
🟦	1	1.5	0.145
🟩	1.5	2	0.065
🟩	2	2.5	0.058
🟩	2.5	3	0.057
🟨	3	3.5	0.081
🟨	3.5	4	0.034
🟨	4	4.5	0.000
🟧	4.5	5	0.000
🟧	5	5.5	0.000
🟥	5.5	6	0.000
🟥	6	6.5	0.000
🟪	6.5	7	0.000
🟪	7	7.5	0.000
⬛	7.5	10	0.000

Figure 16: EBSD measurement of the microstructure of a 6082 FS coating. In the inverse pole figure (IPF) the colours represent the different orientations of the grains (a) and the grain orientation spread map (GOS) shows the standard deviation of the orientations measured on all points within each grain (b).

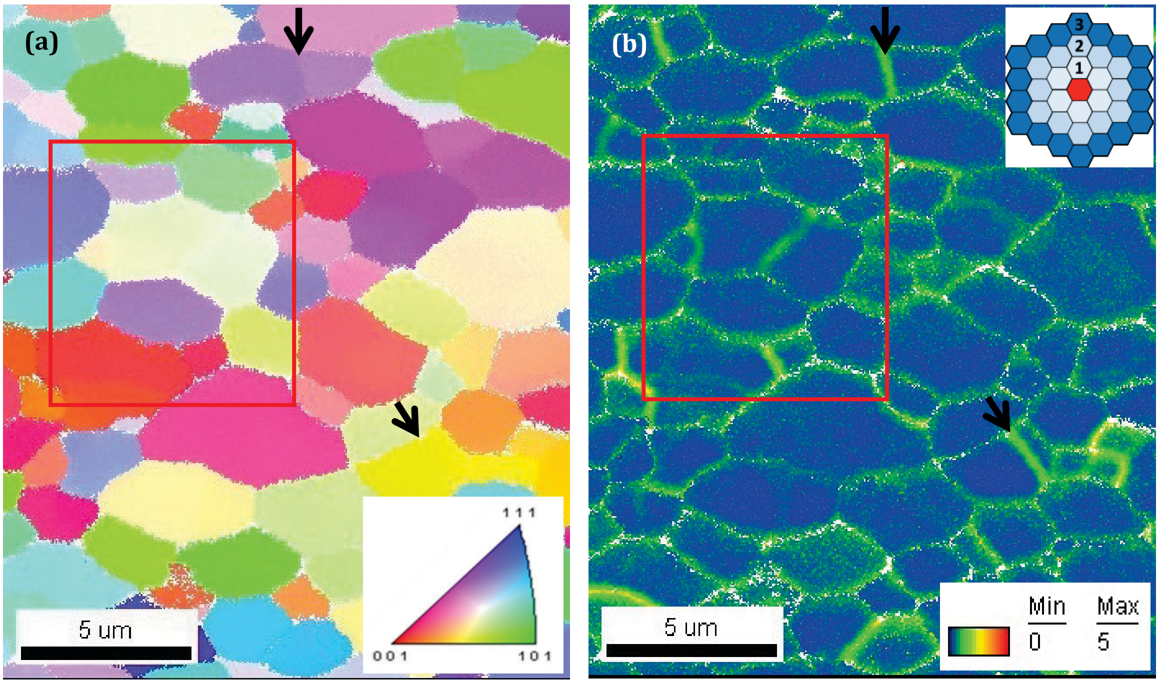

Figure 17: EBSD measurement of the microstructure of a 6082 FS coating. In the inverse pole figure (IPF) the colours represent the different orientations of the grains (a) and in the kernel average misorientation map (KAM) the angle of lattice misorientation for each pixel relative to points in five surrounding circles of pixels is presented (b).

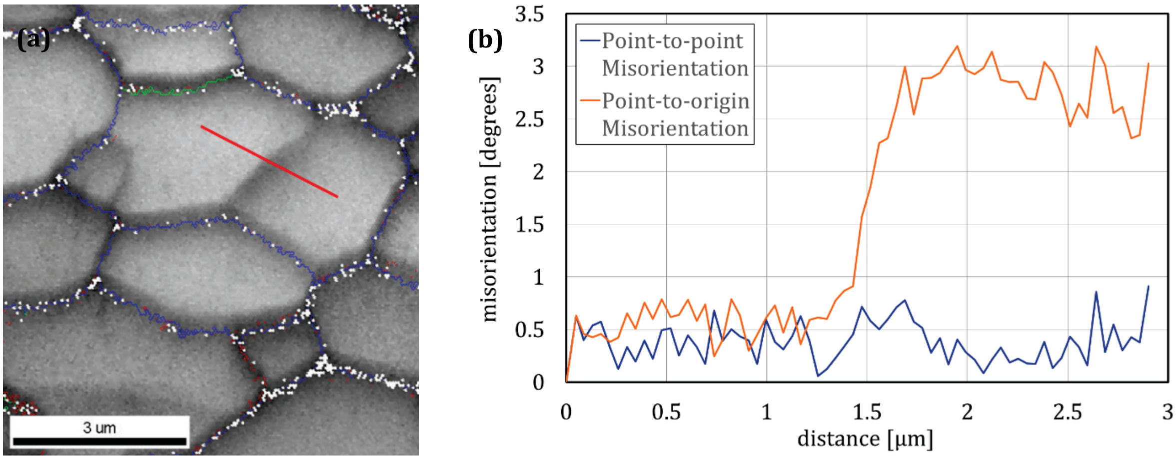

Figure 18: Detail of the EBSD measurement in Figure 17 (red box). In the image quality map grain boundaries are displayed in blue, if the rotation angle between neighbouring pixels is > 15°, in green for 5 to 15° and below 5° in red (a). The straight red line indicates the path along which misorientation angles between single pixels are presented in (b).

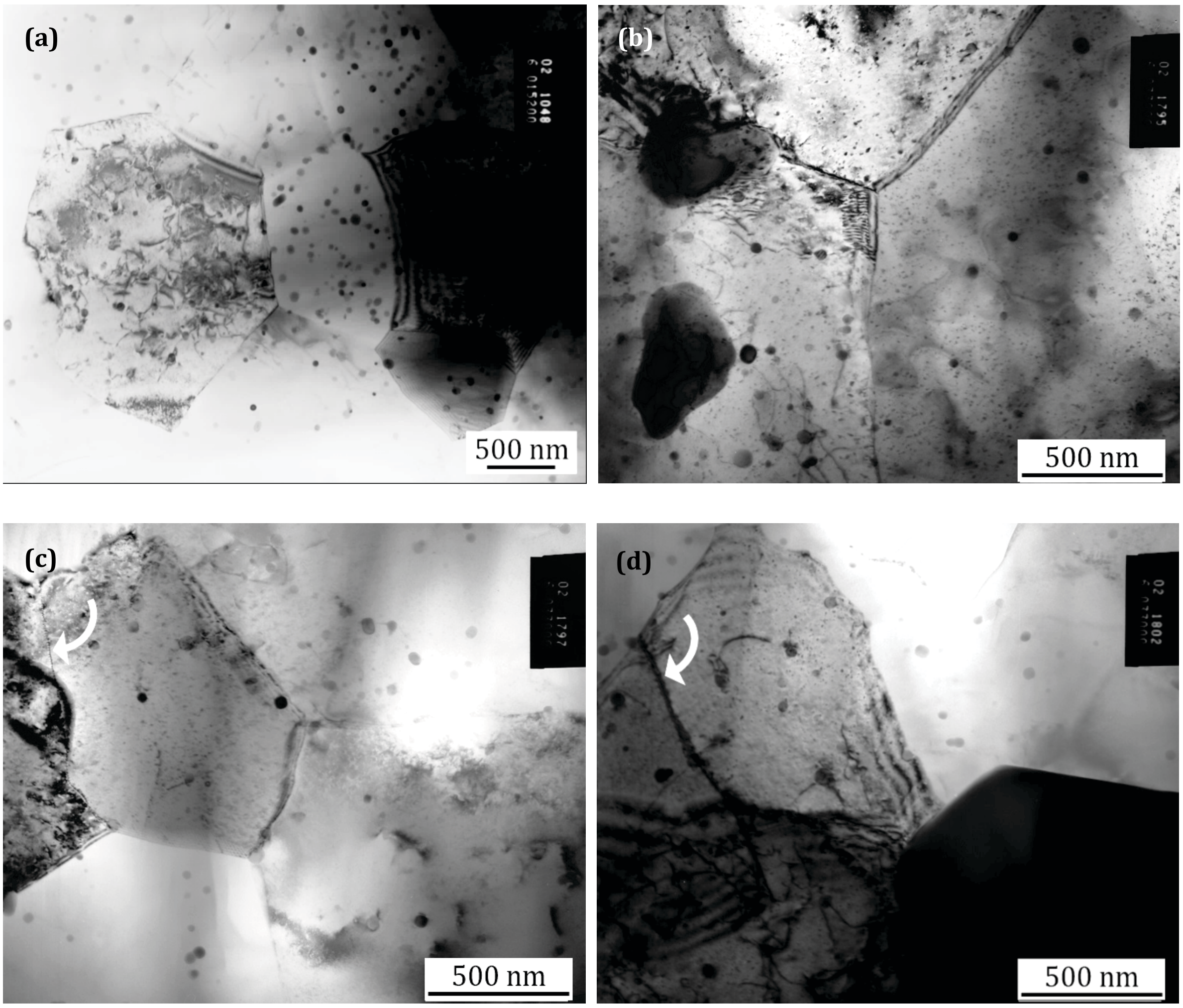

Figure 19: TEM images of 6082 FS coating microstructure showing small grains, low-angle grain boundaries (arrows) and precipitates (or lattice defects) in four discernible size ranges (< 10 nm (b-d); 10-50 nm (a-d); < 500 nm (b); > 1 µm (d)).

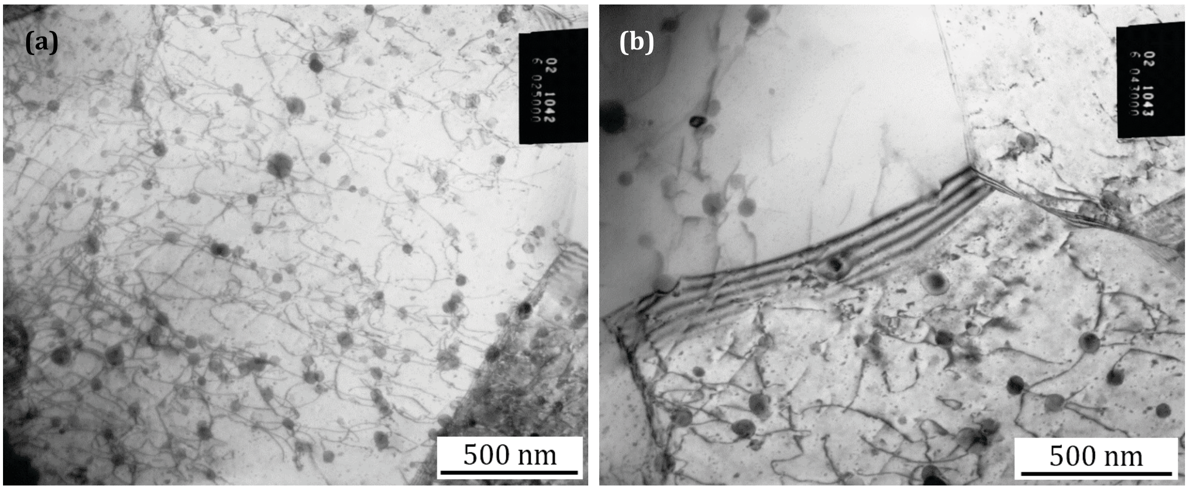

Figure 20: TEM images of 6082 FS coating microstructure showing high amount of entangled dislocations and precipitates in the size range 10-50 nm.

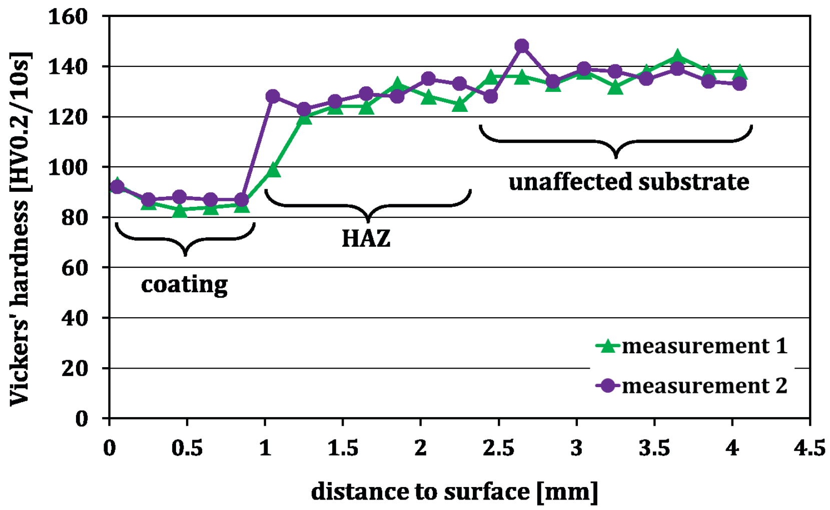

Figure 21: Hardness profile of single layer 6082 FS coating starting 50 µm underneath the coating surface.

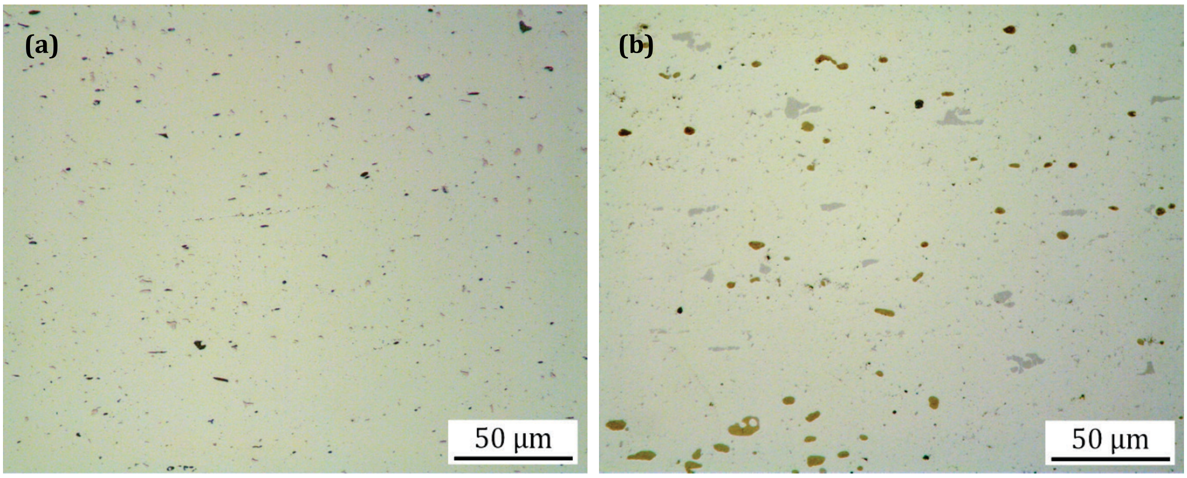

Figure 22: Microstructure of 6082 FS coating in initial state (a) and after heat treatment (170°C, 4h).

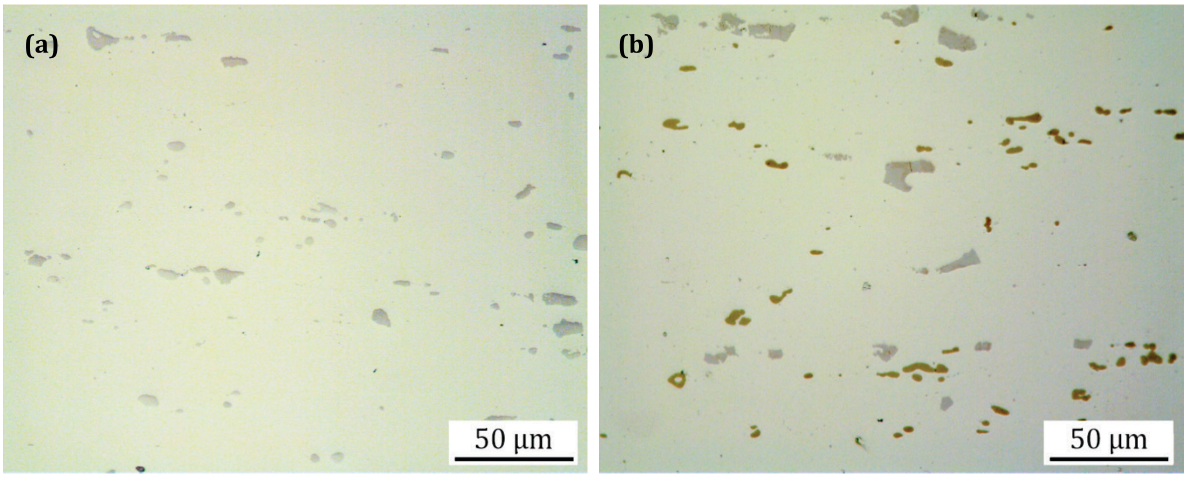

Figure 23: Microstructure of 2024 substrate in initial state (a) and after heat treatment (170°C, 4h).

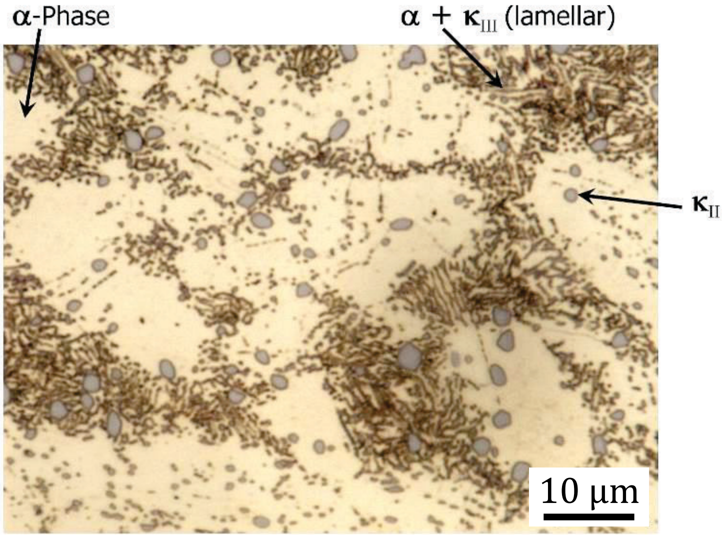

Figure 24: Microstructure of the cast state of NiAl-bronze in the substrate material.

Figure 25: Detail from a cross section of a single layer NiAl-bronze FS coating showing also part of the heat affected zone (HAZ) in the substrate.

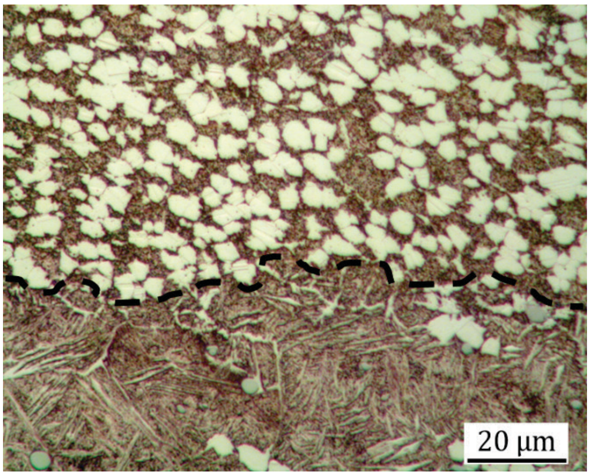

Figure 26: Detail from a cross section of a single layer NiAl-bronze FS layer; the dashed line indicates the bonding line between coating and substrate.

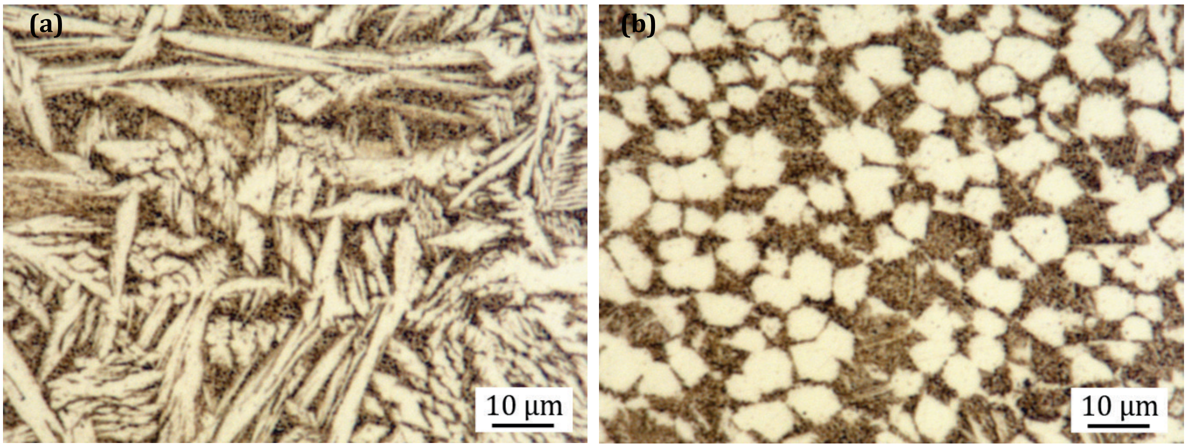

Figure 27: Microstructure of NiAl-bronze FS coating close to the surface (a) and close to the substrate (b).

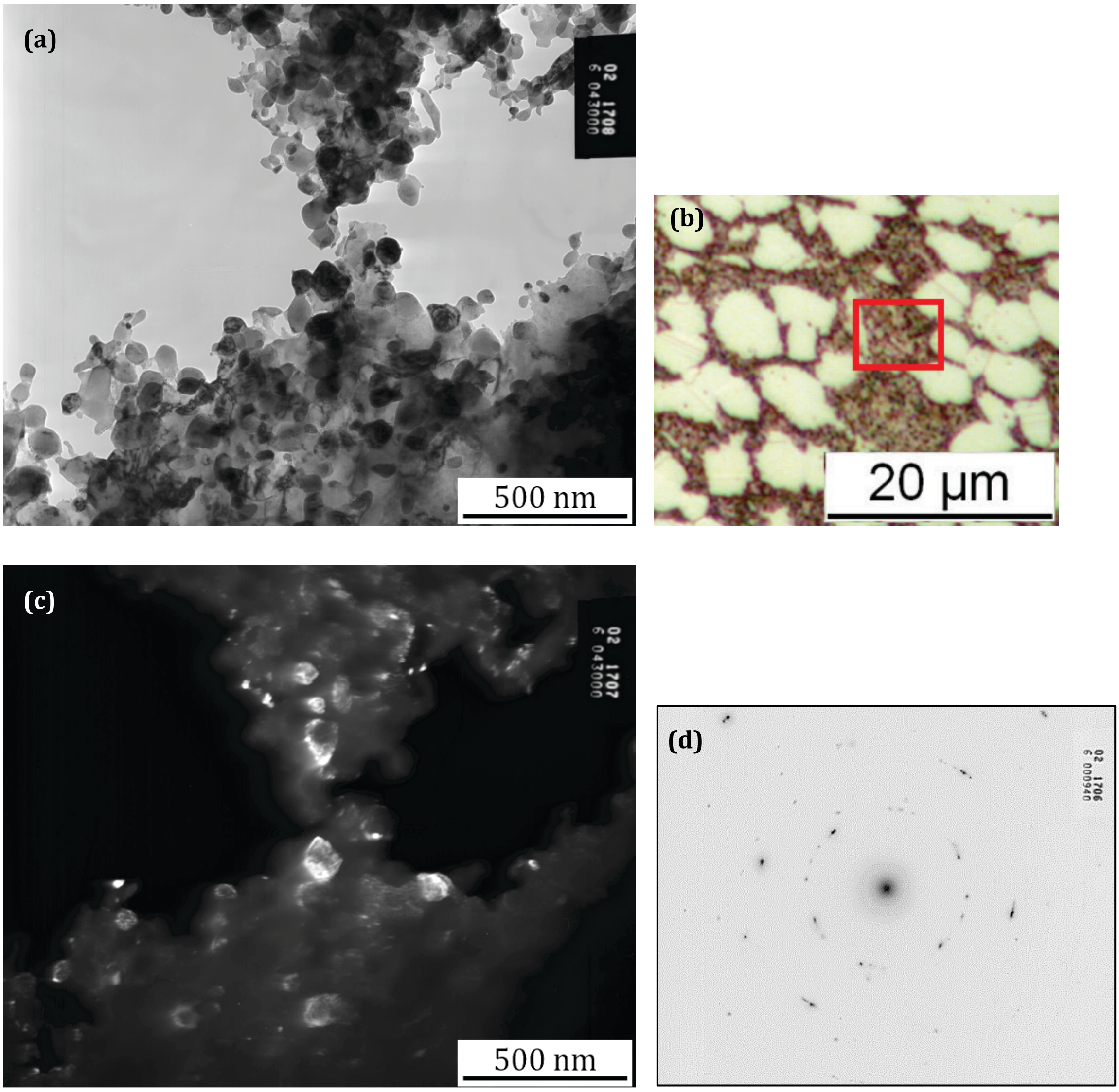

Figure 28: Microstructure of NiAl-bronze FS coating, showing spheroidisation of precipitates of the eutectic β-phase in TEM bright-field (a), light microscopy (b) and TEM dark-field (c). Diffraction (d) did not allow phase identification.

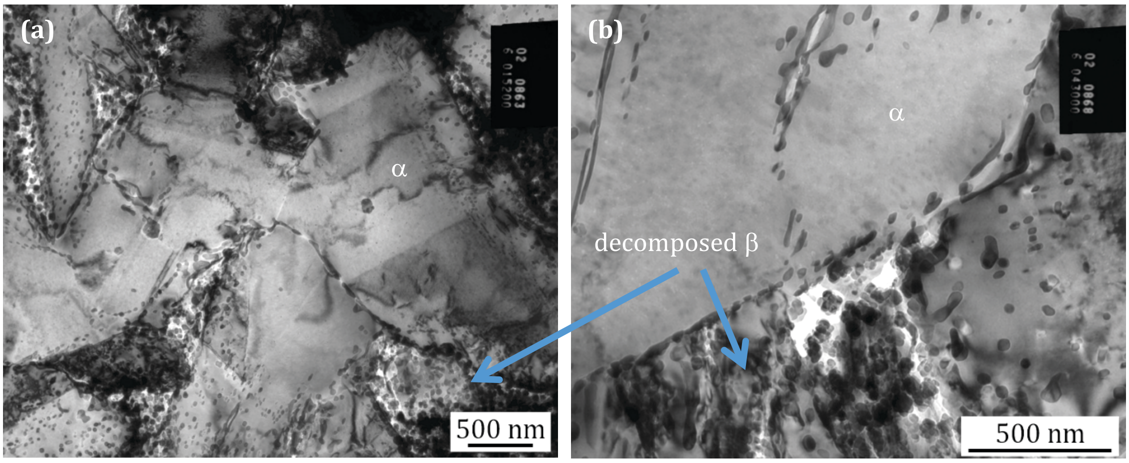

Figure 29: TEM images of NiAl-bronze FS coating microstructure at two magnifications. The two main microstructure constituents, α-solid solution and spheroidised quenched β-phase are discernible.

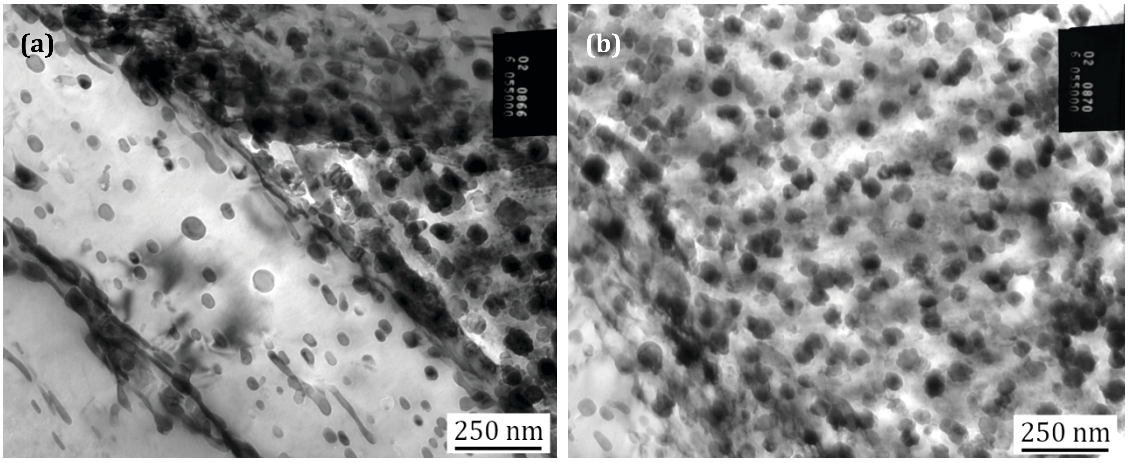

Figure 30: TEM images of NiAl-bronze FS coating microstructure, presenting stripes of α-phase and the spheroidised β-phase (a), as well as a region of the former eutectic β, containing mainly globular phases (b).

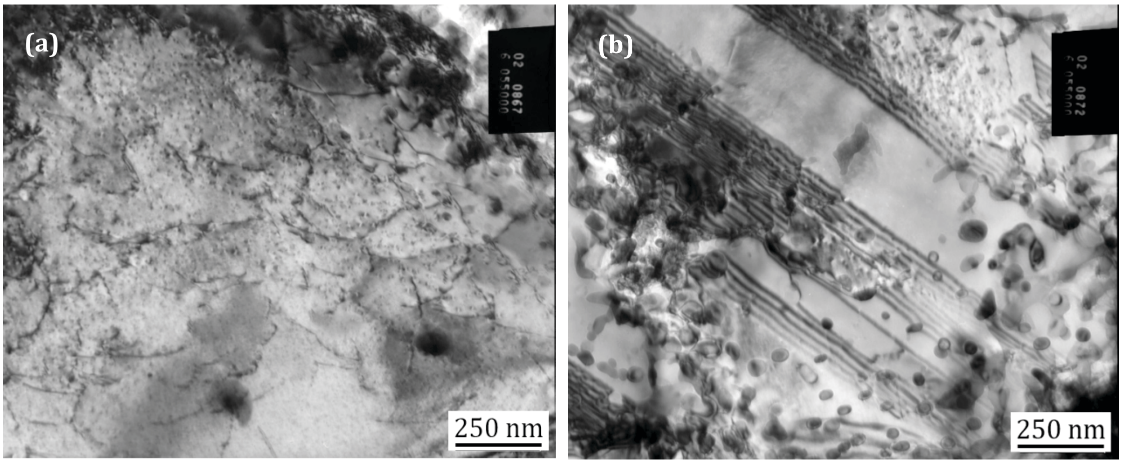

Figure 31: TEM images of a NiAl-bronze FS coating with dislocations and small precipitates (a) and stacking faults (b) in the α-phase.

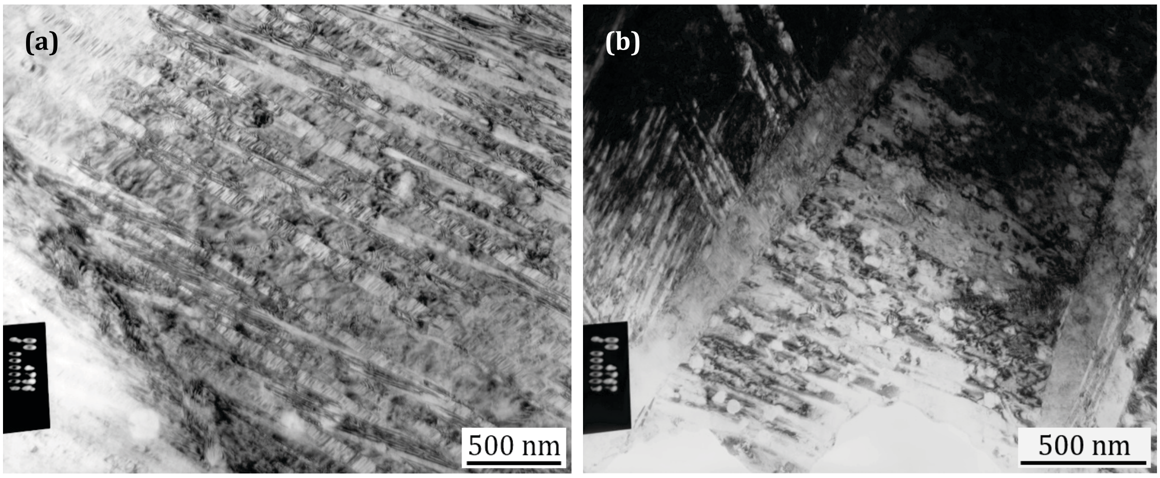

Figure 32: TEM images of the HAZ underneath a NiAl-bronze FS coating, in the region of martensite or bainite phases.

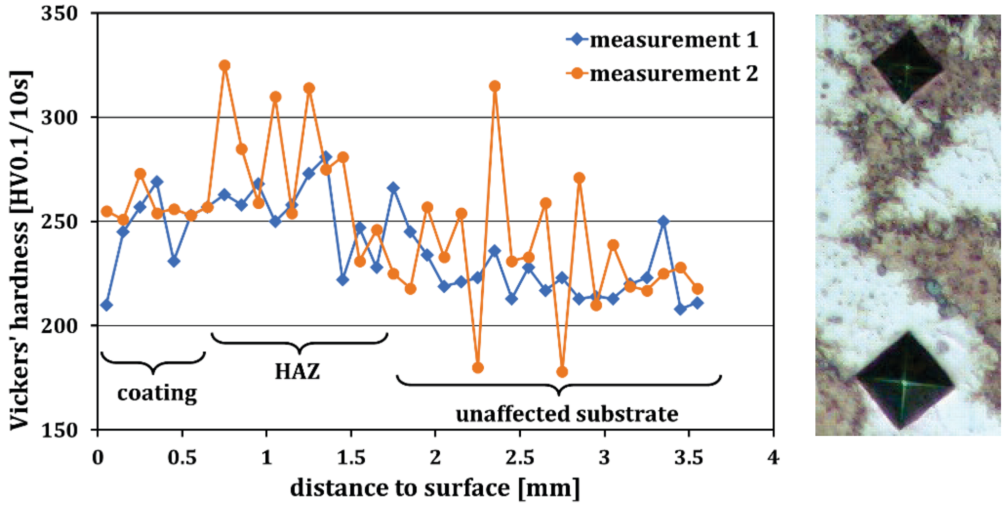

Figure 33: Hardness profile of a single layer coating starting 50 µm underneath the coating surface and an exemplary light-microscopical image showing the hardness difference between α- and β-phase.

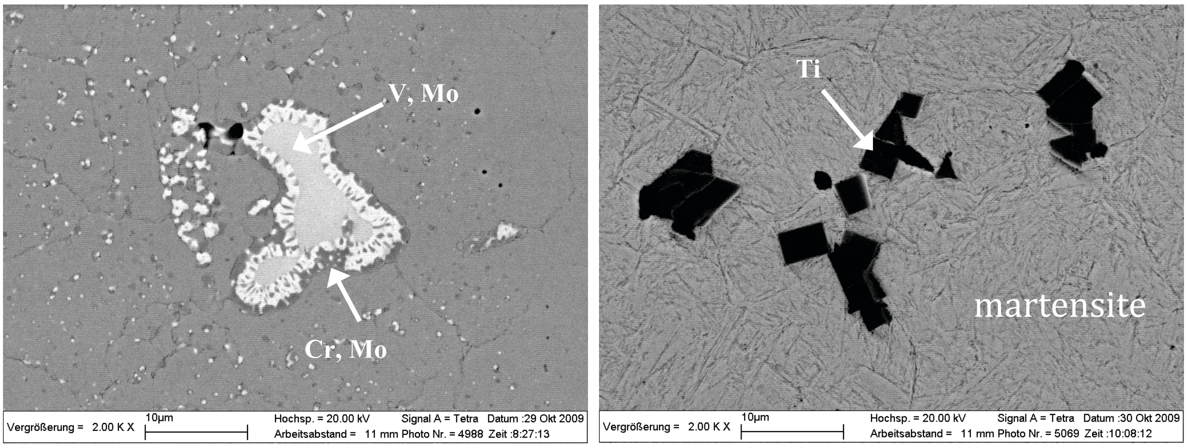

Figure 34: SEM images of the microstructure of the substrate material: inclusions/carbides containing Ti, Mo, Mn, Cr and V in a martensitic matrix.

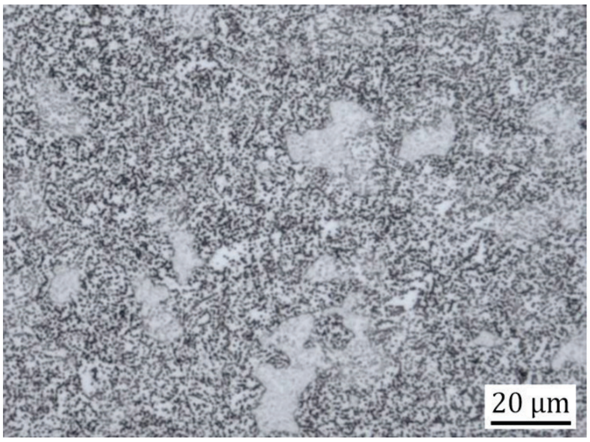

Figure 35: Microstructure of the tool steel CP4M in the soft annealed state (stud material).

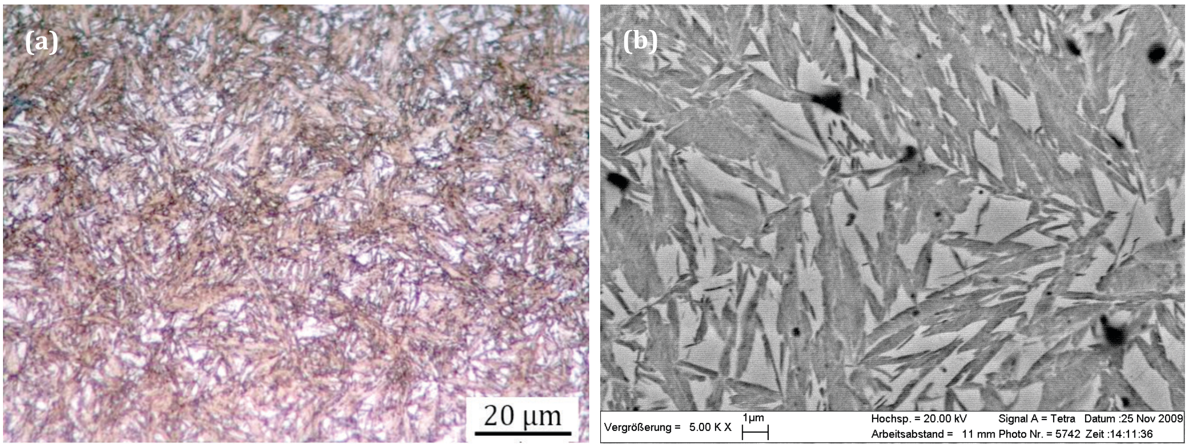

Figure 36: Homogeneous martensite in cross sections of CP4M steel FS coating observed by light microscopy (a) and SEM (b).

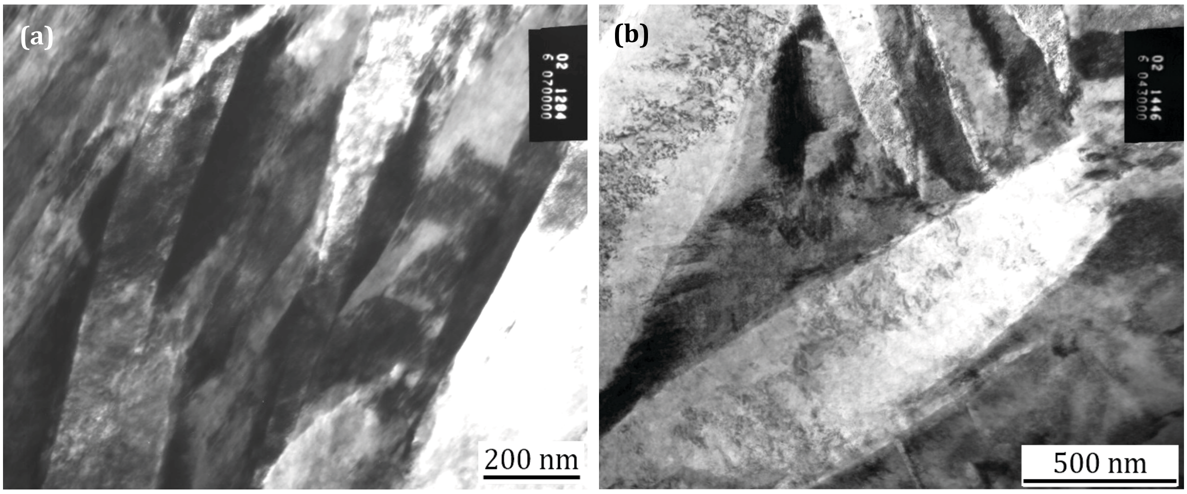

Figure 37: TEM bright field images of a steel FS coating showing plate martensite microstructure.

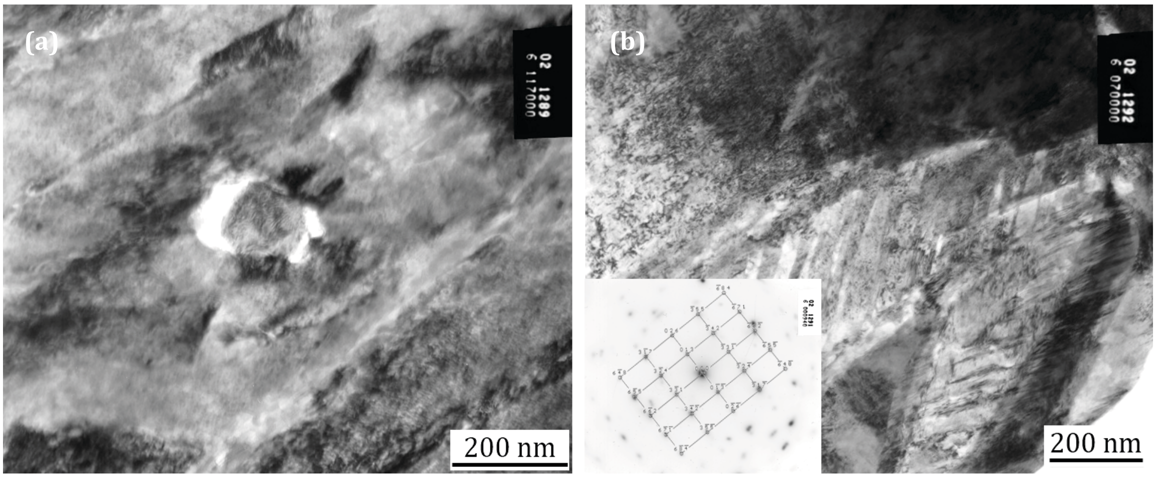

Figure 38: TEM bright field images of a steel FS coating showing (a) small precipitate and (b) diffraction pattern revealing precipitation (type $M_{23}C_6$) with a cube-cube orientation relationship with the matrix.

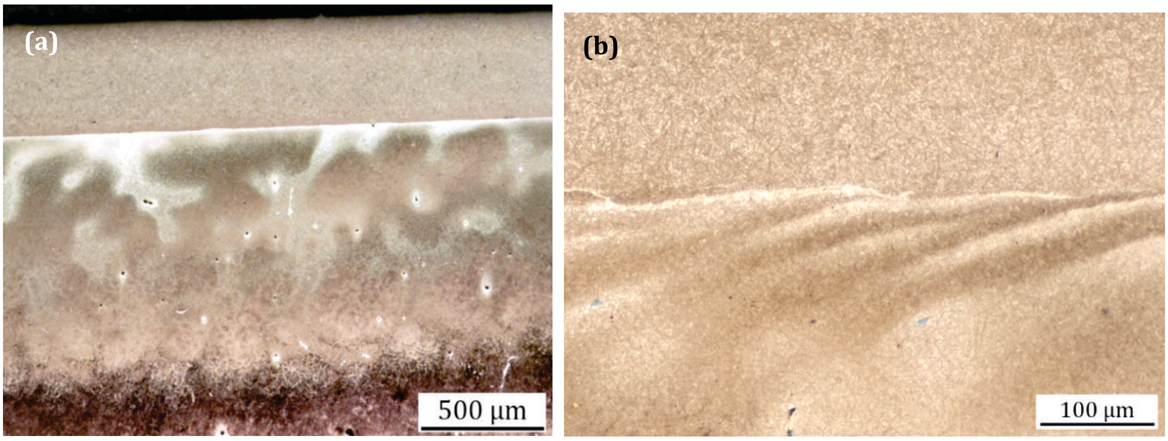

Figure 39: Light-optical image of etched cross sections of coated samples: (a) coating (top), HAZ and unaffected substrate (bottom) and (b) bonding line between the coating (top) and HAZ (bottom).

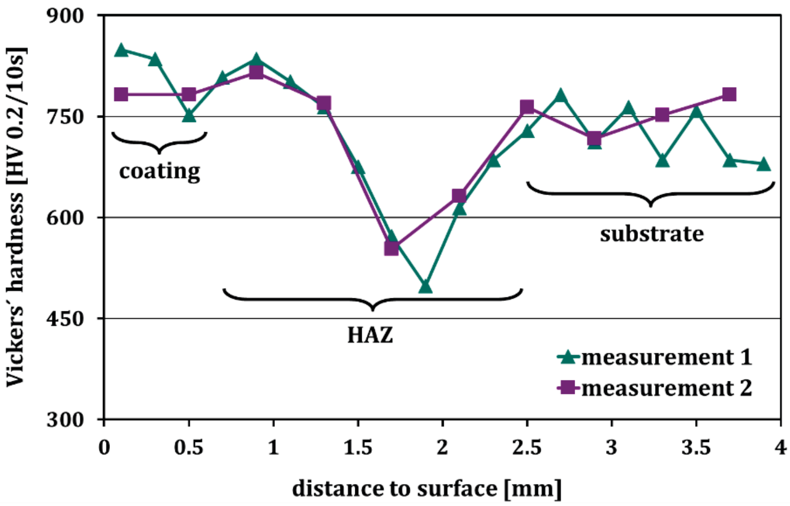

Figure 40: Hardness measurement on the cross section of a single layer coated sample.

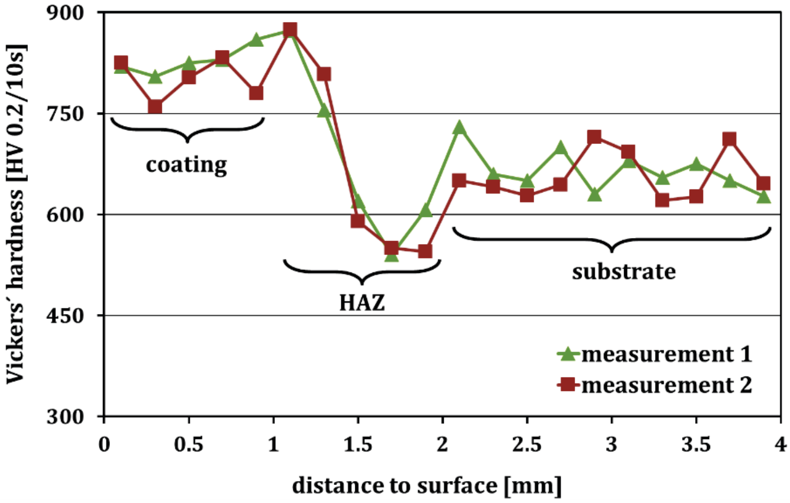

Figure 41: Hardness profile in the middle of the cross section of a double layer coated sample (offset 6 mm).

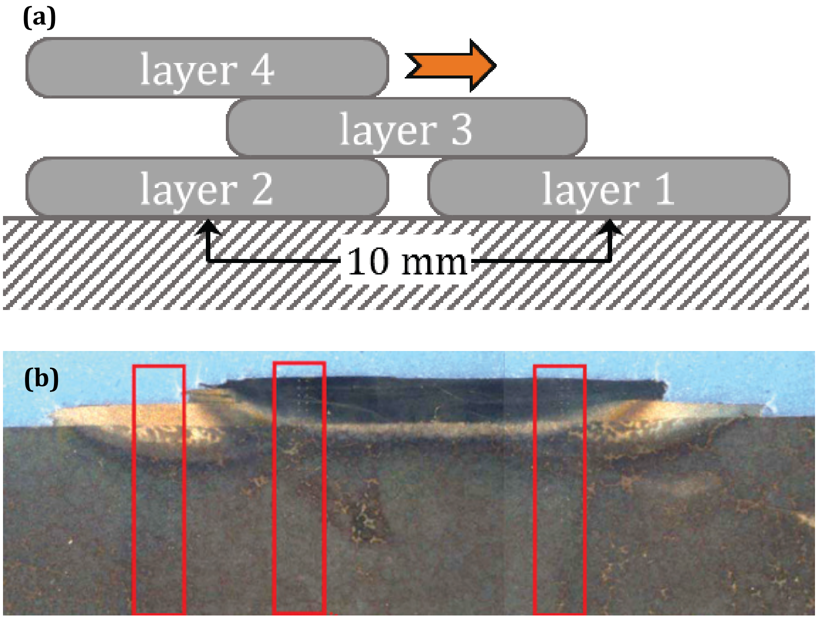

Figure 42: Schematic of the layer position of a four-layer coating (a) and macroscopic image of cross section (b). Deviation of position of layer 4 due to insufficient machine stiffness is indicated by orange arrow in (a). Red boxes in (b) mark position of hardness measurements presented in Figure 43.

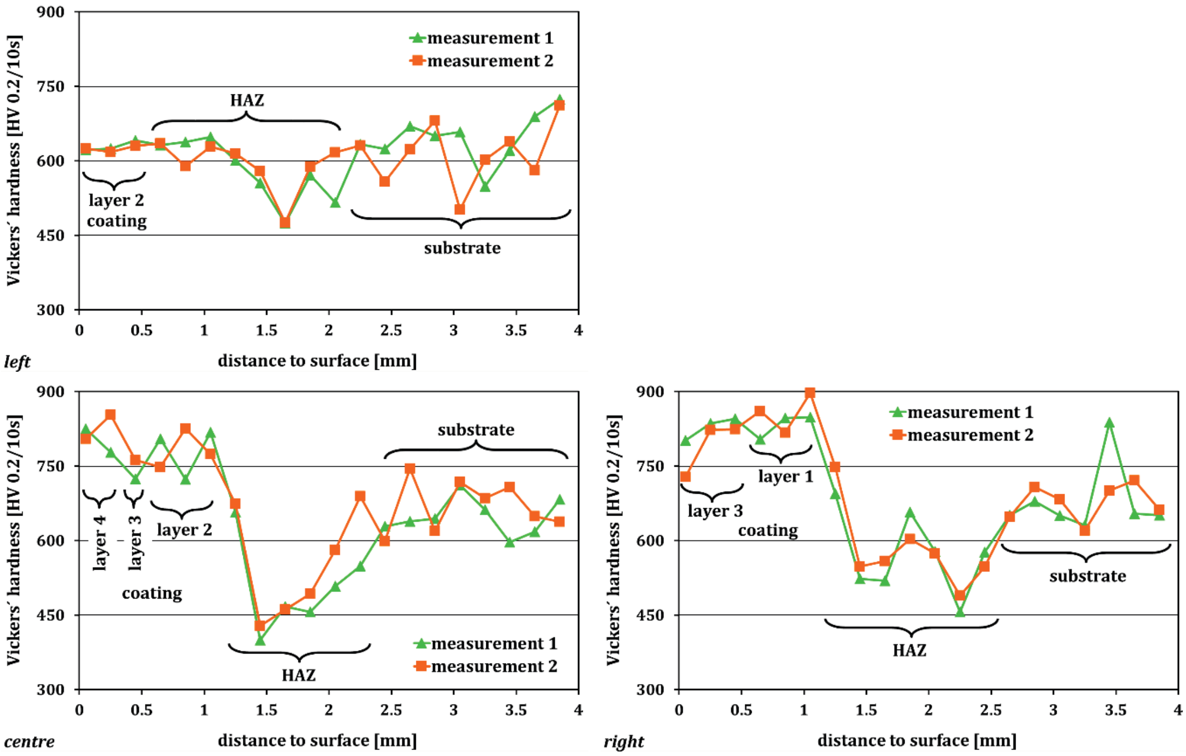

Figure 43: Hardness profiles in three positions of a four-layer coating (see Figure 42).

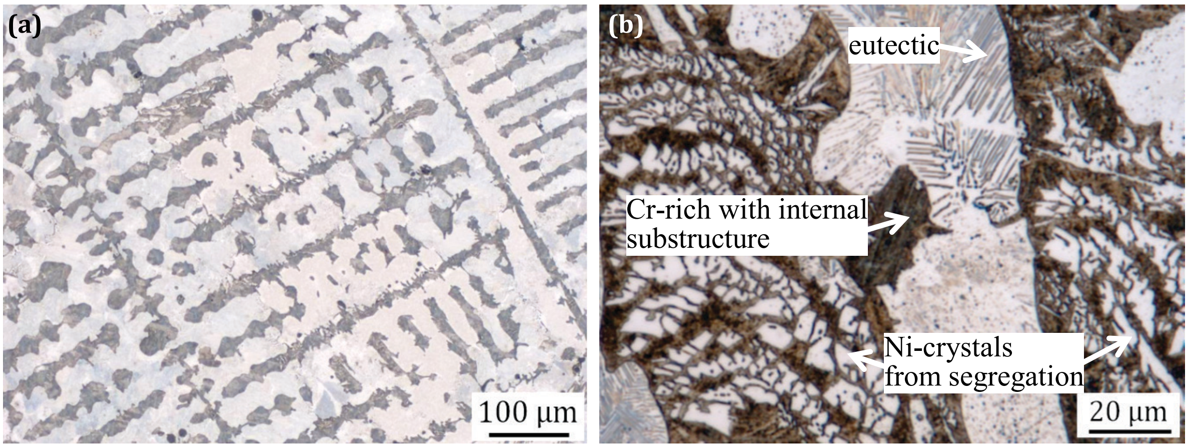

Figure 44: Microstructure of as-cast Cr60Ni40 alloy.

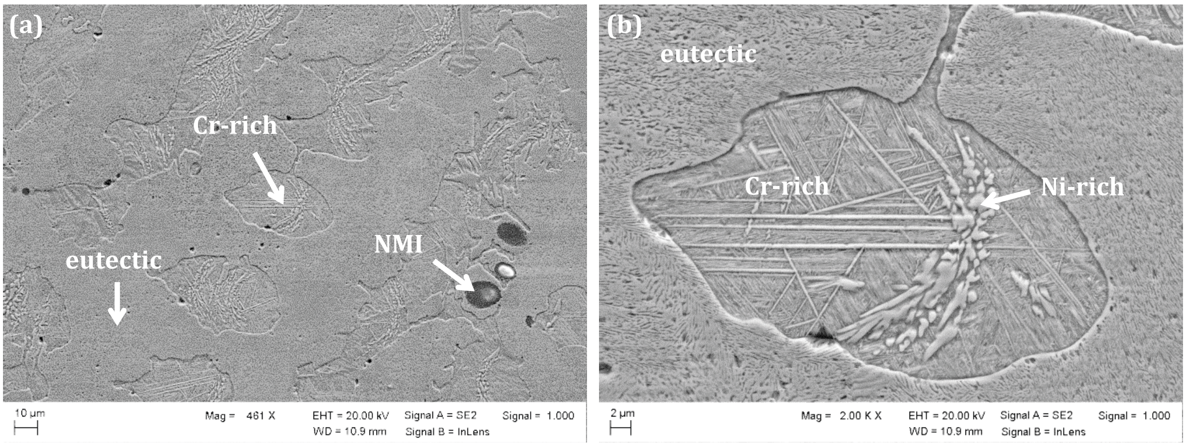

Figure 45: Microstructure of the cast and heat treated state of Cr60Ni40, overview (a) and magnification of region rich in Cr (b). Blue arrow denotes non-metallic inclusions (NMI) rich in Mn, Si and O.

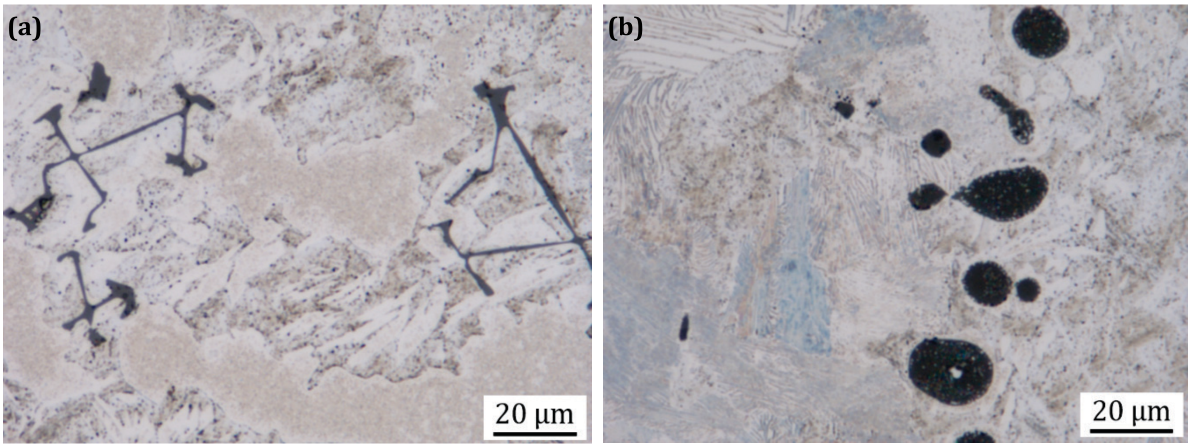

Figure 46: Types of non-metallic inclusions in cast Cr60Ni40 alloy: lamellar (a) and globular (b) shape.

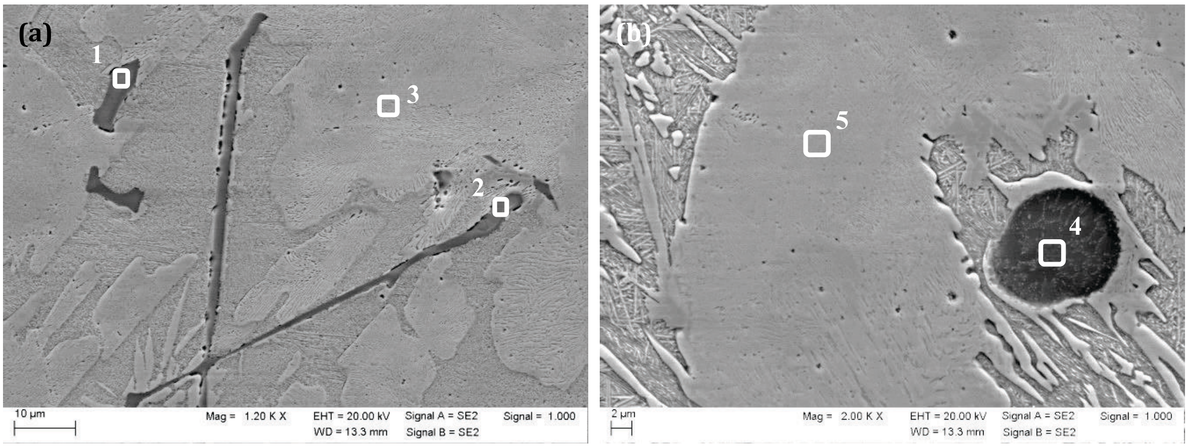

Figure 47: SEM images showing non-metallic inclusions in cast Cr60Ni40 alloy. EDS measurements show increased amounts of O, Cr and Mn in areas (1), (2) and of O, Si, S, Ti and Mn in area (4) (see Table 6 for full results).

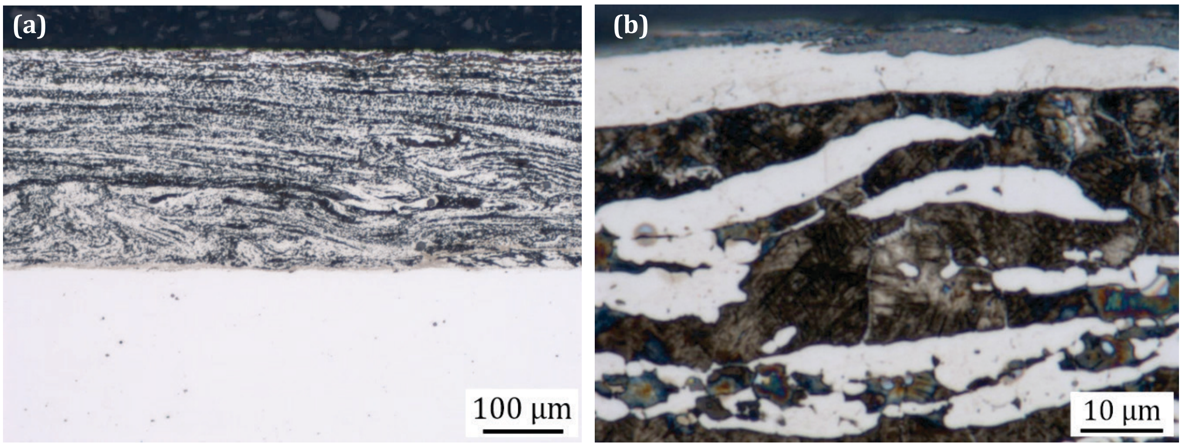

Figure 48: Cross section of single layer coating showing the complete coating thickness and the substrate (a) and a magnification of the microstructure close to the coating's surface (b).

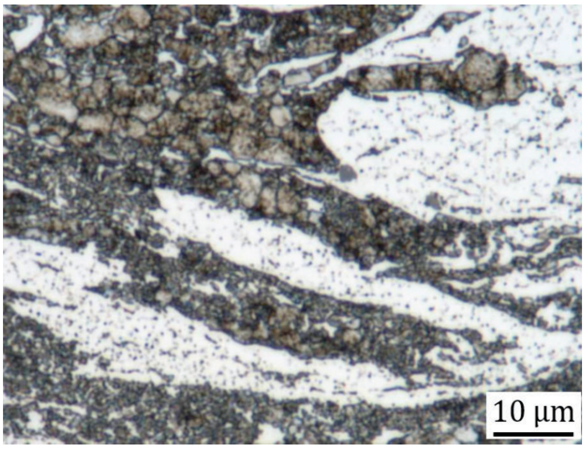

Figure 49: Cross section of a Cr60Ni40 FS coating, two-phase microstructure with small precipitates.

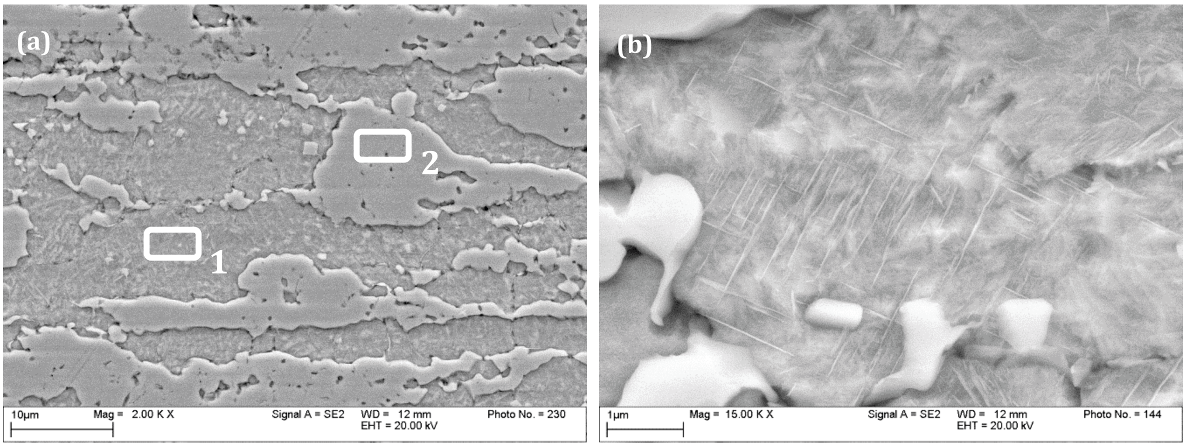

Figure 50: Cross section of a Cr60Ni40 FS coating (etched), showing the two-phase microstructure (a) and the fine needle-shaped precipitates within the more strongly etched phase (b). The average ratios of Cr:Ni determined by EDS in several measurements are 63:37 and 52:48 within the exemplary areas 1 and 2, respectively.

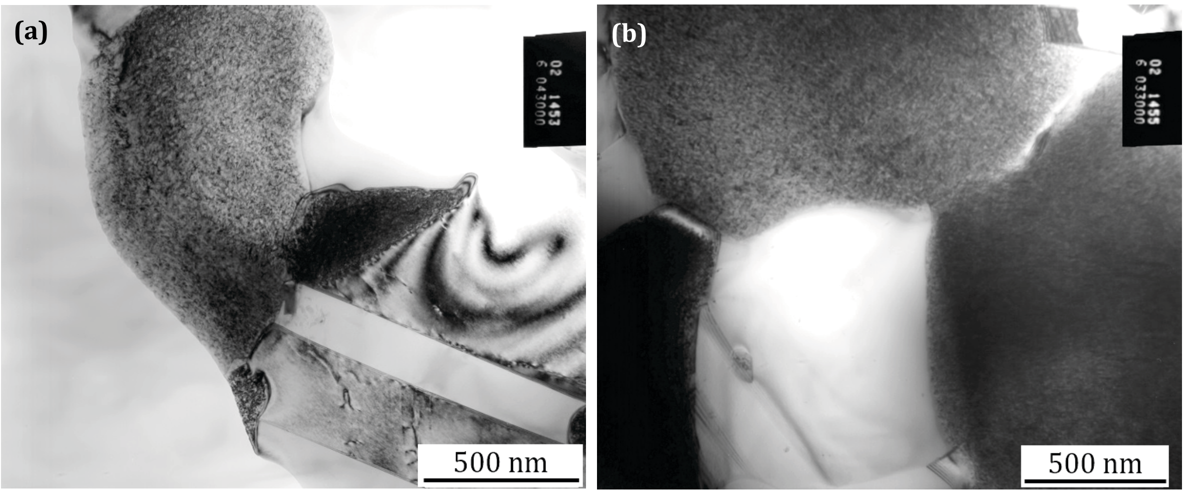

Figure 51: TEM images of Cr60Ni40 coating, showing Cr-rich phase regions with internal substructure and Ni-rich regions of bright appearance.

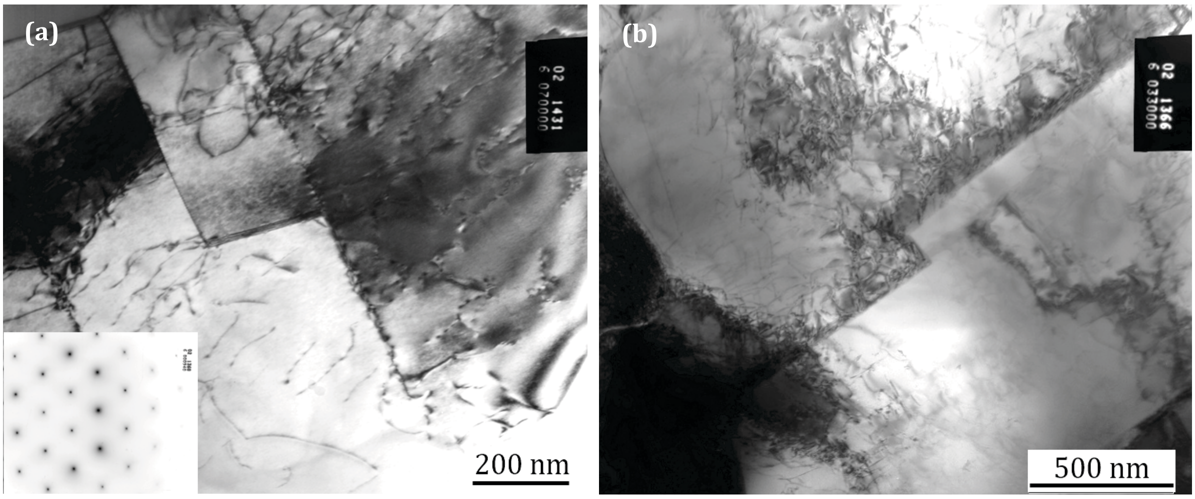

Figure 52: TEM images of Cr60Ni40 coating: “Ni-rich” solid solution with dislocation polygonisation (a) and dislocation accumulation at twin or grain boundary (b).

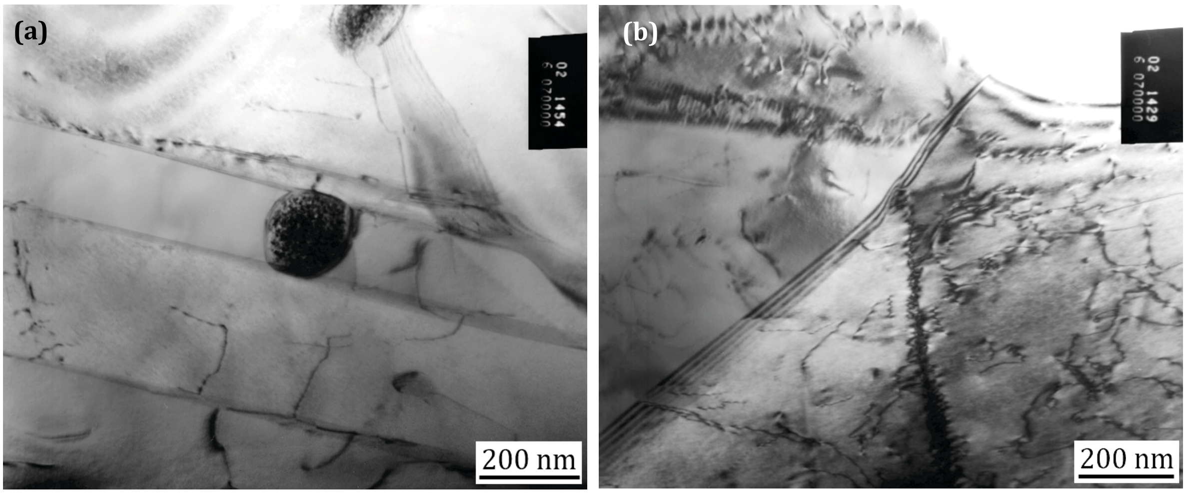

Figure 53: TEM images of Cr60Ni40 coating: supersaturated solid solution with twins and second phases (a) and dislocation arrays/polygonisation (b).

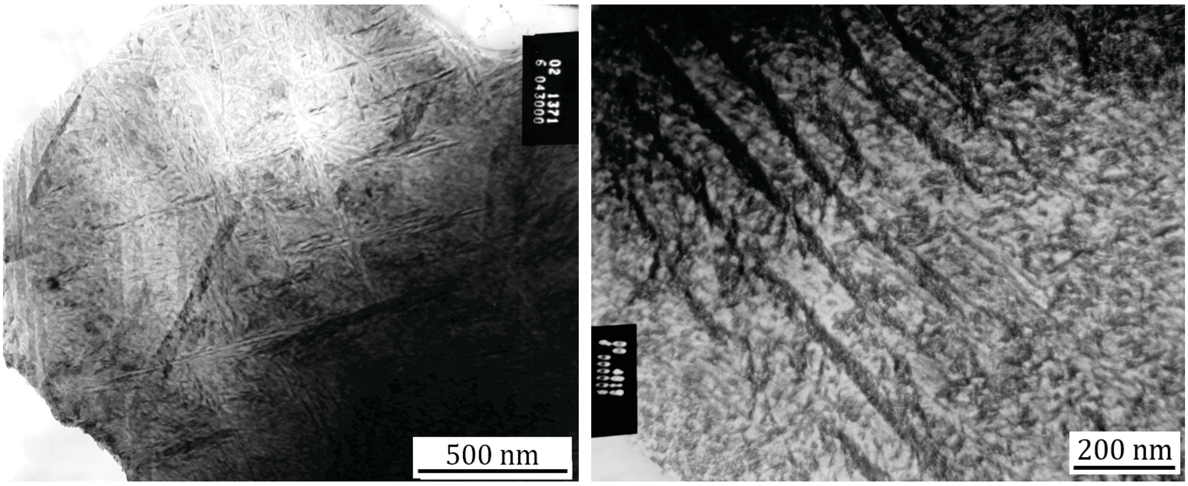

Figure 54: TEM images of Cr60Ni40 coating: Cr-rich regions with internal substructure at different magnifications.

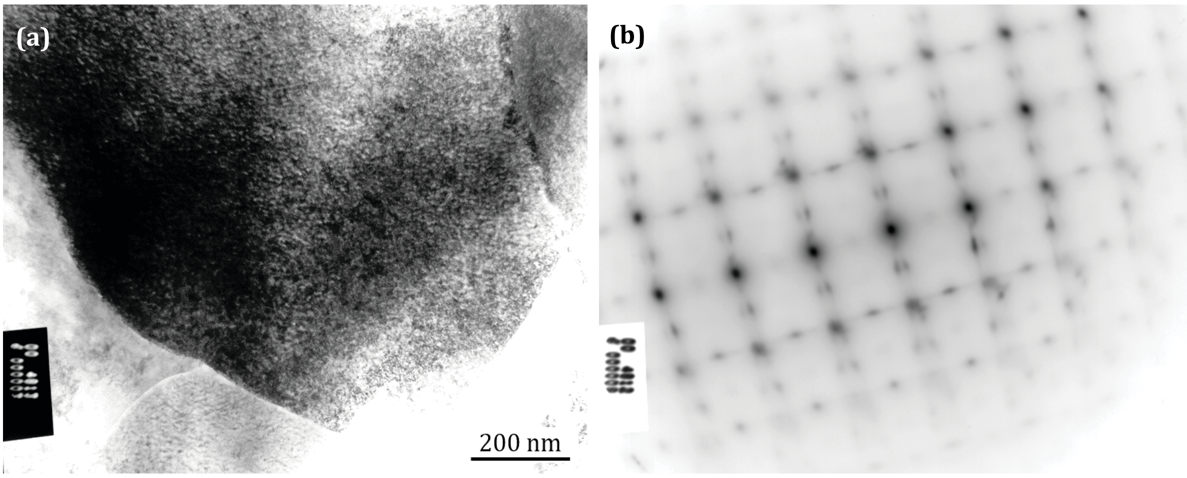

Figure 55: TEM images of Cr60Ni40 coating: Cr-rich phase in bright field image (a) and corresponding diffraction pattern (b).

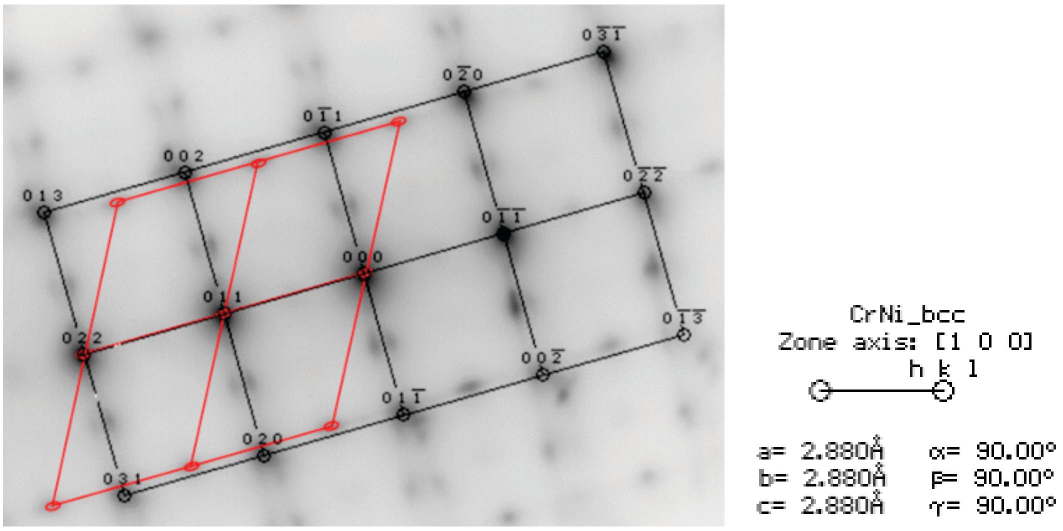

Figure 56: Analysis of the diffraction pattern in Figure 55 (b), one identified phase: bcc Chromium (black lines).

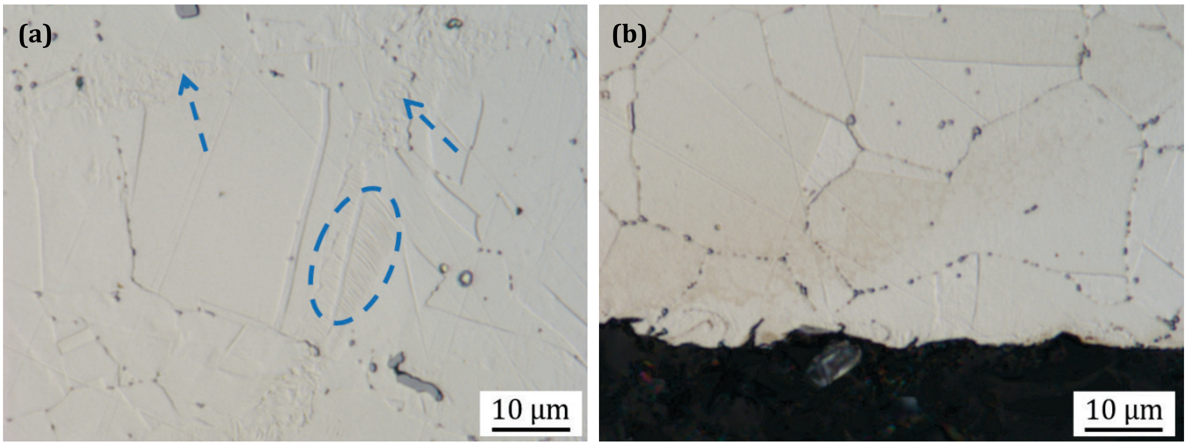

Figure 57: Light-microscopical images of the Nimonic substrate underneath a single-layer Cr60Ni40 FS coating within the HAZ close to the coating (a) and in the unaffected material at the bottom of the sheet (b).

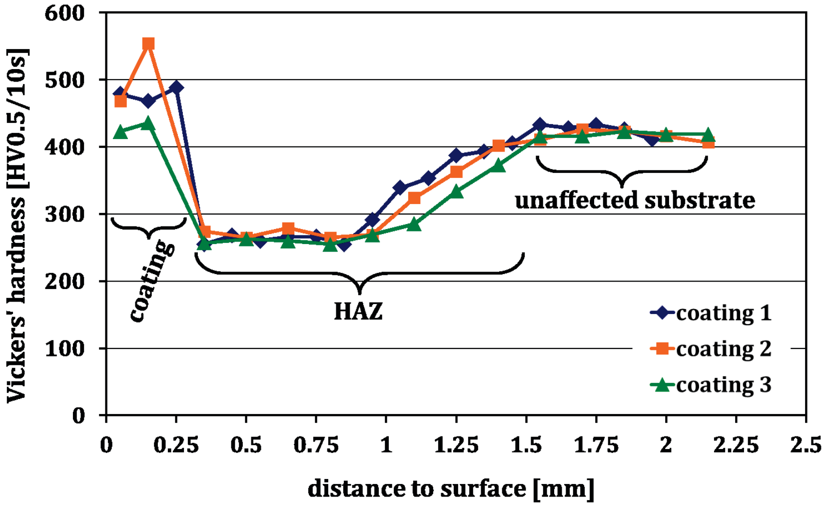

Figure 58: Hardness profiles of single layer Cr60Ni40 coatings starting 50 µm underneath the coating surface.

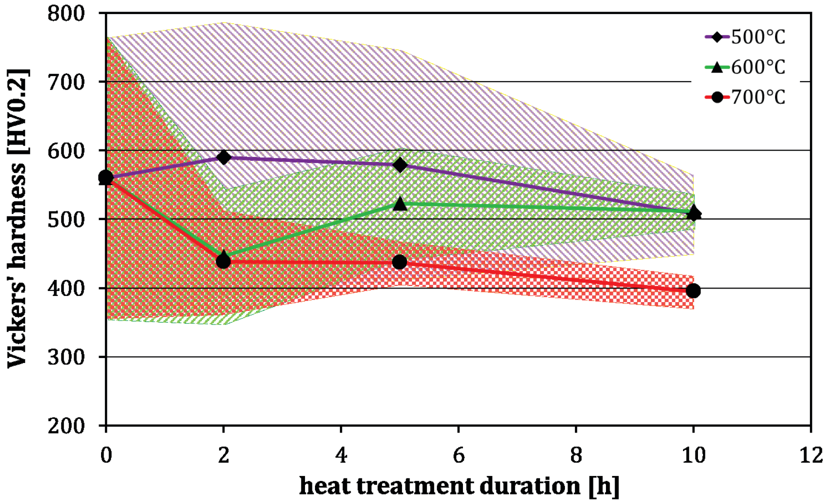

Figure 59: Evolution of hardness over time for various heat treatment temperatures and corresponding standard deviations (from 10 measurements) indicated by shaded areas.

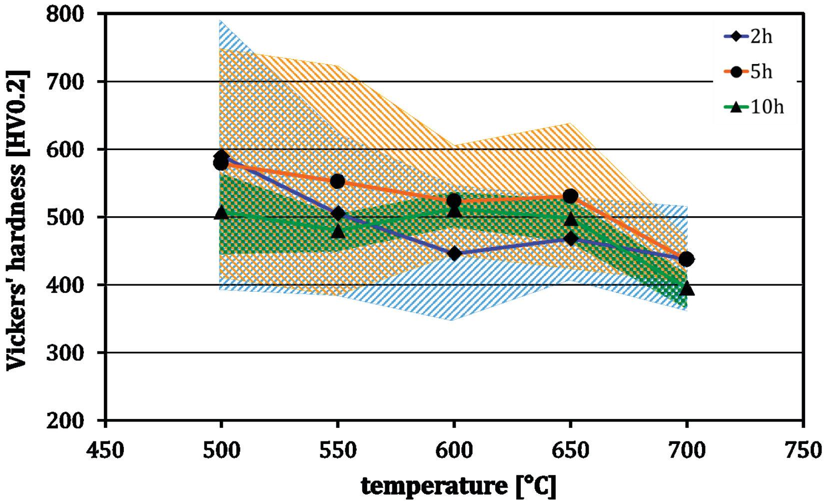

Figure 60: Evolution of hardness over temperature for different heat treatment times. The shaded areas represent the standard deviation for each temperature.

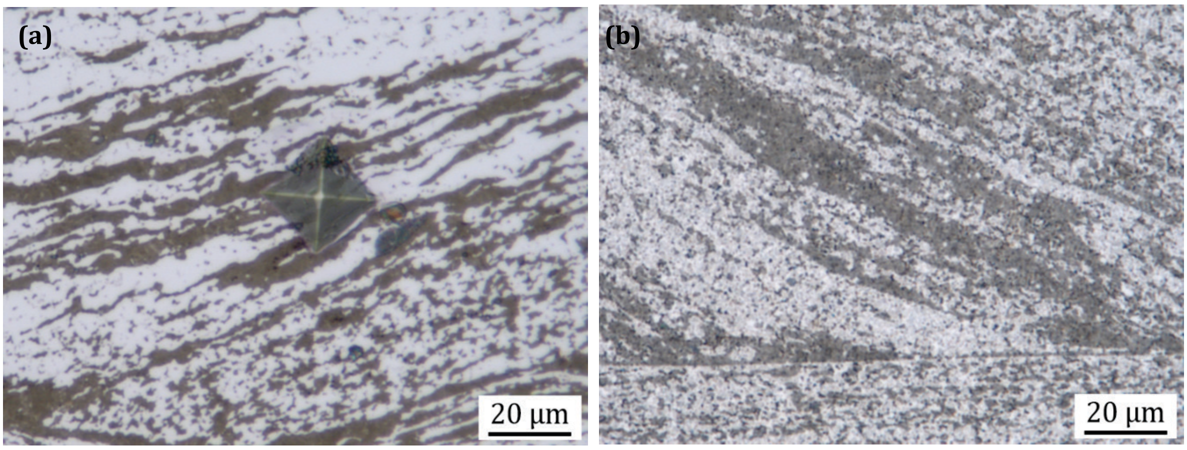

Figure 61: Microstructure of Cr60Ni40 coatings heat treated at 550°C, 2h (a) and 700°C, 2h (b).

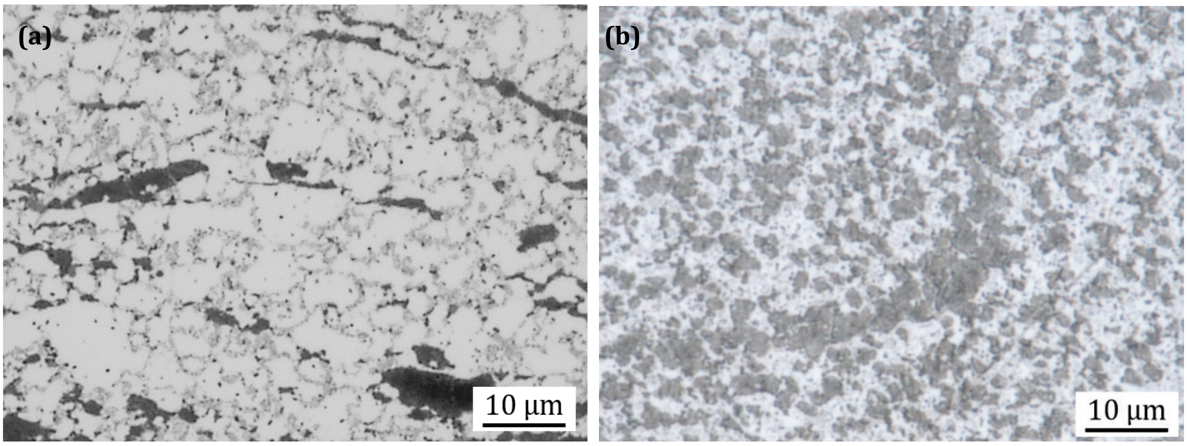

Figure 62: Microstructure of Cr60Ni40 coatings heat treated at 550°C, 10h (a) and 700°C, 10h (b).

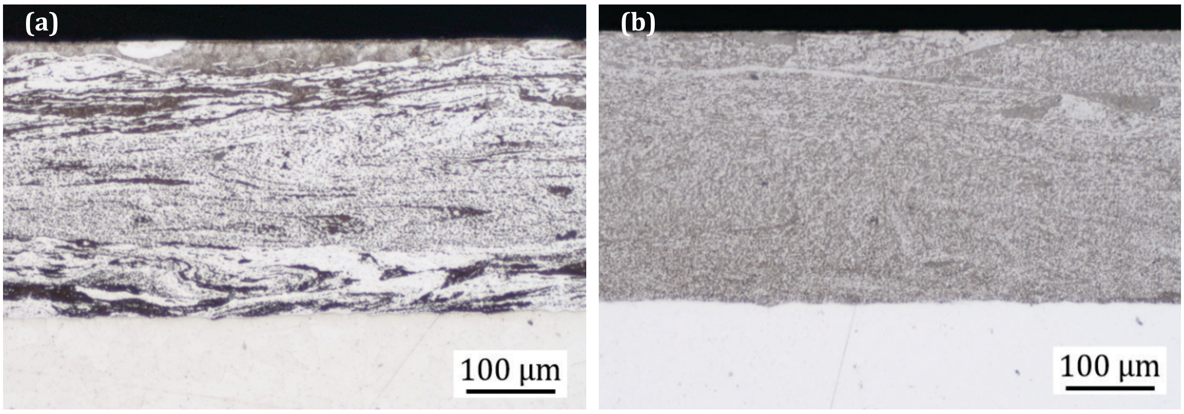

Figure 63: Microstructure of Cr60Ni40 coatings heat treated at 550°C, 10h (a) and 700°C, 10h (b).

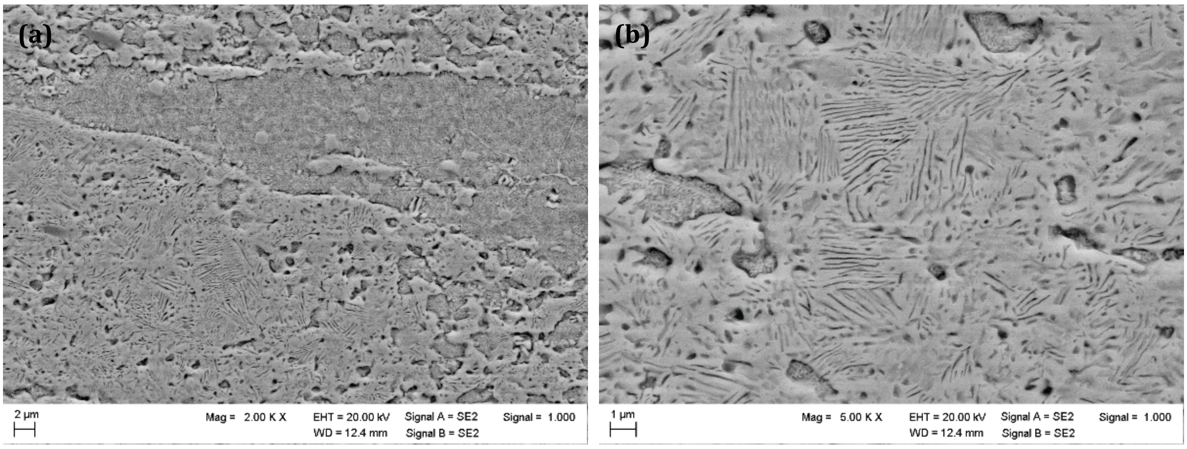

Figure 64: SEM image of microstructure of Cr60Ni40 coatings heat treated at 700°C, 10h, showing two phase regions (a) and previously supersaturated Ni-austenite with lamellar precipitates (b).

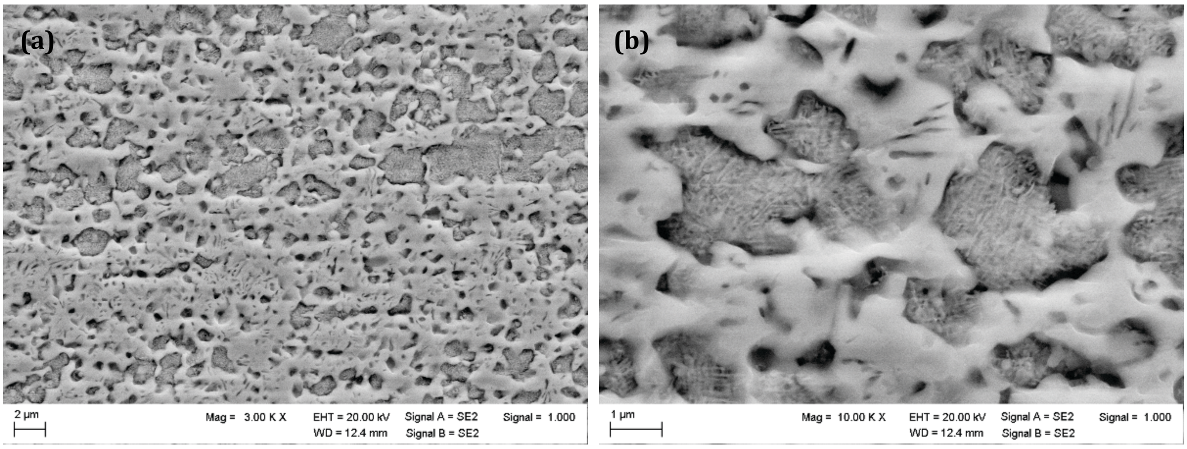

Figure 65: SEM image of microstructure of Cr60Ni40 coatings heat treated at 700°C, 10h, showing fine distribution of two phase regions (a), also at higher magnification (b).

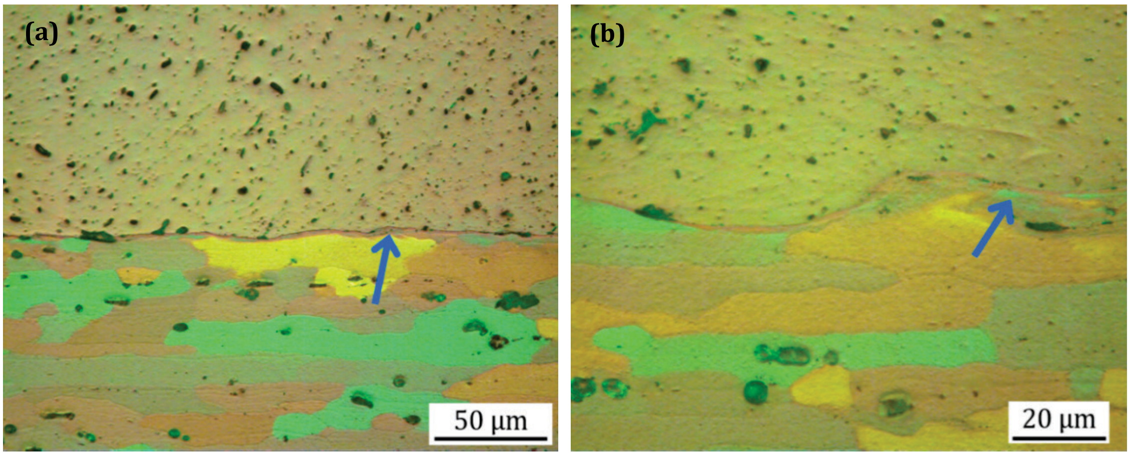

Figure 66: Light-optical images showing the microstructure close to the bonding line of a 6082 FS coating on 2024 substrate, etched and pictured using polarised light. Within the substrate a seam of unevenly coloured material is present along the bonding line (arrows), at two magnifications.

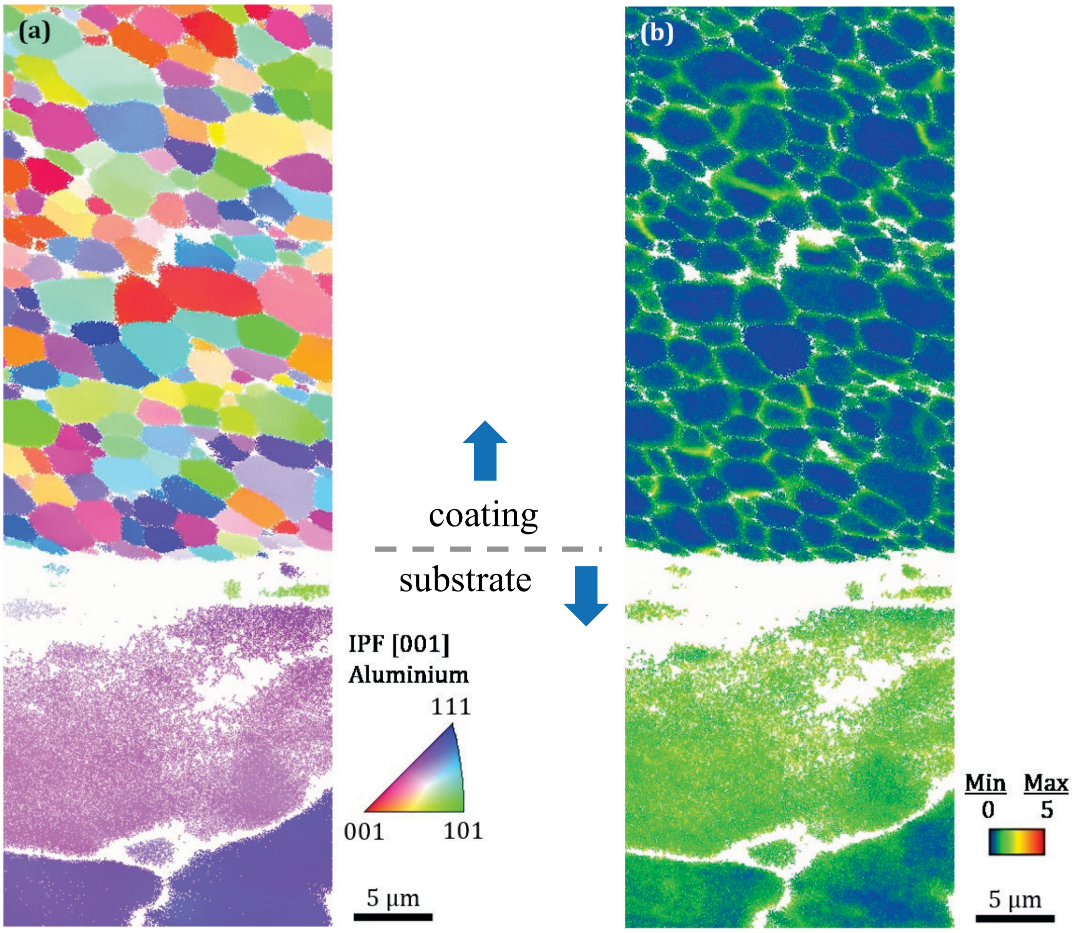

Figure 67: EBSD measurement over the bonding line of a 6082 FS coating on 2024 substrate. In the inverse pole figure (IPF) the colours represent the different orientations of the grains (a) and in the kernel average misorientation map (KAM) the degree of misorientation for each pixel relative to points in five surrounding circles of pixels is presented (b).

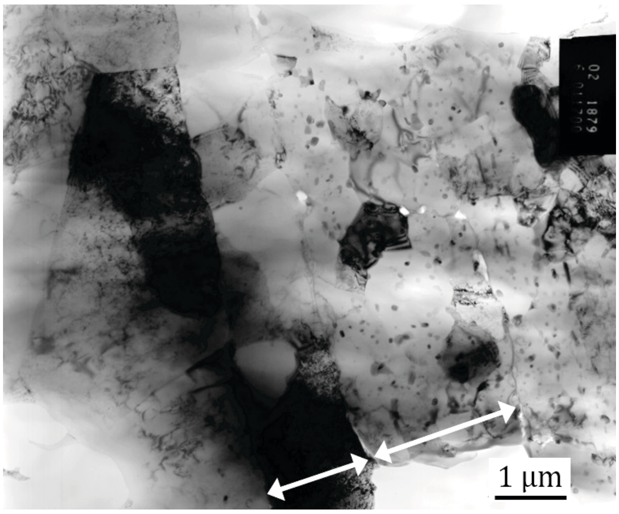

Figure 68: TEM image of the bonding line between 6082 FS coating (on the right side, containing precipitates) and 2024 substrate (on the left). The arrows indicate bands with straight, nearly parallel boundaries on both sides of the bonding line.

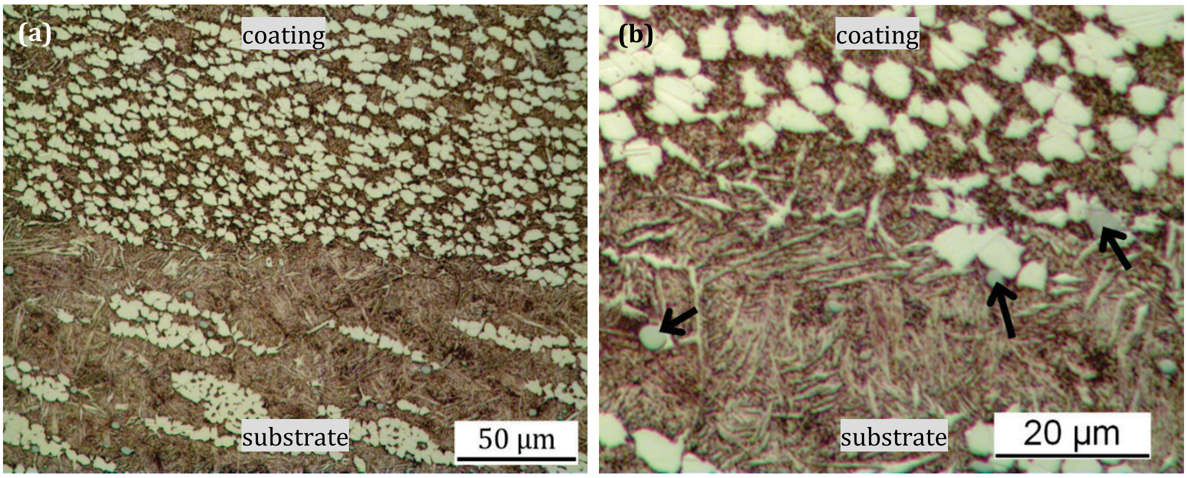

Figure 69: Cross section of a NiAl-bronze layer FS coating. The bonding line can be distinguished by a change in microstructure; arrows mark globular inclusions.

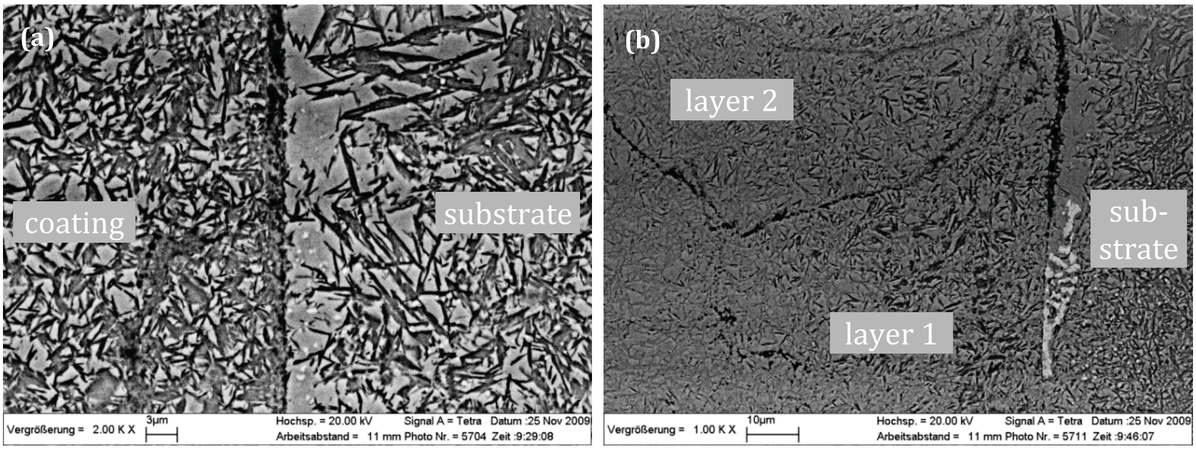

Figure 70: Cross section of steel FS coatings: bonding between single layer coating and substrate (a), and bonding between two overlapping coatings and substrate (b).

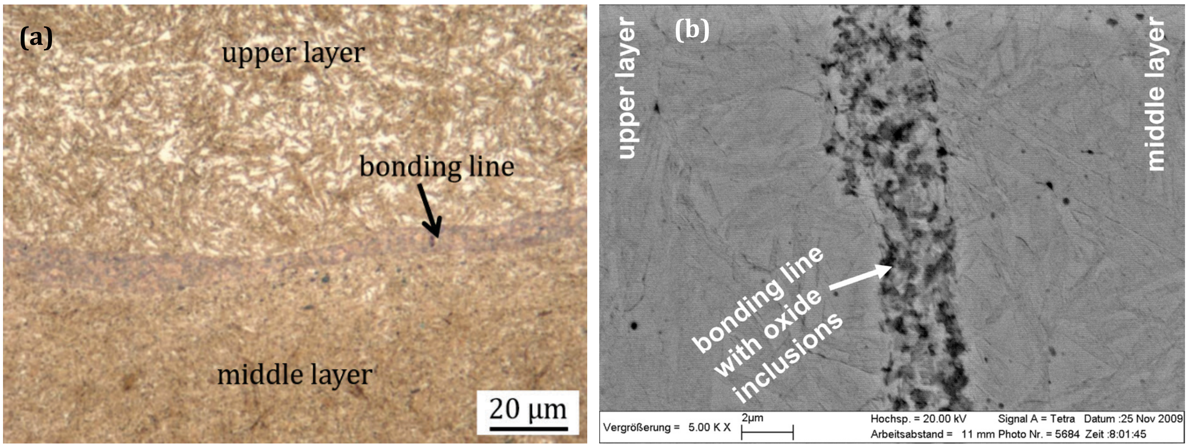

Figure 71: Cross section of a three-layer coating, showing bonding between upper and middle layer by light-microscopy (a) and SEM (b).

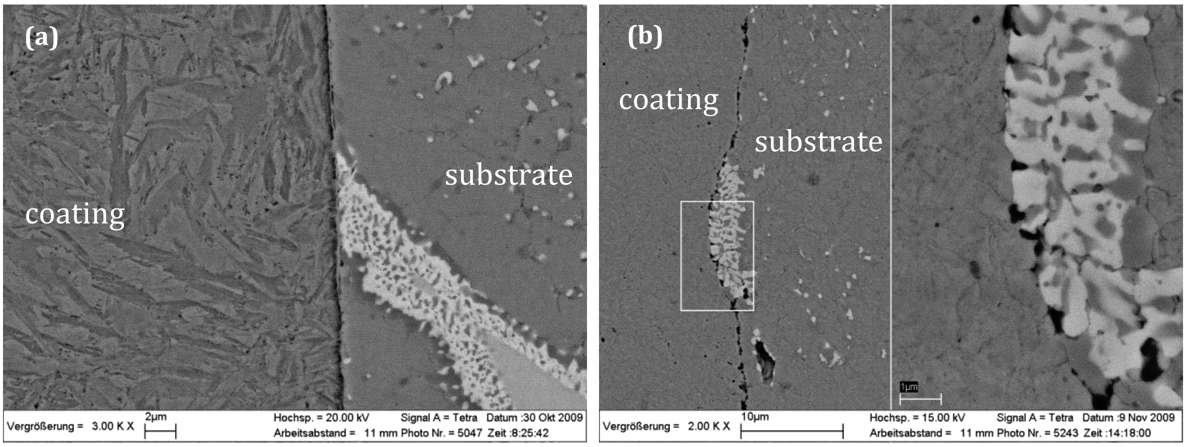

Figure 72: Cross sections of two single layer coatings, with hard phases present at the substrate surface.

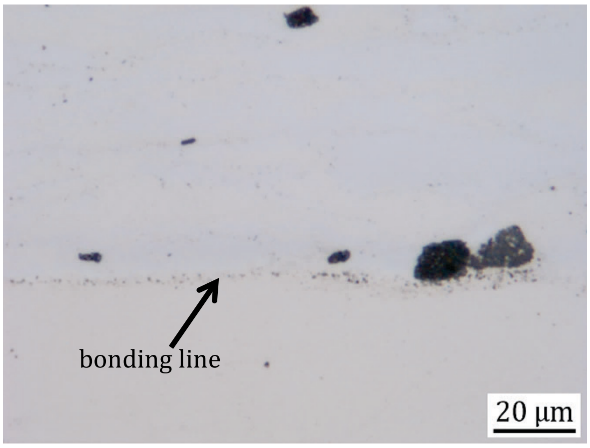

Figure 73: Bonding line between a single layer Cr60Ni40 FS coating and the substrate (polished cross section).

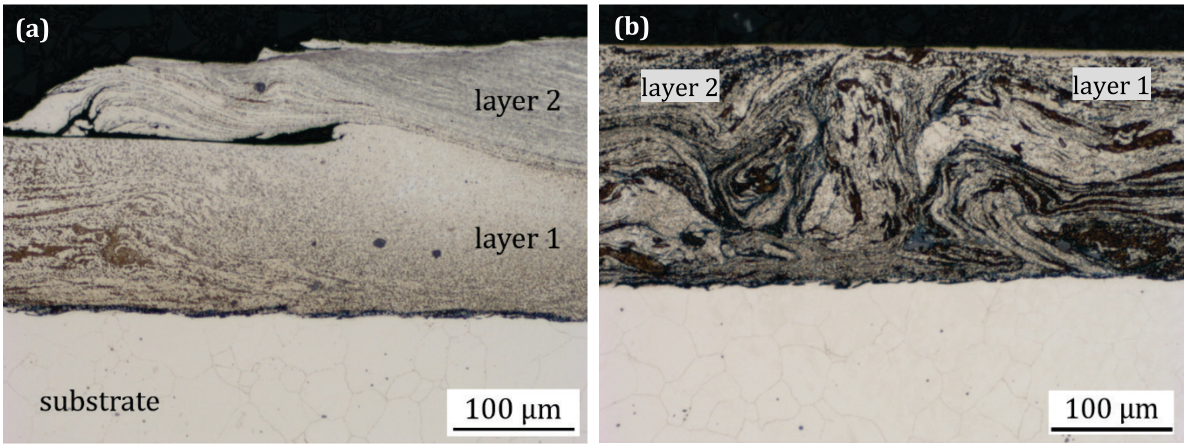

Figure 74: Bonding between overlapping layers from Cr60Ni40 alloy. Overlap realised at the advancing side (a) and at the retreating side (b).

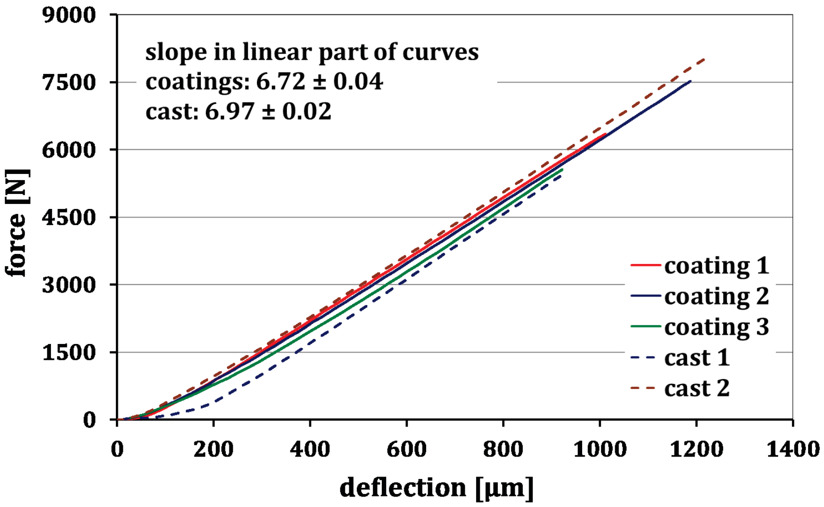

Figure 75: Applied bending force versus measured deflection in 3-point bending tests on single layer steel coatings and uncoated cast samples.

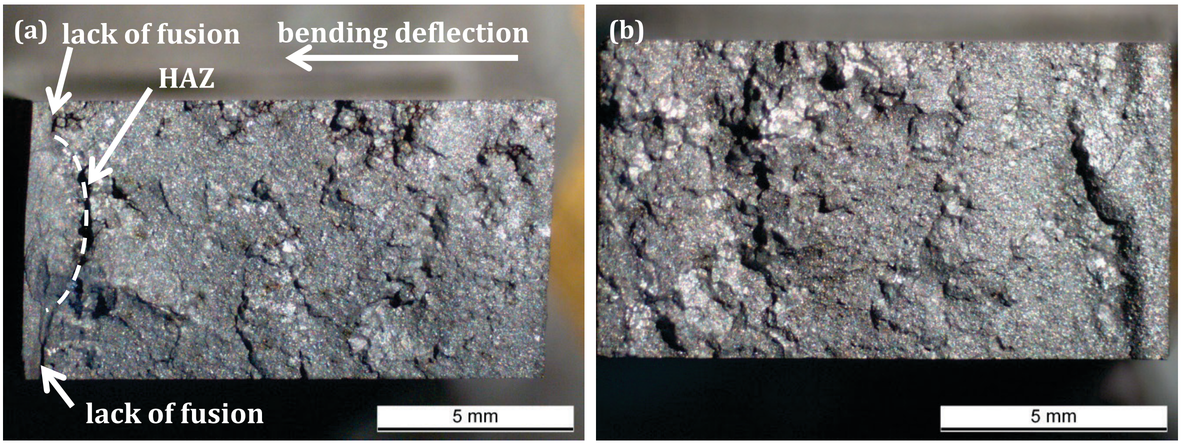

Figure 76: Fracture surface of samples after 3-point bending, showing a coated (a) and an uncoated (b) sample. The bending force was applied onto the samples' surfaces presented on the right side in the images.

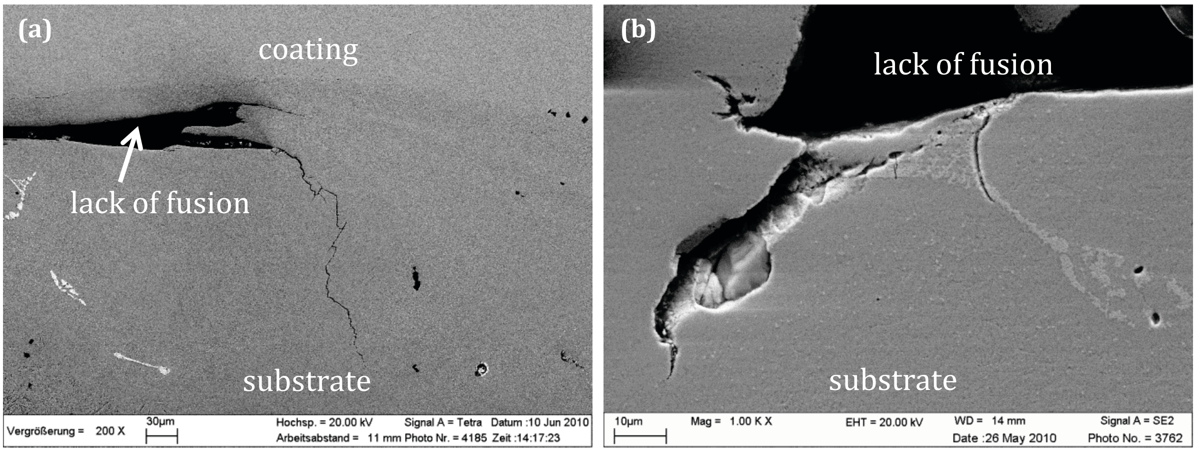

Figure 77: Defects in the substrate of steel FS coatings, located at the inner edge of the lack of fusion of a double layer (a) and a triple layer (b) coated sample.

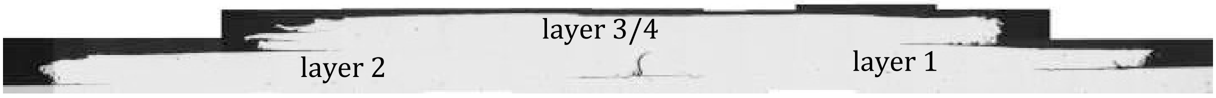

Figure 78: Light-optical micrograph of the cross section of a four layer sample (polished). A lack of bonding is visible between layers 1 and 2 and the substrate.

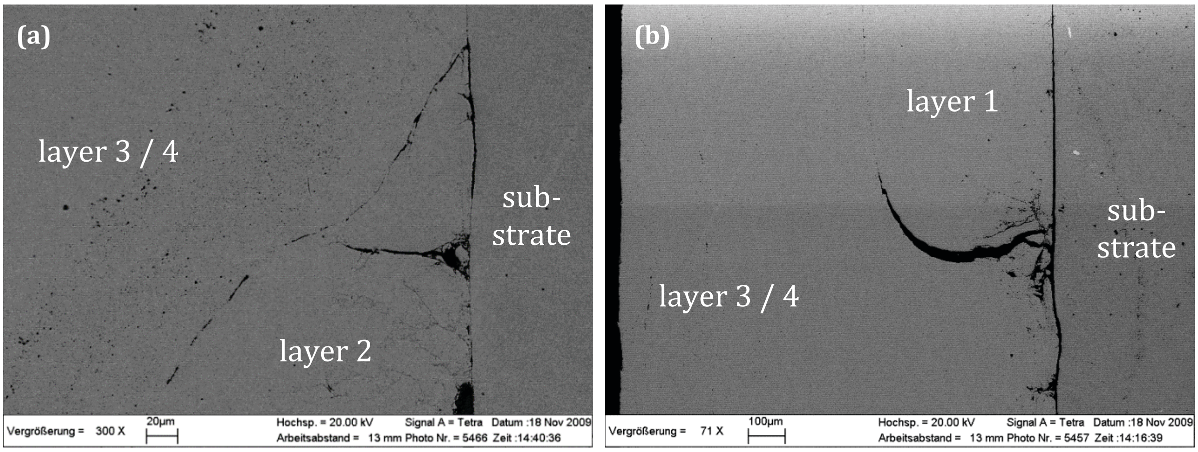

Figure 79: SEM micrographs of the sample presented also in Figure 78 (etched), showing the gap between the two lower layers, filled by material from layer 3.

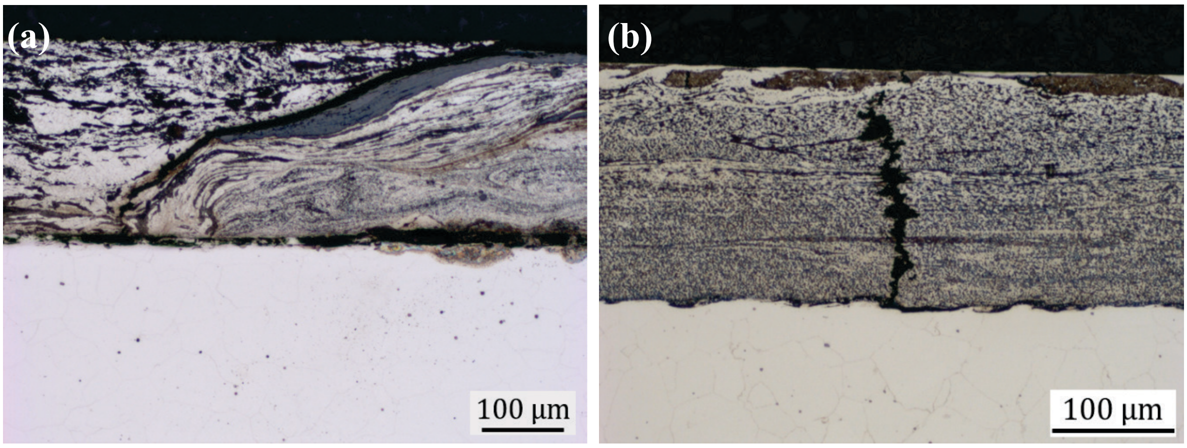

Figure 80: Defects in coatings due to inadequate process parameters: interlayer lack of fusion (a) and segmentation cracks (b).

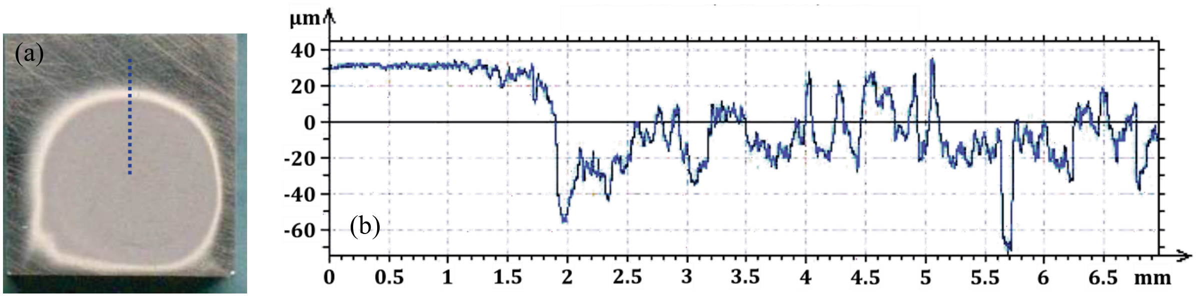

Figure 81: Wear scar on an aluminium sample after 120 min cavitation (a) and surface profile as indicated in (a) by the dashed line (b).

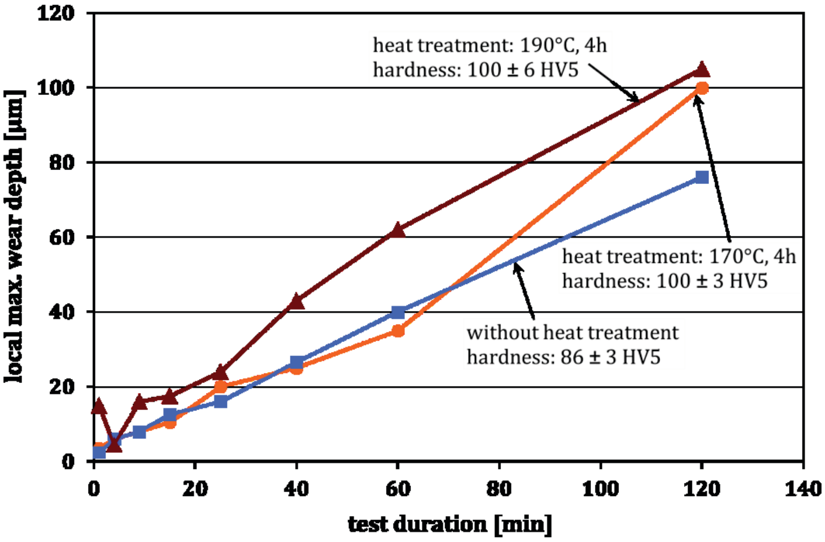

Figure 82: Localised maximum wear depth vs. test duration for 6082 FS coatings subjected to cavitation. The three curves show data for one coating in the original state, and two coatings heat treated at different temperatures.

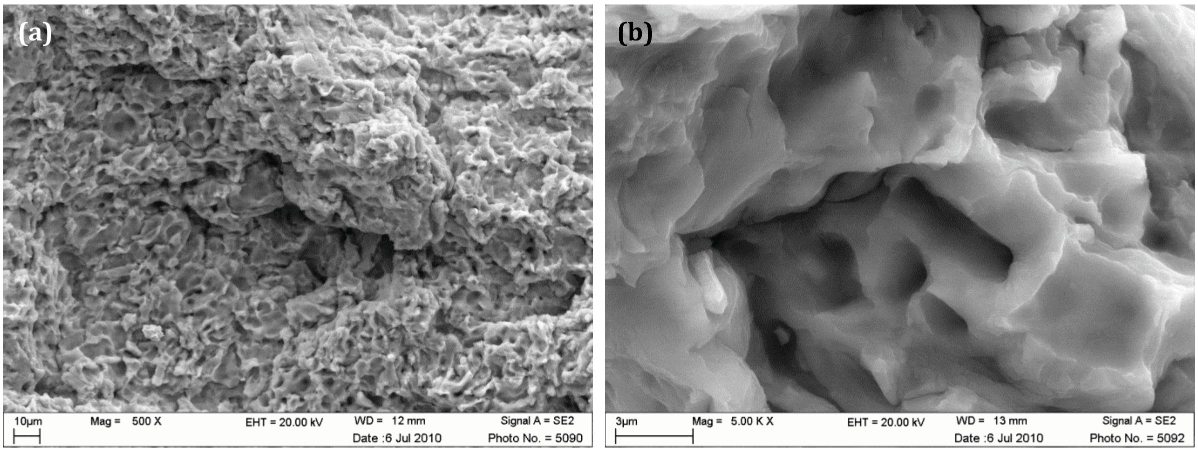

Figure 83: Worn surface of 6082 FS coating after 120 min cavitation (without heat treatment).

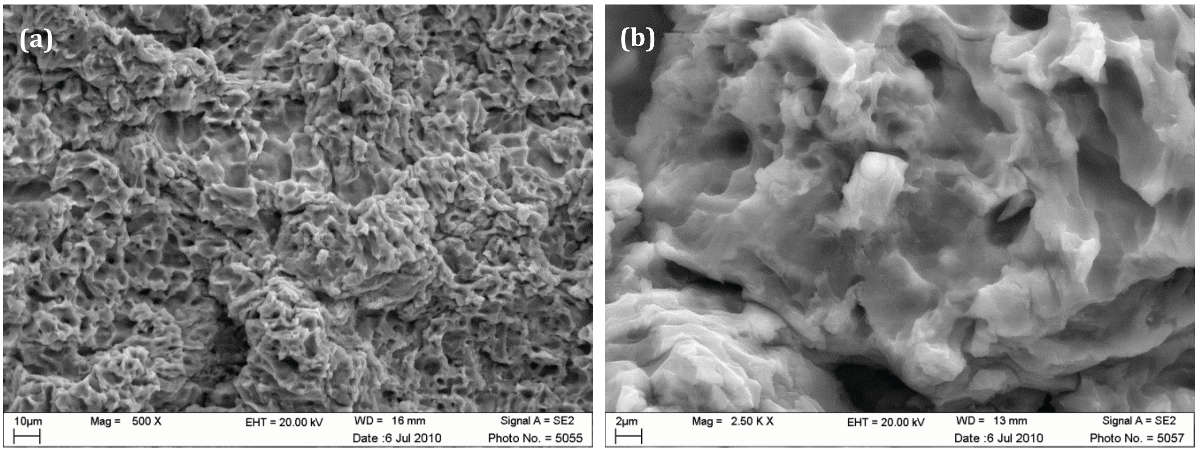

Figure 84: Worn surface of 6082 FS coating (heat treated: 170°C, 4h) after 120 min cavitation.

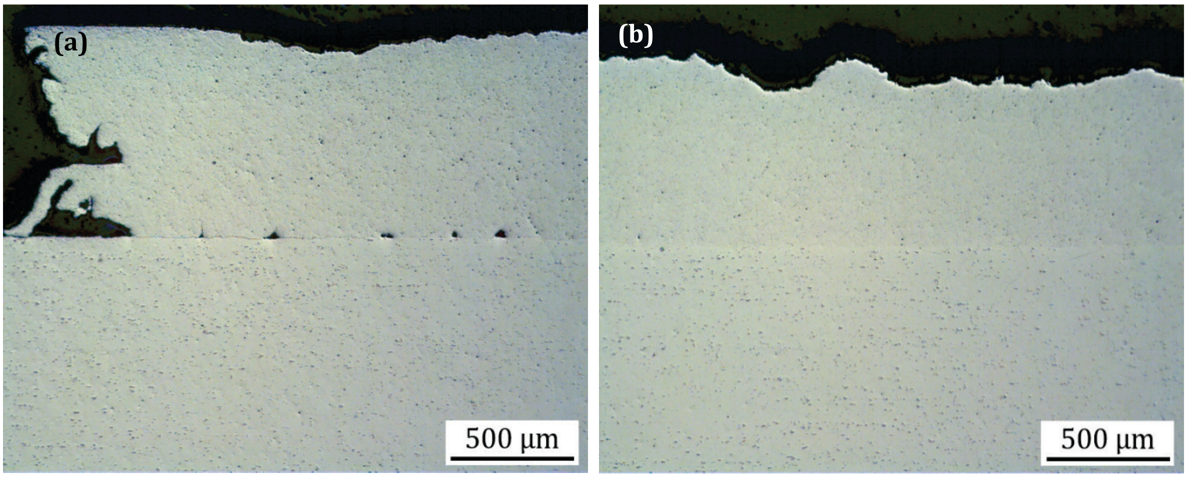

Figure 85: Cross section of heat treated 6082 FS coating after 120 min cavitation (100 ± 3 HV5).

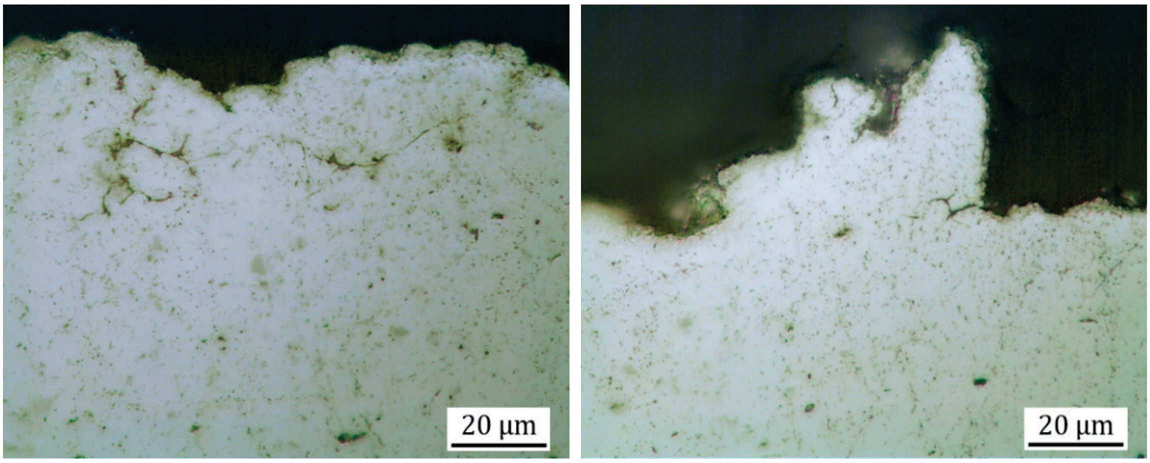

Figure 86: Cross section of heat treated 6082 FS coating after 120 min cavitation (100 ± 3 HV5).

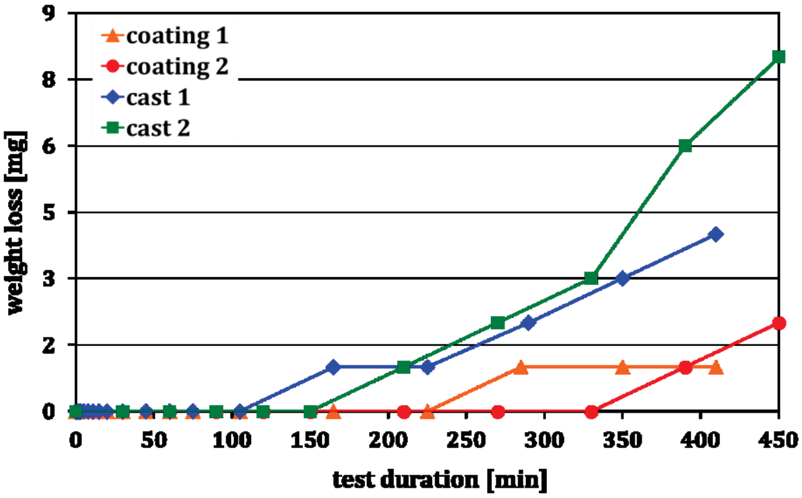

Figure 87: Weight loss vs. cavitation test duration of NiAl-bronze samples.

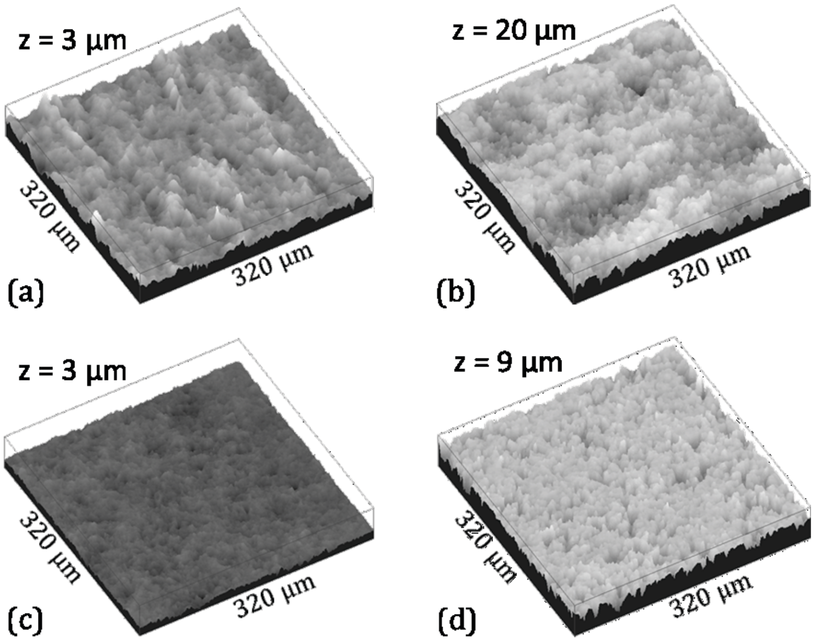

Figure 88: Surface topography of worn NiAl-bronze samples measured by confocal microscopy. Substrate: (a) 105 min, (c) 410 min; FS Coating: (b) 105 min, (d) 410 min.

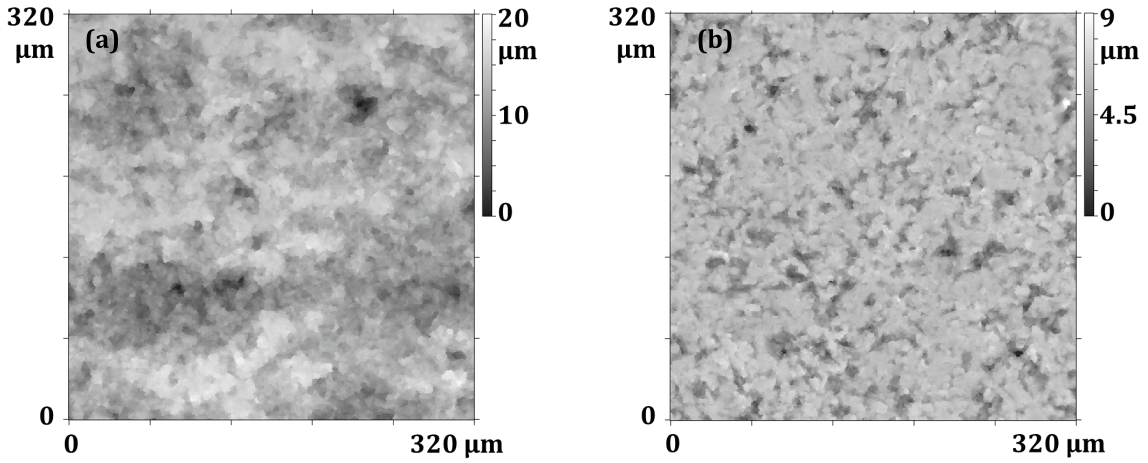

Figure 89: 2D view of surface topography of worn NiAl-bronze samples after 410 min cavitation duration: substrate (a) and FS coating (b).

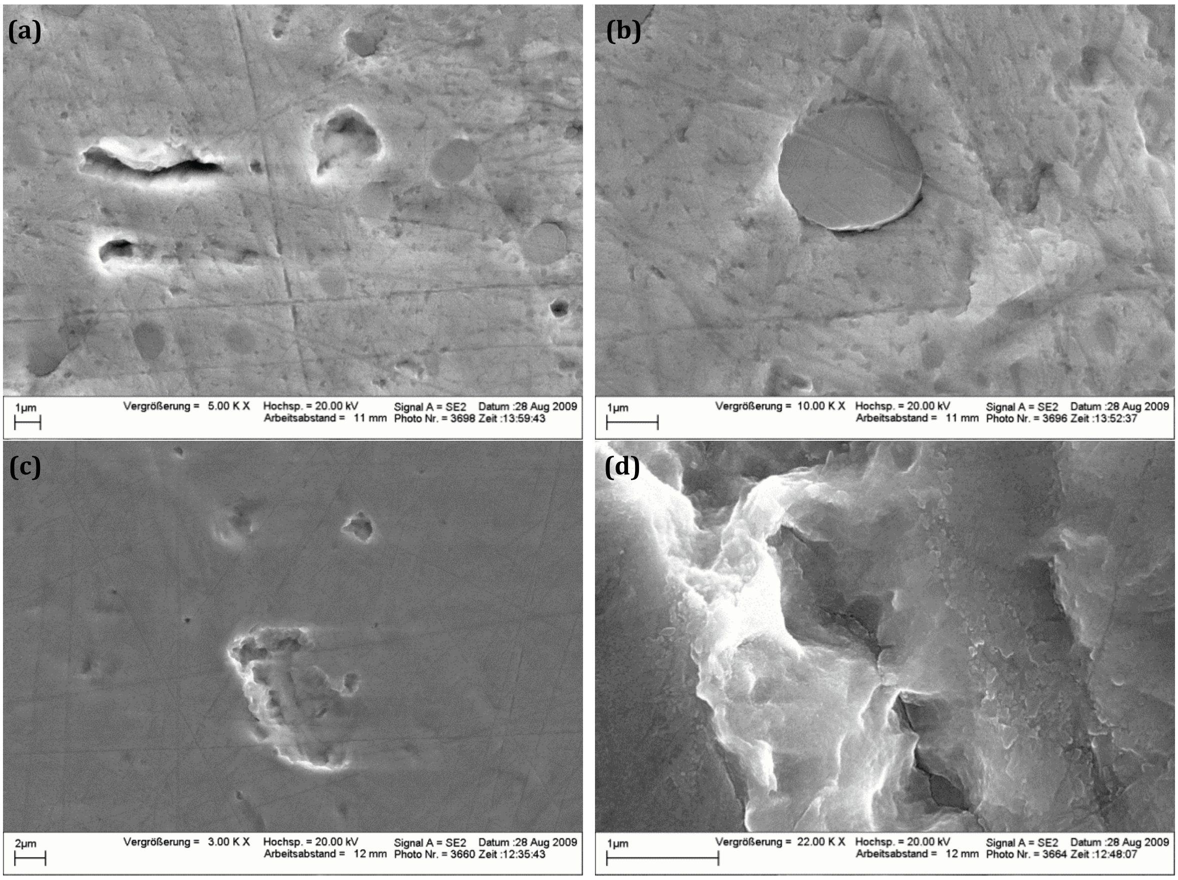

Figure 90: Worn surfaces on NiAl-bronze after 60min cavitation test. (a), (b): substrate; (c), (d): coating.

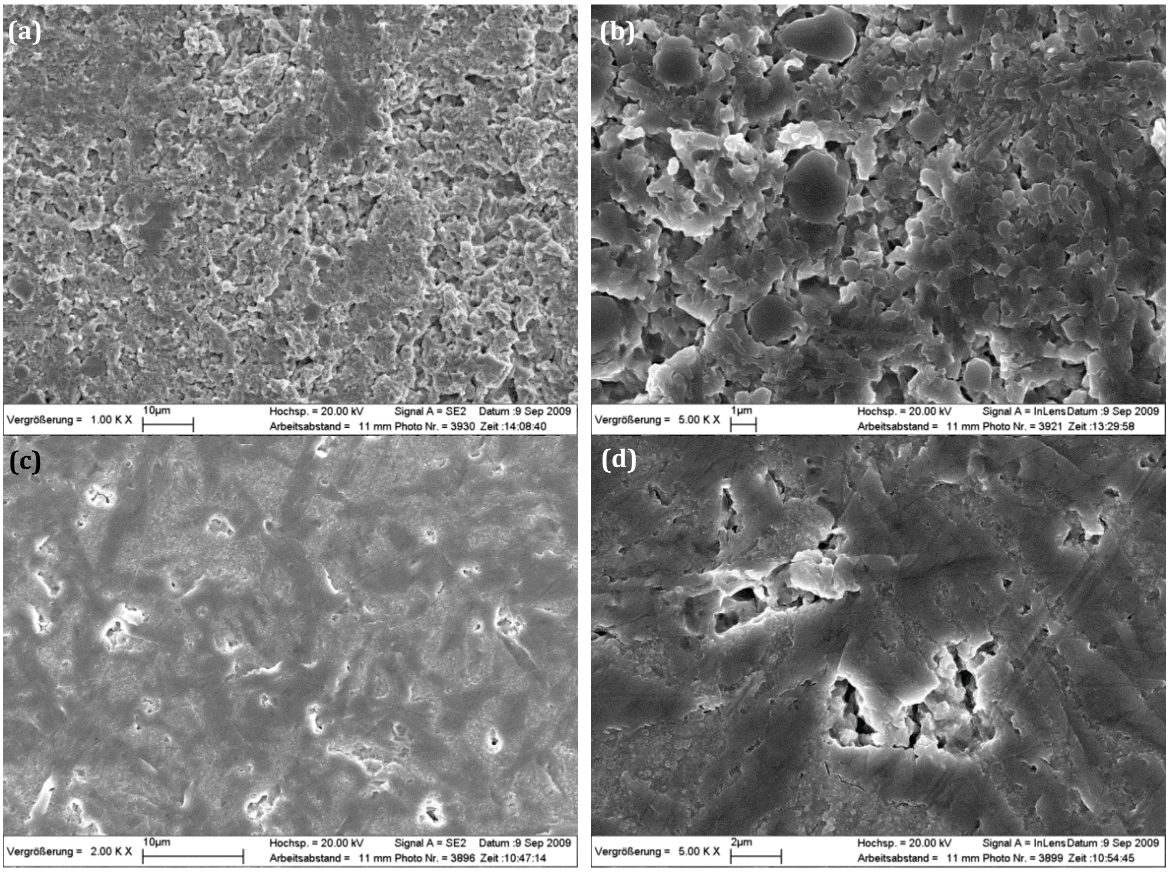

Figure 91: Worn surfaces on NiAl-bronze after 180min cavitation test. (a), (b): substrate; (c), (d): coating.

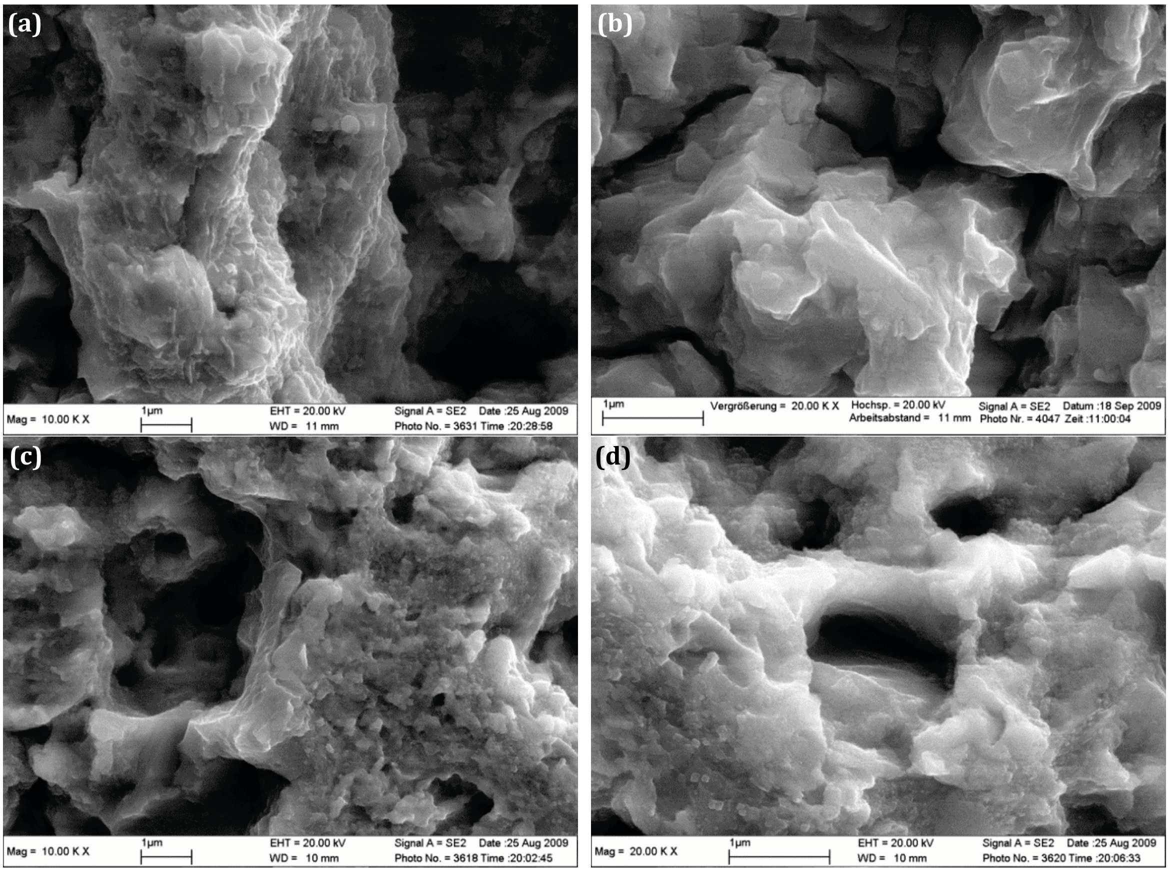

Figure 92: Worn surfaces on NiAl-bronze after 410min cavitation test. (a), (b): substrate; (c), (d): coating.

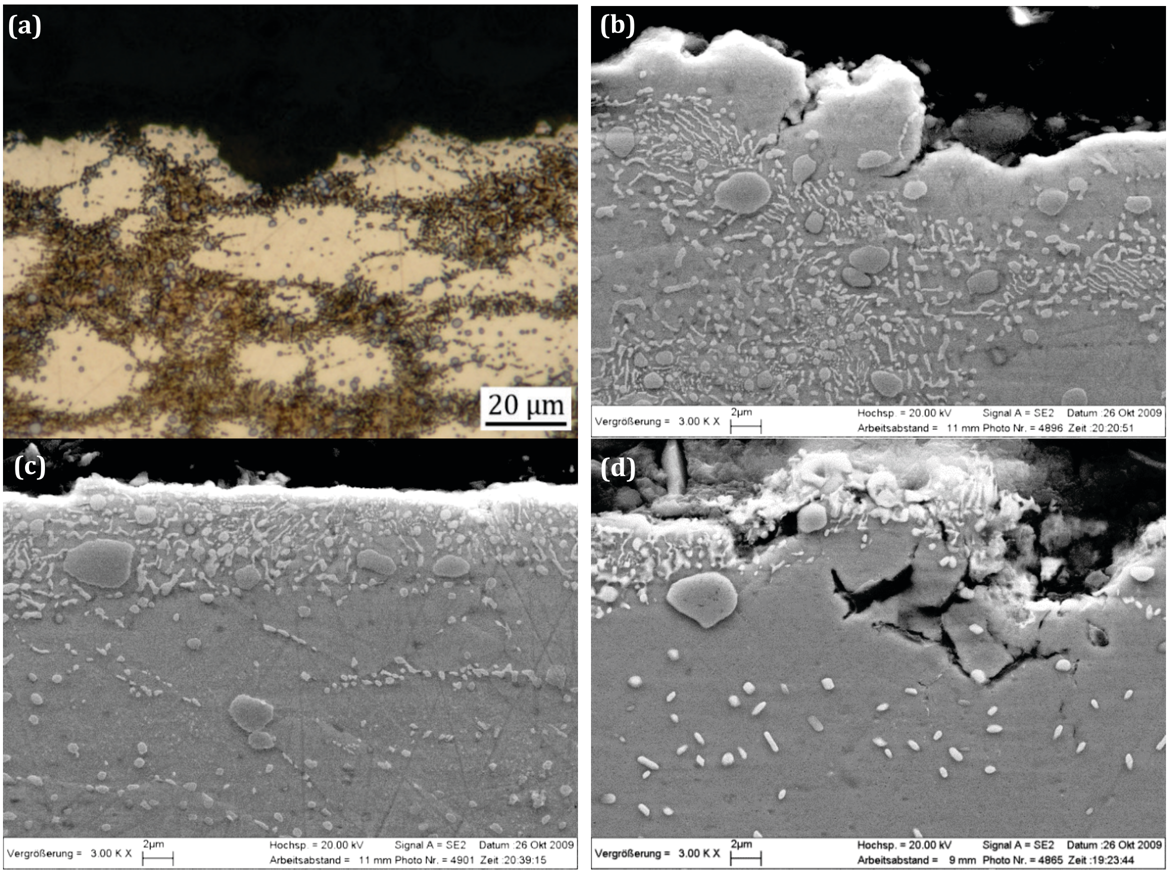

Figure 93: Cross section of worn surface of NiAl-bronze substrate after 410min cavitation duration, showing crack propagation, material removal within α-phase (a, b, d) and stabilising effect of precipitates (c).

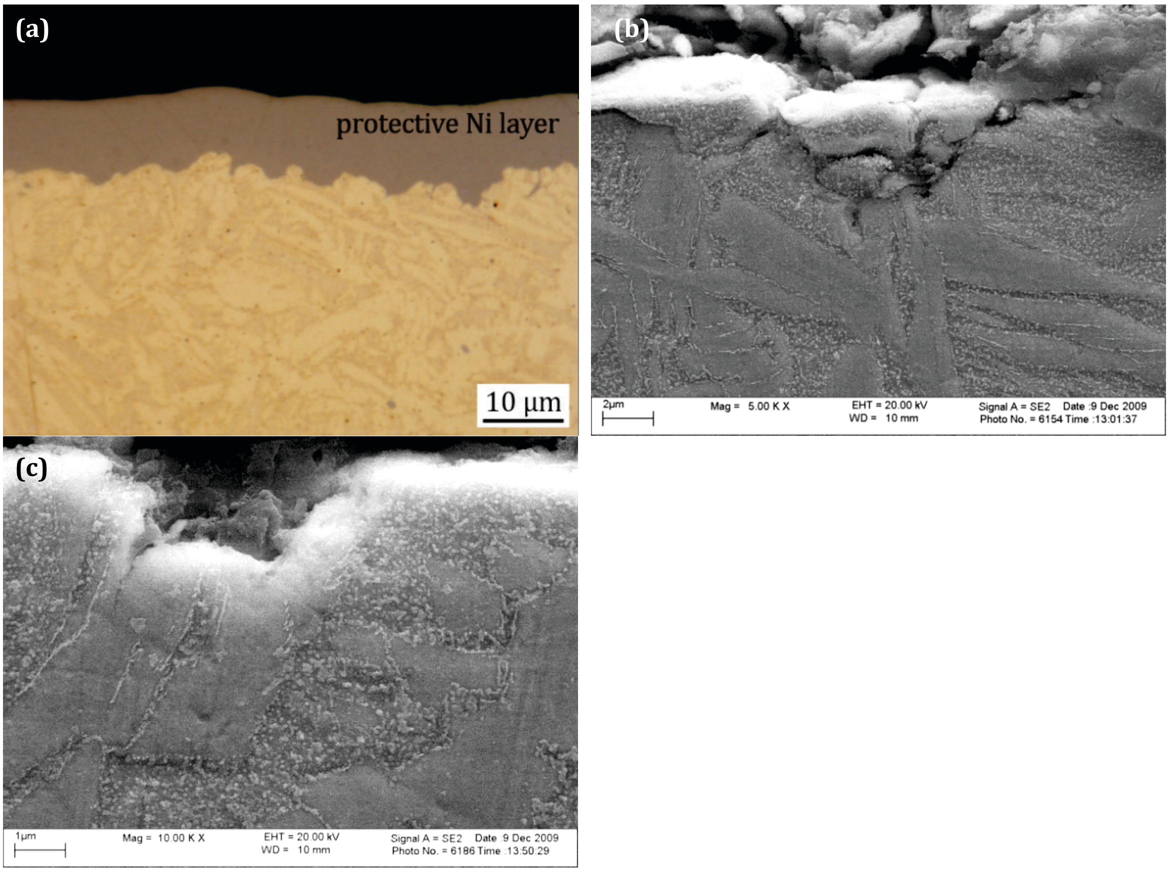

Figure 94: Cross section through worn surface of a NiAl-bronze FS coating after 410min cavitation duration. Visible are roughening of the surface (a), crack formation (b) and removal of α-phase (c).

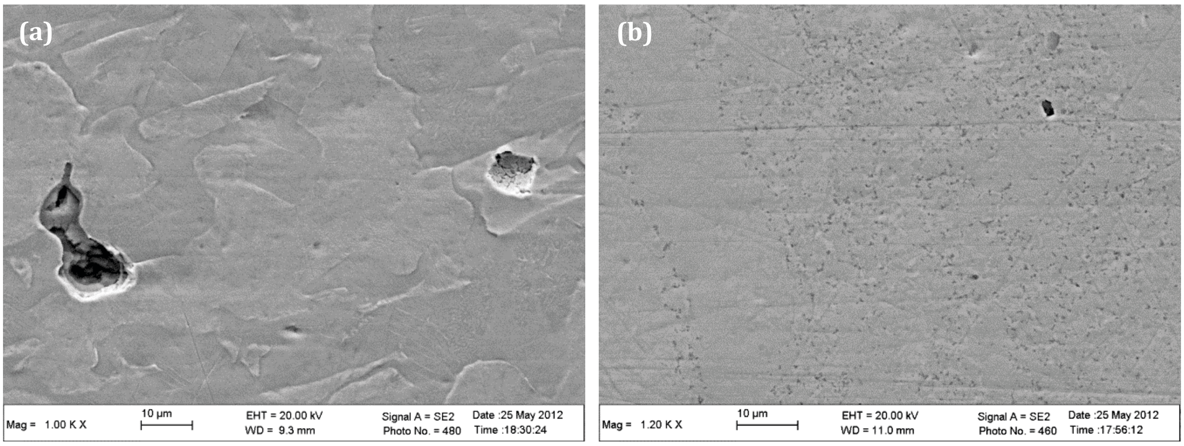

Figure 95: Worn Cr60Ni40 surface after 45 min of cavitation, (a) cast and heat treated state and (b) coating.

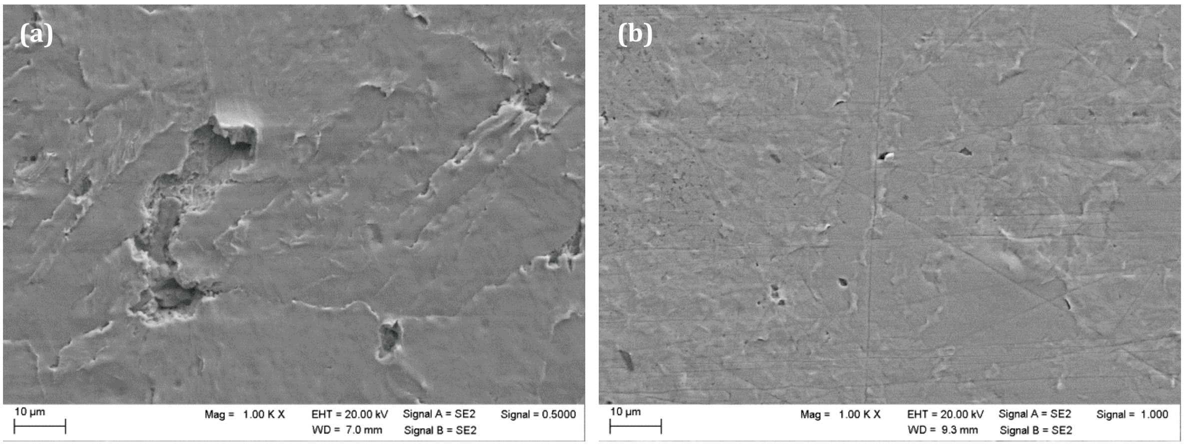

Figure 96: Worn Cr60Ni40 surface after 120 min of cavitation, (a) cast and heat treated state and (b) coating.

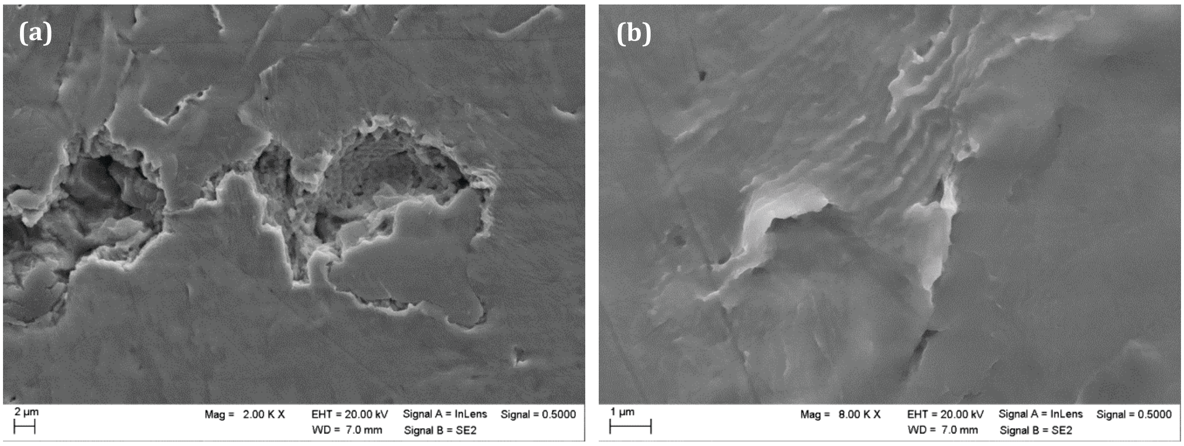

Figure 97: Worn Cr60Ni40 surface after 120 min of cavitation on cast and heat treated sample.

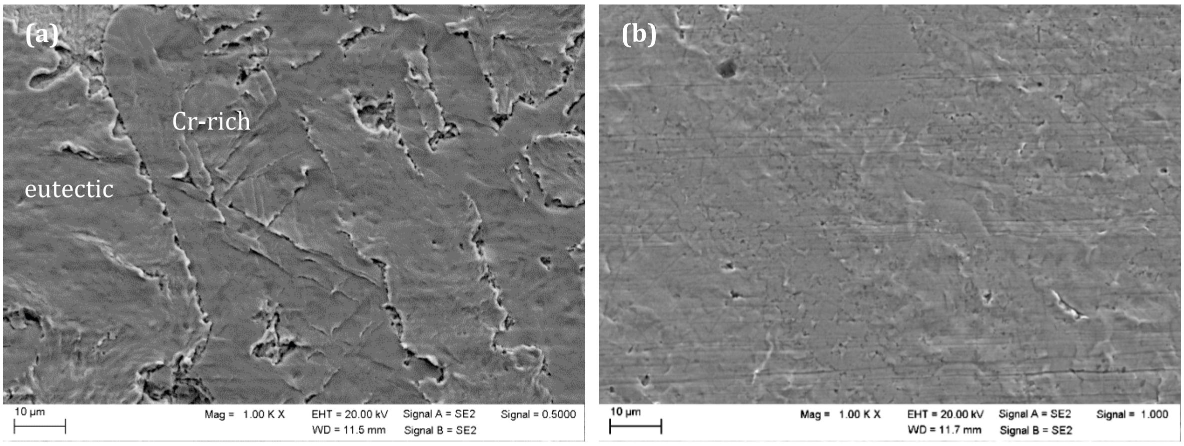

Figure 98: Worn Cr60Ni40 surface after 180 min of cavitation, (a) cast and heat treated state and (b) coating.

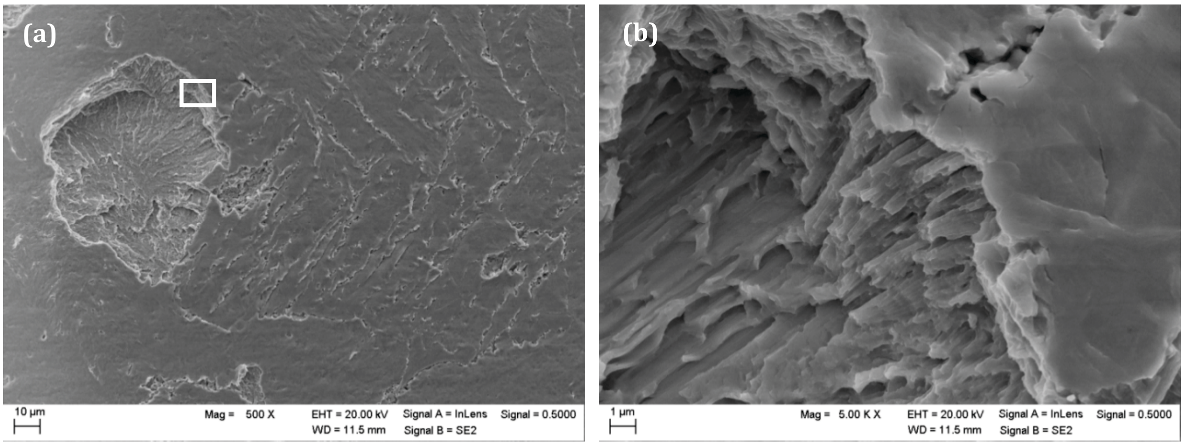

Figure 99: Worn Cr60Ni40 surface after 180 min of cavitation on a cast and heat treated sample, (b) showing a detail of (a).

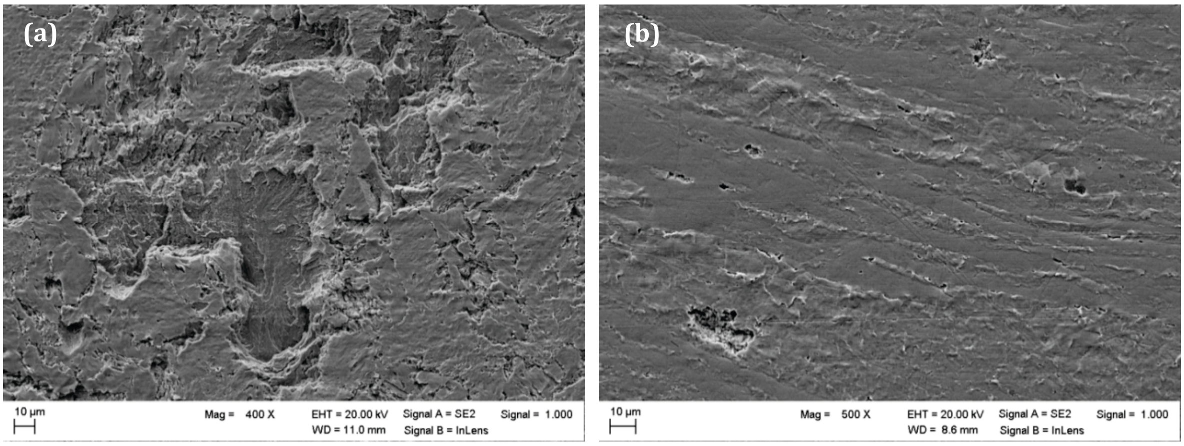

Figure 100: Worn Cr60Ni40 surface after 300 min of cavitation, (a) cast and heat treated state and (b) coating.

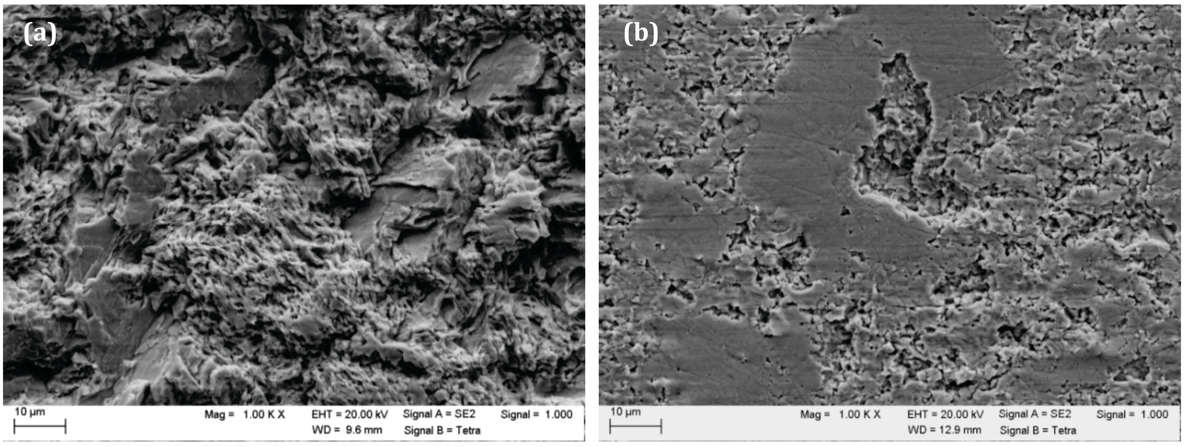

Figure 101: Worn Cr60Ni40 surface after 540 min of cavitation, (a) cast and heat treated state and (b) coating.

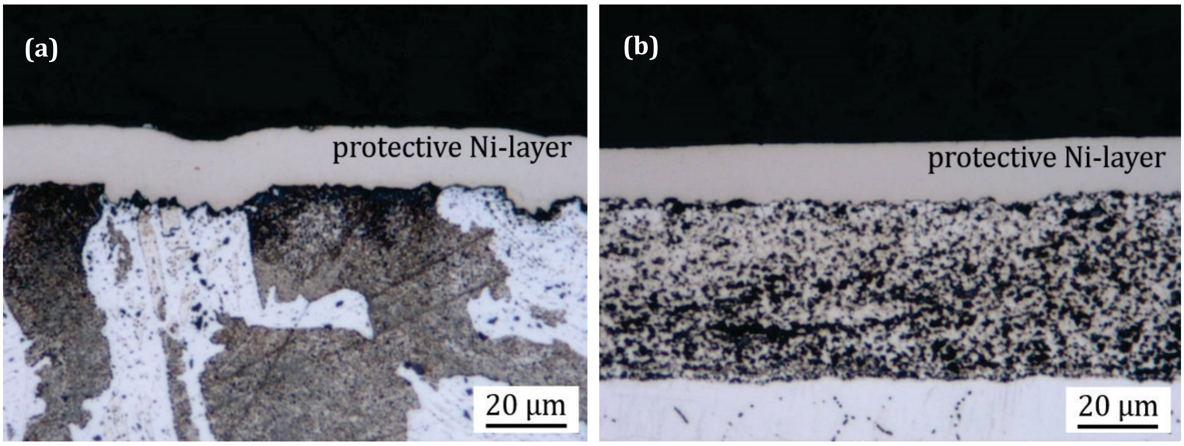

Figure 102: Cross sections through worn Cr60Ni40 surfaces after 600 min of cavitation, (a) cast and heat treated state and (b) coating.

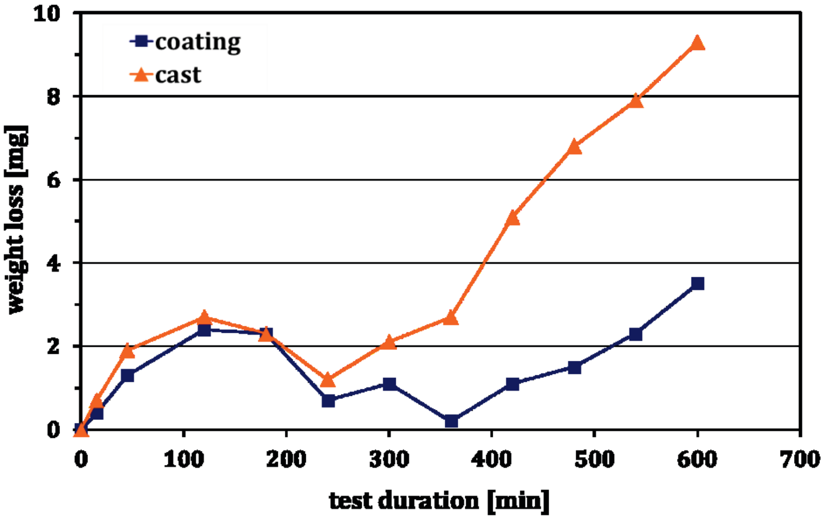

Figure 103: Progression of weight loss during cavitation for a cast and heat treated and a coated sample from Cr60Ni40.

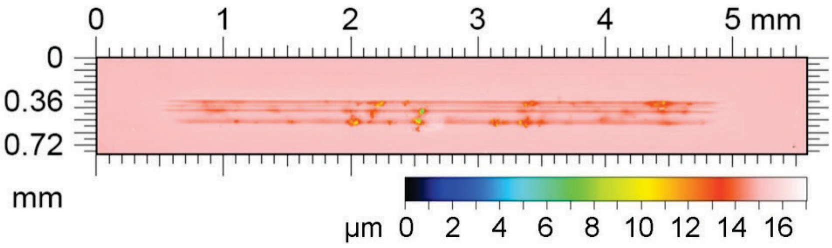

Figure 104: Sliding wear scar on cast and hardened tool steel, after 500,000 cycles at 180N normal force, measured by confocal microscopy.

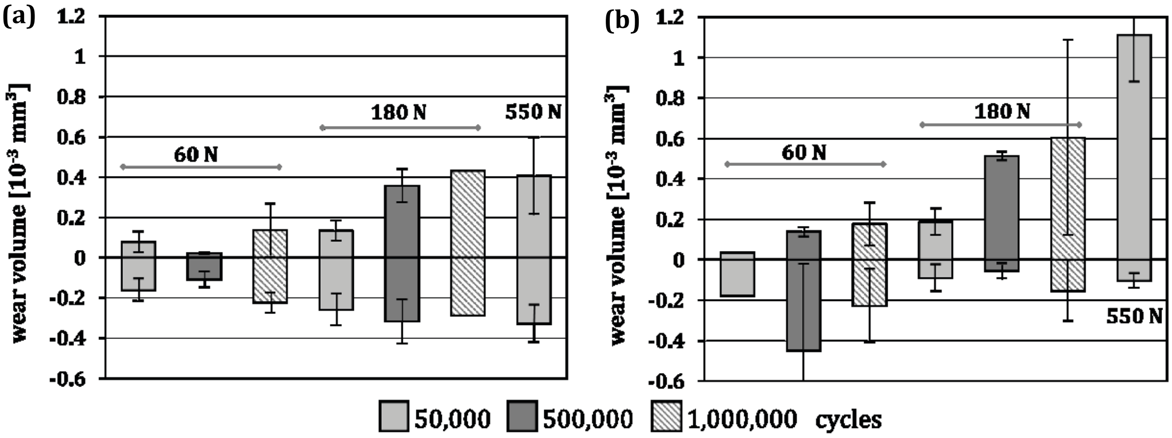

Figure 105: Wear volumes on (a) cast and hardened and (b) coated steel samples for various normal forces and numbers of cycles.

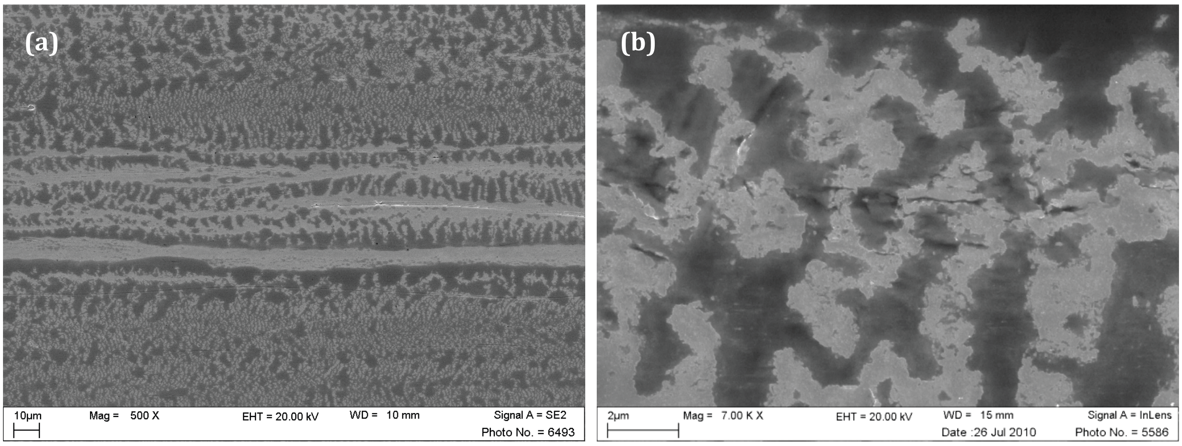

Figure 106: Worn surfaces on steel samples. Wear test at 60 N and 1 million cycles on FS coating (a) and at 60 N and 500,000 cycles on cast and hardened material (b). Visible are tribochemical layers and deformation of surface material.

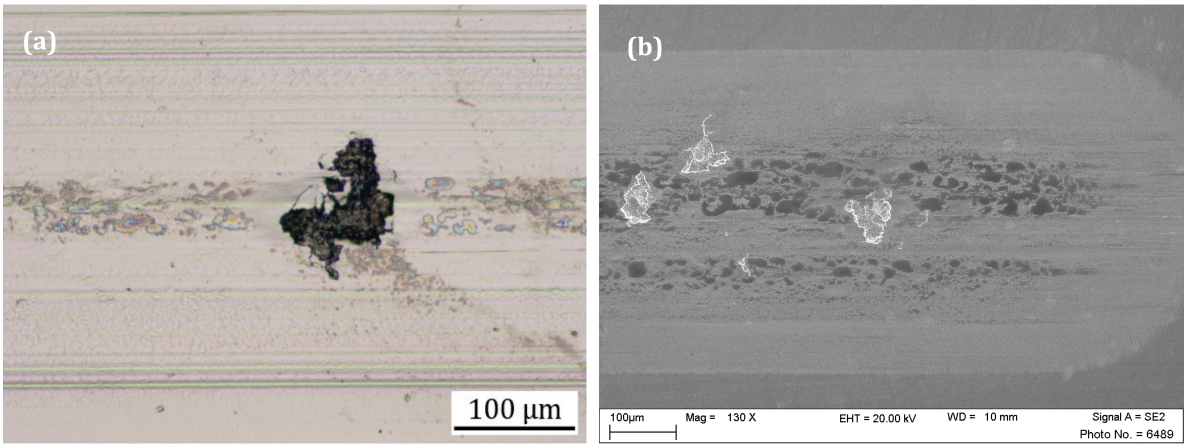

Figure 107: Worn surfaces on samples with FS steel coating. Both wear tests at 180 N and 500,000 cycles (a), (b). Delaminations, tribochemical layers and grooves are visible.

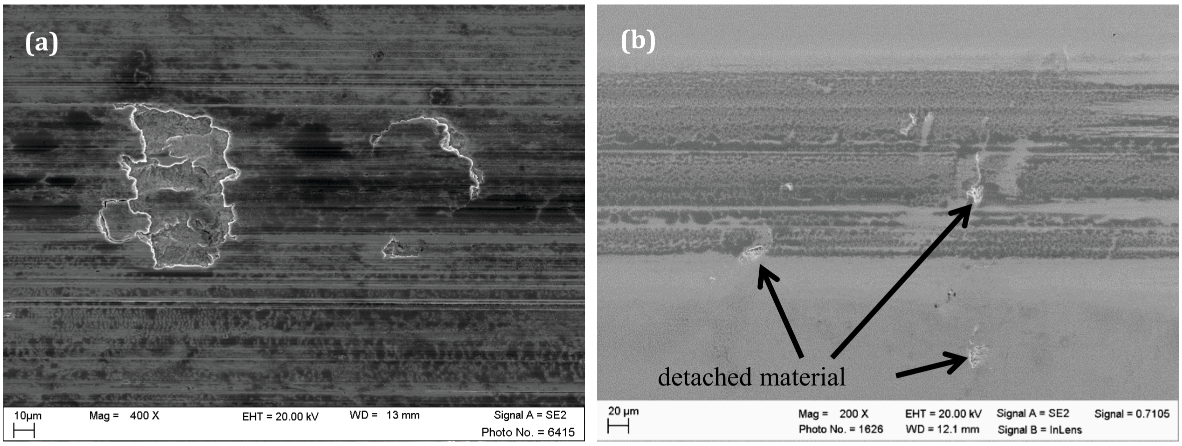

Figure 108: Worn surfaces on samples with FS steel coating. Wear test at 180 N and 50,000 cycles (a) and at 30 N and 15,000 cycles (b). Crack growth preceding a delamination can be observed in (a). In (b), small superficial defects in the FS coating are visible, not caused by the wear test.

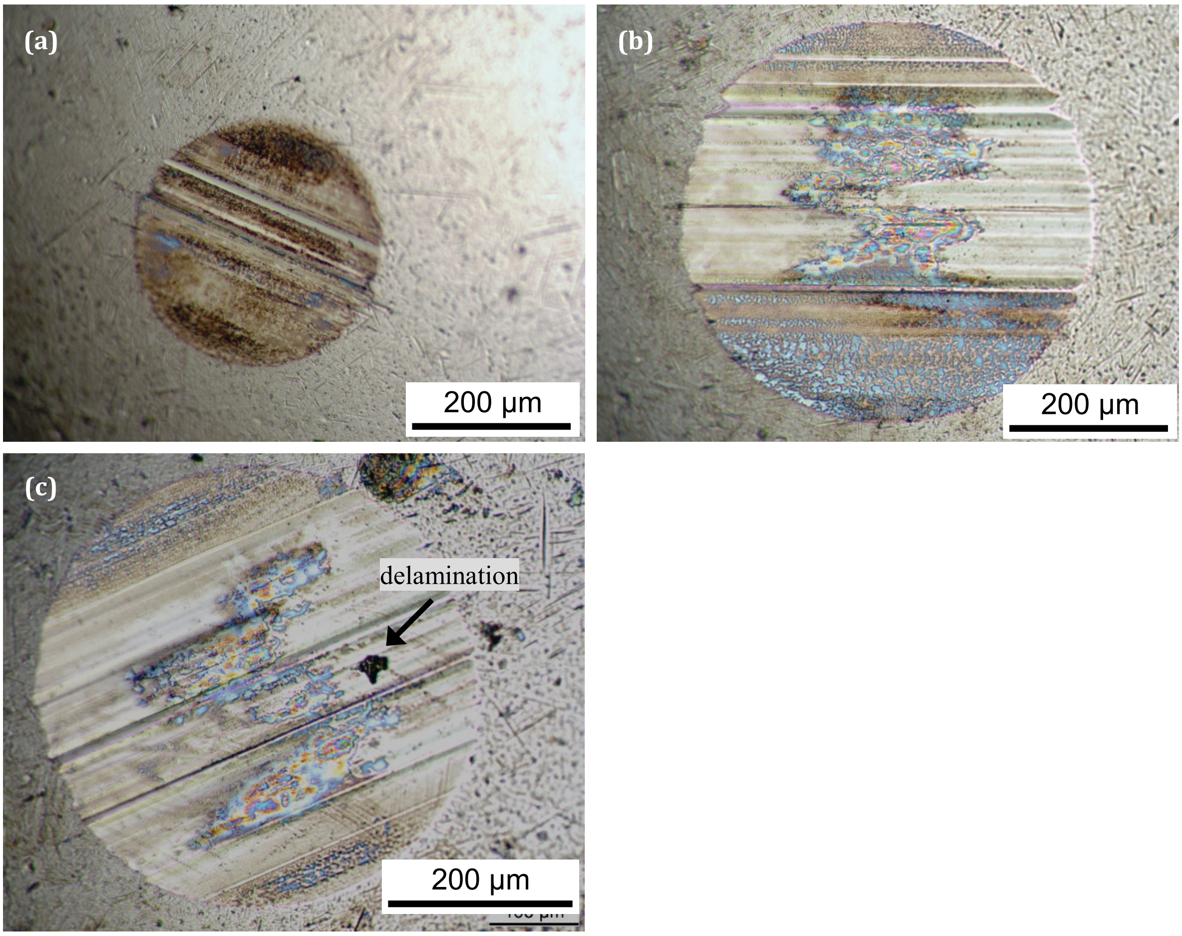

Figure 109: Worn surfaces on balls from wear test with 60 N and 500,000 cycles on cast and hardened steel (a) and from wear tests with 180N and 1,000,000 cycles on FS coated steel samples (b and c). Abrasive grooves, tribochemical layers and a delamination are visible.

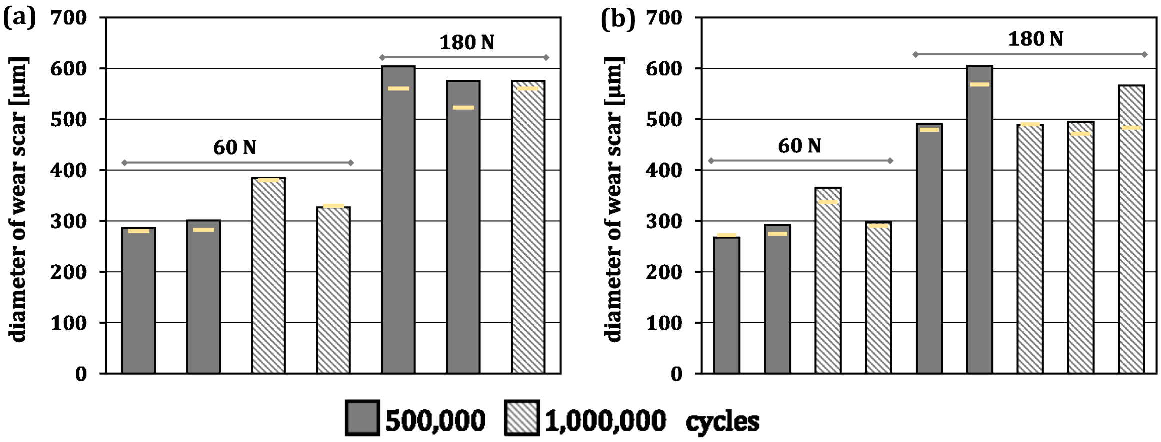

Figure 110: Diameter of wear scars on balls after sliding against cast and hardened (a) and FS coated steel samples (b) for two normal forces and numbers of cycles.

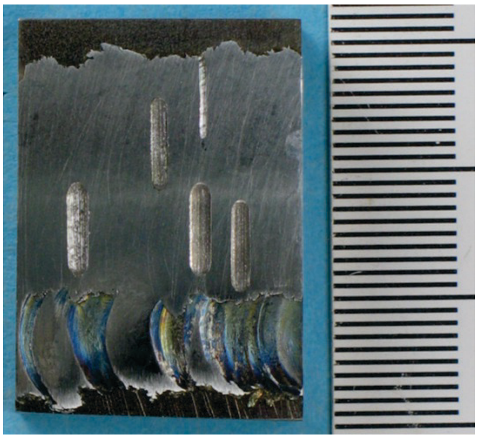

Figure 111: Sample with triple layer Cr60Ni40 coating after wear tests.

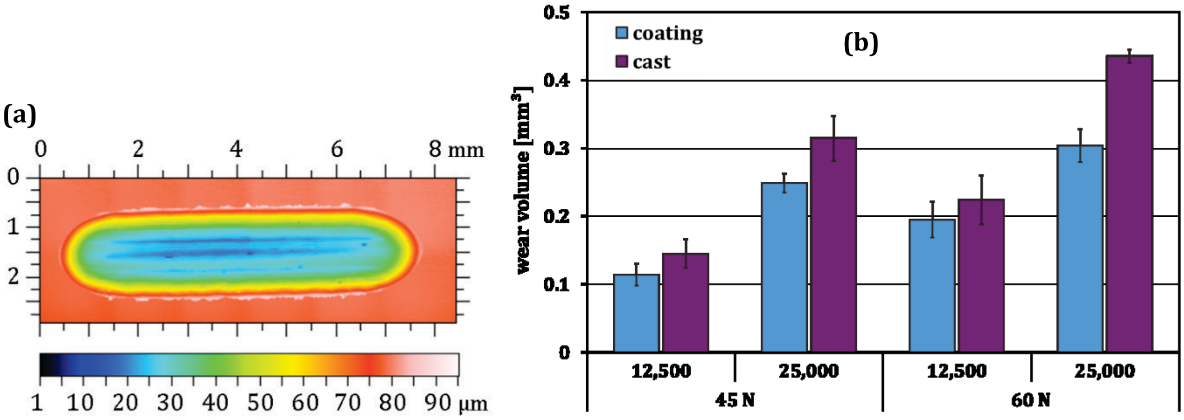

Figure 112: (a) Wear scar on cast Cr60Ni40 measured by confocal light microscopy (60 N; 25,000 cycles), the colour scale defining the height of surface points; (b) Wear volumes of the flats, determined by confocal microscopy, for 12,500 and 25,000 cycle tests.

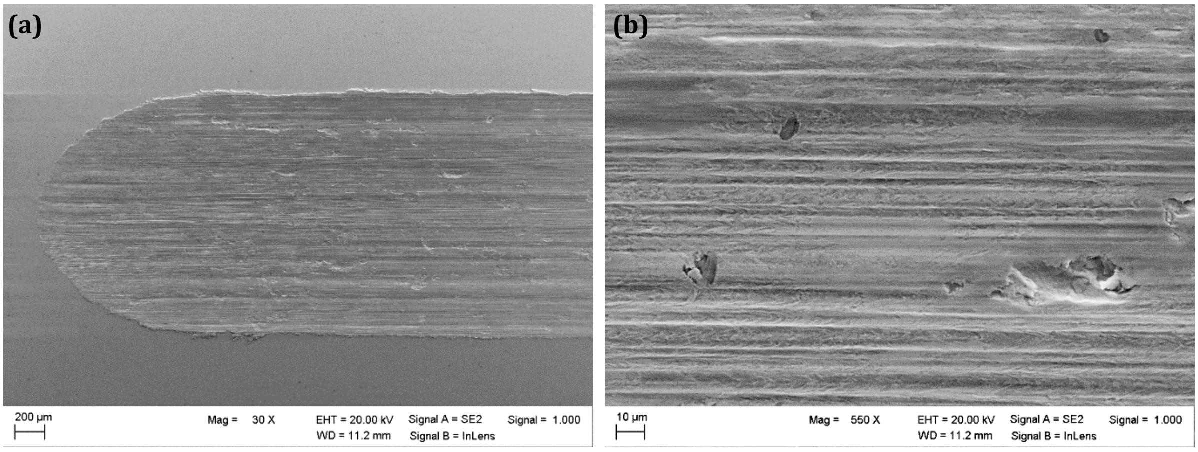

Figure 113: SEM images of worn surface on cast Cr60Ni40 (60N; 25,000 cycles): grooves and delaminations.

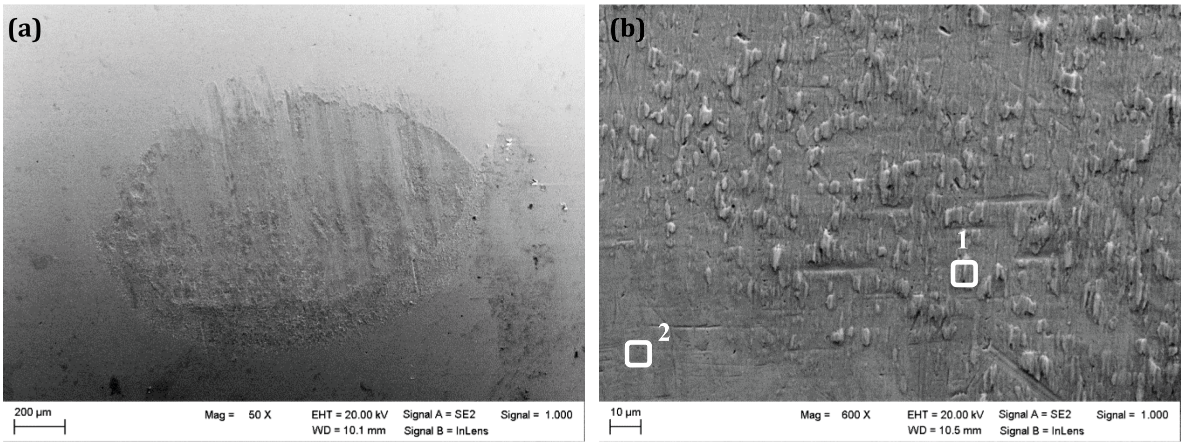

Figure 114: SEM images of worn surface on the ball corresponding to the flat in Figure 72: grooves and adhering material. EDS measurements reveal increased amounts of Cr and Ni in area (1), compared to area (2) indicated in (b). Complete measured values are given in Table 7.

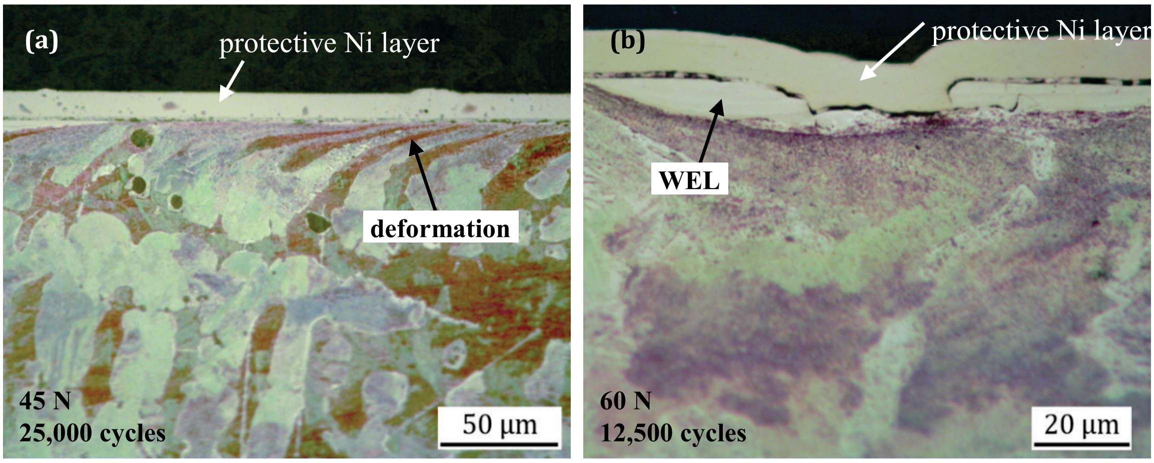

Figure 115: Cross sections of cast Cr60Ni40 after wear testing, cut parallel to the sliding direction: deformation underneath the worn surface (a) and partly delaminated white etching layer (WEL) (b).

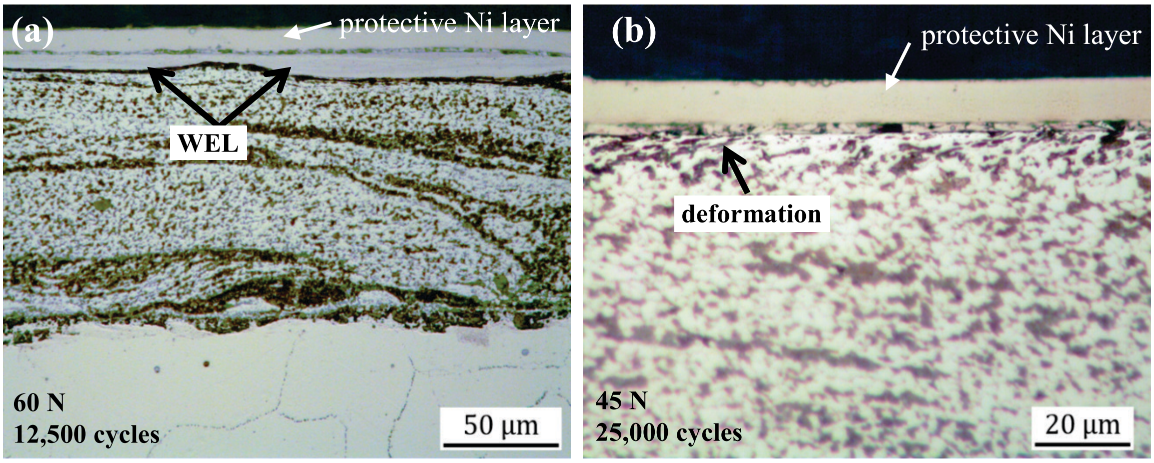

Figure 116: Cross sections of Cr60Ni40 friction surfacing coating after wear testing, cut parallel to the sliding direction: extensive white etching layers (a) and narrow region of deformed material underneath the worn surface (b).

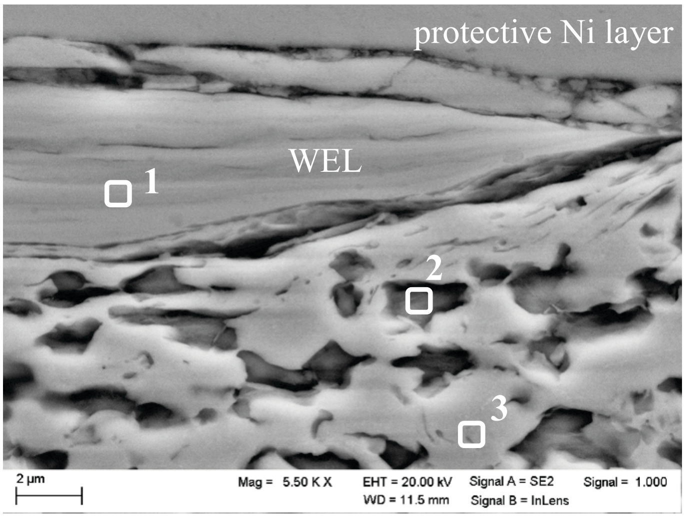

Figure 117: SEM image of cross section through worn surface on Cr60Ni40 FS coating (60N, 12,500 cycles), showing part of a white etching layer. EDS measurements reveal that the Cr:Ni ratio in the WEL (1) corresponds to the Ni-dominated phase regions (3) rather than the Cr-rich ones (2). Full results are given in Table 8.

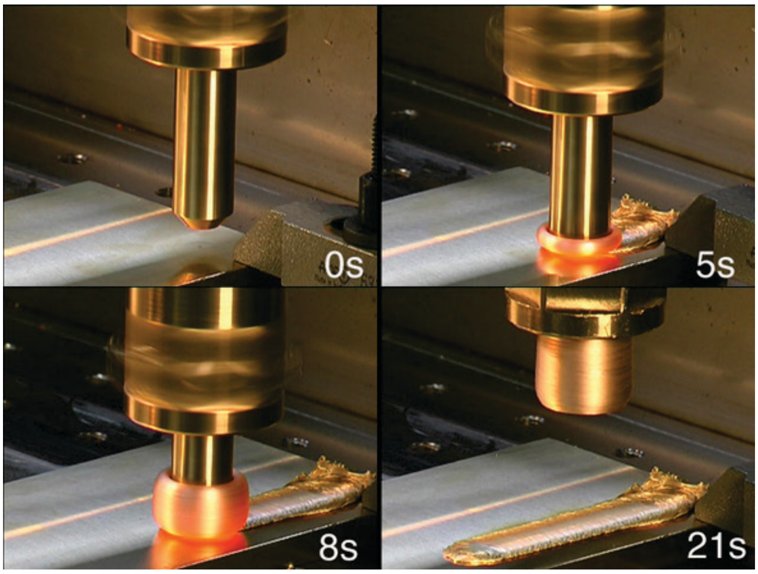

Figure 118: Friction Surfacing process of NiAl-bronze at HZG Geesthacht, photographs taken at different process times, as indicated in the bottom right corners of each image.

7.2 Tables

Si	Fe	Cu	Mn	Mg	Cr	Zn	Ti	others	Al
0.7-1.3	0.5	0.1	0.4-1.0	0.6-1.2	0.25	0.2	0.1	0.15	bal.

Table 1: Chemical composition of 6082 aluminum alloy [65].

Substrate						
Cu	Al	Fe	Ni	Mn	Si	P, Pb, Zn, Sn
81.60	10.10	4.01	3.78	0.30	0.16	
Studs						
Cu	Al	Fe	Ni	Mn	Si	P, Pb, Zn, Sn
80.90	10.20	4.60	3.77	0.27	0.17	

Table 2: Chemical composition of the NiAl-Bronze as substrate and stud materials.

C	Mn	Si	S	P	N	Fe	Ti	Al	Cr	Ni
< 0.1	< 1.0	< 1.0	< 0.2	< 0.2	< 0.3	< 1.0	< 0.5	< 0.25	58.0-62.0	bal.
tensile strength > 760 MPa (110 ksi)						yield strength > 590 MPa (85 ksi)				

Table 3: Chemical composition and properties of Cr60Ni40 according to ASTM 560/A 560 M [80].

	rotational speed [min^{-1}]	translational speed [m/min]	axial pressure [MPa]	stud diameter [mm]
6082 AA	3500	0.67	18.5	20
NiAl-Bronze	3000-4000	0.33	50	20
CP4M steel	3000-4000	0.33	109	15.3
Cr60Ni40	3500	0.33	89	20.3

Table 4: Friction surfacing process parameters for the different materials.

Cavitation		Sliding Wear		
		CP4M tool steel		Cr60Ni40
frequency	20 kHz	frequency	6 Hz	6 Hz
amplitude	19 µm	amplitude	2 mm	3 mm
temperature	25 ± 3 °C	Ø sliding speed	2.9 m/min	4.3 m/min
medium	H2O, distilled	normal forces (Hertz' mean contact pressure)	60 N (1,230 MPa) 180 N (1,770 MPa) 550 N (2,570 MPa)	45 N (1,110 MPa) 60 N (1,220 MPa)
loaded area	Ø 16 mm	numbers of cycles	50,000 500,000 1,000,000	12,500 25,000
various test times		lubricant	Anticorit PL 3802 39 S	Silicon Oil
		counterbody	100Cr6 bearing ball	
			Ø 10 mm	
			polished	

Table 5: Overview on wear testing parameters.

	area 1	area 2	area 3	area 4	area 5
C	1.7	2.0	2.0	0.9	1.2
O	23.8	19.0	1.1	29.4	1.1
Si	-	0.1	0.3	17.3	0.5
S	-	-	-	1.6	-
Ti	-	-	-	0.9	-
Cr	57.6	52.2	47.0	40.8	48.4
Mn	15.9	11.6	-	8.4	-
Fe	-	-	1.5	-	1.5
Ni	1.0	15.1	48.1	0.7	47.2

Table 6: EDS measurements as designated in Figure 47 (a) and (b), in wt.%.

	area 1	area 2
C	5.9	6.6
O	4.6	0.0
Si	4.7	1.6
Cr	27.1	2.3
Mn	0.6	0.3
Fe	33.1	88.3
Ni	24.0	0.9

Table 7: EDS measurements as designated in Figure 114 (b), in wt.%.

	area 1	area 2	area 3
C	4.6	10.3	2.8
O	5.1	4.6	1.8
Si	6.1	1.9	0.5
Cr	46.0	51.1	49.1
Fe	1.4	1.2	1.4
Ni	36.8	30.9	44.4
Cr : Ni ratio	55:45	62:38	53:47

Table 8: EDS measurements as designated in Figure 117, in wt.%.

8 References

[1] A. Manzat, A. Killinger, R. Gadow, Application of HVOF for high performance cylinder liner coatings, Ceramic Engineering and Science Proceedings 32/3 (2011) 51-58.

[2] K. Bobzin, F. Ernst J. Zwick, T. Schlaefer, D. Cook, K. Nassenstein, A. Schwenk, F. Schreiber, T. Wenz, G. Flores, M. Hahn, Coating bores of light metal engine blocks with a nanocomposite material using the plasma transferred wire arc thermal spray process, Journal of Thermal Spray Technology 17/3 (2008) 344-351.

[3] J.P. Bergmann, R. Schuerer, K. Ritter, Friction stir welding of tailored blanks of aluminum and magnesium alloys, Key Engineering Materials 549 (2013) 492-499.

[4] W. Homberg, A.E. Tekkaya, C. Beerwald, A. Brosius, J. Dau, M. Trompeter, Multifunctional lightweight structures from tailored cladded blanks, Key Engineering Materials 410-411 (2009) 37-42.

[5] S. Hollner, B. Fournier, J. Le Pendu, T. Cozzika, I. Tournié, J.-C. Brachet, A. Pineau, High-temperature mechanical properties improvement on modified 9Cr-1Mo martensitic steel through thermomechanical treatments, Journal of Nuclear Materials 405/2 (2010) 101-108.

[6] A. Nuraini, S.N. Aqida, Optimization of quenching process in hot press forming of 22MnB5 steel for high strength properties, IOP Conf. Series: Materials Science and Engineering 50 (2013) 012064.

[7] P. Berlet, M. Dienwiebel, M. Scherge, The effect of sample finishing on the tribology of metal/metal lubricated contacts, Wear 268/11–12 (2010) 1518–1523.

[8] C.A.W. Olea, L. Roldo, T.R. Strohaecker, J.F. Dos Santos, Friction stir welding of precipitate hardenable aluminium alloys: A Review, Welding in the World 50/11-12 (2006) 78-87.

[9] P.L. Threadgill, R. Johnson, The potential for friction stir welding in oil and gas applications, Proceedings of the International Offshore and Polar Engineering Conference 2004, Pages 1-7, ISSN: 10986189.

[10] G. Çam, Friction stir welded structural materials: Beyond Al-alloys, International Materials Reviews 56/1 (2011) 1-48.

[11] H. Klopstock, A.R. Neelands, An improved method of joining or welding metals, patent GB00572789, 17.10.1941.

[12] S. Hanke, A. Fischer, M. Beyer, J. dos Santos, Cavitation erosion of NiAl-bronze layers generated by friction surfacing, Wear 273/1 (2011) 32-37

[13] S. Hanke, M. Beyer, A. Silvonen, J.F. dos Santos, A. Fischer, Cavitation erosion of Cr60Ni40 coatings generated by friction surfacing, Wear 301/1–2 (2013) 415–423.

[14] M. Chandrasekaran, A.W. Batchelor, S. Jana, Study of the interfacial phenomena during friction surfacing of aluminium with steels, Journal of Materials Science 32 (1997) 6055-6062

[15] A.W. Batchelor, S. Jana, C.P. Koh, C.S. Tan, The effect of metal type and multi-layering on friction surfacing, Journal of Materials Processing Technology 57 (1996) 172-182

[16] E.I. Pluzhnikova, E.L. Demina, V.Y. Kershenbaum, G.K. Schreiber, Friction Facing of cast iron on steel, Metallovedenie i Termicheskaya Obrabotka Metallov 11 (1971) 46-47.

[17] S.B. Dunkerton, W.M. Thomas, The deposition of hardfacing and corrosion resistant materials by friction surfacing, In: Proc. 2nd Int. Conf. on surface eng., Weld. Inst. Abington Hall, Abington Cambridge (1987) 375-386.

[18] G.M. Bedford, Friction surfacing for wear applications, Metals and Materials 6/11 (1990) 702-705.

[19] P.L. Threadgill, W.M. Thomas, Manufacture of metal matrix composites clad layers during friction surfacing: preliminary studies, In: Eurojoin 1: First European Conference on Joining Technology (1991) 433-440.

[20] M. Chandrasekaran, A.W. Batchelor, S. Jana, Friction surfacing of metal coatings on steel and aluminum substrate, Journal of Materials Processing Technology 72 (1997) 446-452.

[21] J. Li, T. Shinoda, Eigenschaften reibauftraggeschweißter Schneidenkanten, Schweissen & Schneiden 52/5 (2000) 278-281.

[22] H. Sakihama, H. Tokisue, K. Katoh, Mechanical properties of friction surfaced 5052 aluminum alloy, Material Transactions 44/12 (2003) 2688-2694.

[23] D. Nakama, K. Katoh, H. Tokisue, Some Characteristics of AZ31/AZ91 dissimilar Magnesium alloy deposit by friction surfacing, Materials Transactions 49/5 (2008) 1137-1141.

[24] K.A. Tyayar, Friction welding in the reconditioning of worn components, Svarochnoe Proizvodstov 1/10 (1959) 71-76.

[25] B.M. Jenkins, E.D. Doyle, Hardfacing by low-pressure friction surfacing, Transactions of the Institution of Engineers, Australia: Mechanical Engineering 14/3 (1989) 178-185.

[26] K. Fukakusa, On the characteristics of the rotational contact plane – A fundamental study of friction surfacing, Welding International 10/7 (1996) 524-529.

[27] X.M. Liu, Z.D. Zou, Y.H. Zhang, S.Y. Qu, X.H. Wang, Transferring mechanism of the coating rod in friction surfacing, Surface & Coatings Technology 202 (2008) 1889-1894.

[28] T. Shinoda, J.Q. Li, Y. Katoh, T. Yashiro, Effect of process parameters during friction coating on properties of non-dilution coating layers, Surface Engineering 14/3 (1998) 211-216.

[29] J.Q. Li, T. Shinoda, Underwater friction surfacing, Surface Engineering 16/1 (2000) 31-35.

[30] E.D. Nicholas, W.M. Thomas, A review of friction processes for aerospace applications, Int. J. of Materials and Product Technology 13/1-2 (1998) 45-55.

[31] G.M. Bedford, V.I. Vitanov, I.I. Voutchkov, On the thermo-mechanical events during friction surfacing of high speed steels, Surface & Coatings Technology 141 (2001) 34-39.

[32] V.I. Vitanov, N. Javaid, D.J. Stephenson, Application of response surface methodology for the optimisation of micro friction surfacing process, Surface & Coatings Technology 204 (2010) 3501-3508.

[33] P. Lambrineas, P. Jewsbury, Areal coverage using friction surfacing, Journal of Ship Production 8/3 (1992) 131-136.

[34] H. Tokisue, K. Katoh, A. Toshikatsu, T. Usiyama, Mechanical properties of 5052/2017 dissimilar Aluminum alloys deposit by friction surfacing, Materials Transactions 47/3 (2006) 874-882.

[35] S. Hanke, M. Beyer, J. dos Santos, A. Fischer, Friction Surfacing of a Cold Work Tool Steel – Microstructure and Sliding Wear Behaviour, Wear 308/1–2 (2013) 180-185.

[36] T.G. Langdon, Twenty-five years of ultrafine-grained materials: Achieving exceptional properties through grain refinement, Acta Materialia 61/19 (2013) 7035-7059.

[37] R. Pippan, S. Scheriau, A. Hohenwarter, M. Hafok, Advantages and limitations of HPT: a review, Materials Science Forum 584-586 (2008) 16-21.

[38] A.P. Zhilyaev, T.G. Langdon, Using high-pressure torsion for metal processing: Fundamentals and applications, Progress in Materials Science 53 (2008) 893-979.

[39] R.Z. Valiev, R.K. Islamgaliev, I.V. Alexandrov, Bulk nanostructured materials from severe plastic deformation, Progress in Materials Science 45 (2000) 103-189.

[40] R.Z. Valiev, I.V. Alexandrov, Paradox of strength and ductility in metals processed by severe plastic deformation, Journal of Materials Research 17/1 (2002) 5-8.

[41] R. Wadsack, R. Pippan, B. Schedler, The effect of pre-deformation on the ductility of chromium, Journal of Nuclear Materials 307–311 (2002) 701–704.

[42] Z. Pakieła, H. Garbacz, Ma Lewandowska, A. Drużycka-Wiencek, M. Suś-Ryszkowska, W. Zieliński, K.J. Kurzydłowski, Structure and properties of nanomaterials produced by severe plastic deformation, Nukleonika 51/1 (2006) 19-25.

[43] N. Tsuji, Y. Saito, S. Lee, Y. Minamino, ARB (Accumulative Roll-Bonding) and other new Techniques to Produce Bulk Ultrafine Grained Materials, Advanced Engineering Materials 5/5 (2003) 338-344.

[44] T. Sakai, A. Belyakov, R. Kaibyshev, H. Miura, J.J. Jonas, Dynamic and post-dynamic recrystallization under hot, cold and severe plastic deformation, Progress in Materials Science 60 (2014) 130-207.

[45] G. Gottstein, ed., Rekristallisation metallischer Werkstoffe: Grundlagen, Analyse, Anwendung, Deutsche Gesellschaft für Materialkunde e.V. (1984) p. 67ff., p. 199ff.

[46] E. Hornbogen, H. Warlimont, Metalle: Struktur und Eigenschaften der Metalle und Legierungen 5th ed., Springer Verlag (2006) p. 154ff.

[47] E.I. Galindo-Nava, P.E.J. Rivera-Dı´az-del-Castillo, Grain size evolution during discontinuous dynamic recrystallization, Scripta Materialia 72–73 (2014) 1–4.

[48] L. Sun, K. Muszka, B.P. Wynnea, E.J. Palmiere, On the interactions between strain path reversal and dynamic recrystallization in 316L stainless steel studied by hot torsion, Materials Science & Engineering A 568 (2013) 160-170.

[49] M. Vedani, P. Bassani, A. Tuissi, G. Angella, Ultrafine Grained Alloys Produced by Severe Plastic Deformation: Issues on Microstructural Control and Mechanical Behavior, Metallurgical Science and Technology 22/2 (2004) 21-33.

[50] R. Pippan, S. Scheriau, A. Taylor, M. Hafok, A. Hohenwarter, A. Bachmaier, Saturation of Fragmentation During Severe Plastic Deformation, Annual Review of Materials Research 40 (2010) 319–343.

[51] U. Andrade, M.A. Meyers, K.S. Vecchio, A.H. Chokshi, Dynamic Recrystallization in High-Strain, High-Strain-Rate Plastic Deformation of Copper, Acta Metallurgica et Materialia 42/9 (1994) 3183-3195.

[52] K. Edalati, Z. Horita, T. Furuta, S. Kuramoto, Dynamic recrystallization and recovery during high-pressure torsion: Experimental evidence by torque measurement using ring specimens, Materials Science & Engineering A 559 (2013) 506-509.

[53] X. Quelennec, A. Menand, J.M. Le Breton, R. Pippan, X. Sauvage, Homogeneous Cu–Fe supersaturated solid solutions prepared by severe plastic deformation, Philosophical Magazine 90/9 (2010) 1179–1195.

[54] Gesellschaft für Tribologie e.V. (German Society of Tribology), Arbeitsblatt 7: Tribologie – Verschleiß, Reibung, Definitionen, Begriffe, Prüfung (2002).

[55] H. Czichos, K.H. Habig, Tribologie Handbuch 2nd ed., Vieweg Verlag (2003) p. 147ff.

[56] A. Al-Hashem, P.G. Caceres, W.T. Riad, H.M. Shalaby, Cavitation corrosion behavior of cast nickel–aluminum bronze in seawater, Corrosion 51/5 (1995) 331–342.

[57] K.R. Trethewey, T.J. Haley, C.C. Clark, Effect of ultrasonically induced cavitation on corrosion behaviour of a copper–manganese–aluminium alloy, British Corrosion Journal 23/1 (1988) 55-60.

[58] R. G. Bayer, Wear Analysis for Engineers, HNB Publishing (2002) p. 72-76 and 244-247.

[59] H. Czichos, Reibung und Verschleiß von Werkstoffen, Bauteilen und Konstruktionen, Expert Verlag (1982) p. 53-74.

[60] S. Mischler, A. Spiegel, D. Landolt, The role of passive oxide films on the degradation of steel in tribocorrosion systems, Wear 225-229 (1999) 1078-1087.

[61] A. Bidiville, M. Favero, P. Stadelmann, S. Mischler, Effect of surface chemistry on the mechanical response of metals in sliding tribocorrosion systems, Wear 263 (2007) 207-217.

[62] T.H.C. Childs, The sliding wear mechanisms of metals, mainly steels, Tribology International 13 (1980) 285-293.

[63] J. Schöfer, Tribologische Initialprozesse bei Selbstpaarungen aus dem Stahl 100Cr6 unter reversierender Gleitbeanspruchung in einem kraftstoffähnlichen Isoparaffingemisch, PhD thesis, University Karlsruhe, 2001.

[64] T. Akagaki, K. Kato, Wear mode diagram in lubricated sliding friction between carbon steels, Wear 129/2 (1989) 303-317.

[65] D. Altenpohl, Aluminium von Innen 5th ed., Aluminium-Verlag Düsseldorf (2005) p. 428.

[66] A.M. Russell, K.L. Lee, Structure-Property Relations in Nonferrous Metals, Wiley-Interscience (2005) p. 365ff.

[67] D. Altenpohl, Aluminium von Innen 5th ed., Aluminium-Verlag Düsseldorf (2005) p. 213ff.

[68] E. Hornbogen, H. Warlimont, Metalle: Struktur und Eigenschaften der Metalle und Legierungen 5th ed., Springer Verlag (2006) p. 264ff.

[69] G.A. Edwards, K. Stiller, G.L. Dunlop, M.J. Couper, The precipitation sequence in Al-Mg-Si alloys, Acta Materialia 46/11 (1998) 3893-3904.

[70] A.M. Russell, K.L. Lee, Structure-Property Relations in Nonferrous Metals, Wiley-Interscience (2005) p. 311 ff.

[71] A. Jahanafrooz, E. Hasan, G.W. Lorimer, N. Ridley, Microstructural Development in Complex Nickel-Aluminium Bronzes, Metallurgical Transactions A 14A (1983) 1951-1956.

[72] T. Kawazoe, A. Ura, M. Saito, S. Nishikido, Erosion Characteristics of Surface Hardened Ni-Al Bronze, Surface Engineering 13/1 (1997) 37-40.

[73] C.H. Tang, F.T. Cheng, H.C. Man, Improvement in Cavitation Erosion Resistance of a Copper-Based Propel-ler Alloy by Laser Surface Melting, Surface & Coatings Technology 182/2-3 (2004) 300-307.

[74] M.K. Lee, S.M. Hong, G.H. Kim, K.H. Kim, C.K. Rhee, W.W. Kim, Numerical Correlation of the Cavitation Bubble Collapse Load and Frequency with the Pitting Damage of Flame Quenched Cu-9Al-4.5Ni-4.5Fe Alloy, Materials Science and Engineering A 425/1-2 (2006) 15-21.

[75] M.W. Mahoney, W.H. Bingel, S.R. Sharma, R.S. Mishra, Microstructural Modification and Resultant Properties of Friction Stir Processed Cast NiAl Bronze, Materials Science Forum 426-432/4 (2003) 2843-2848.

[76] T.G. Gooch, Mechanical Properties of Arc Welds in Aluminium Bronze, Metal Construction 14/6 (1983) 320-329.

[77] Y. Sasaki, N. Hayami, K. Moriya, Effects of Welding Repairs on Fatigue Strength of Marine Propellers, Research and Development Kobe Steel Engineering Reports 33/3 (1983) 69-72.

[78] A. Oldewurtel, C. Escher, DE-GP4M – A new generation for tool steel casting, The use of tool steels: experience and research, in: Proc. of the 6th Int. Tooling Conference 1 (2002), Karlstad University, Sweden.

[79] W. Herda, G. L. Swales, Neue Nickel-Chrom-Legierungen mit hoher Beständigkeit gegen Brennstoffaschenkorrosion, Werkstoffe und Korrosion 19/8 (1968) 679-689.

[80] ASTM International, Standard Specification for Castings, Chromium-Nickel Alloy, ASTM 560/A 560 M, 1993.

[81] M.B. Vollaro, D.I. Potter, Phase formation in coevaporated Ni-Cr thin films, Thin Solid Films 239 (1994) 37-46.

[82] A.R. Sethuraman, R.J. De Angelis, P.J. Reucroft, Diffraction studies on Ni-Co and Ni-Cr alloy thin films, Journal of Material Research 6/4 (1991) 749-754.

[83] C. Sarbu, S.A. Rau, N. Popescu-Pogrion, M.I. Birjega, The Structure of Flash-Evaporated Cr-Ni (65:35) and Cr-Ni (50:50) Thin Films, Thin Solid Films 28 (1975) 311-322.

[84] M.I. Birjega, M. Alexe, The influence of the argon pressure and substrate temperature on the structure of r.f.-sputtered CrNi(65:35), CrNi(50:50) and CrNi(20:80) thin films, Thin Solid Films 275 (1996) 152-154.

[85] P. Nash, The Cr-Ni (Chromium-Nickel) System, Bulletin of Alloy Phase Diagrams 7/5 (1986) 466-476.

[86] L. Kaufman, H. Nesor, Calculation of the Binary Phase Diagrams of Iron, Chromium, Nickel and Cobalt, Zeitschrift für Metallkunde 64/4 (1973) 249-257.

[87] www.calphad.com/nickel-chromium.html, Computational Thermodynamics Inc., Carnegy, USA, 2006.

[88] ASTM International, Standard Test Method for Cavitation Erosion Using Vibratory Apparatus, G 32-03, 2003.

[89] DIN EN ISO 6507-1: 1998 – 01 - Metallische Werkstoffe - Härteprüfung nach Vickers - Teil 1: Prüfverfahren.

[90] E. Hornbogen, B. Skrotzki, Mikro- und Nanoskopie der Werkstoffe 3rd ed., Springer Verlag (2009).

[91] H. Oettel, H. Schumann, Metallographie 15th ed., Wiley-VHC (2011).

[92] A.M. Russell, K.L. Lee, Structure-Property Relations in Nonferrous Metals, Wiley-Interscience (2005) p. 312.

[93] G.F. Sarzhan, V.I. Trefilov, S.A. Firstov, Study of the disintegration of a supersaturated solid solution on Chromium base in the system Cr-Ni, Fiz. metal. metalloved. 31/2 (1971) 294-298.

[94] H. Hertz, Über die Berührung fester elastischer Körper, Journal für die reine und angewandte Mathematik 92 (1881) 156-171.

[95] R. Vissers, M.A. van Huis, J. Jansen, H.W. Zandbergen, C.D. Marioara, S.J. Andersen, The crystal structure of the β' phase in Al-Mg-Si alloys, Acta Materialia 55/11 (2007) 3815-3823.

[96] S. Zajac, B. Bengtsson, C. Jönsson, Influence of cooling after homogenisation and reheating to extrusion on extrudability and final properties of AA 6063 and AA6082 alloys, Materials Science Forum 396-402/1 (2002) 399-404.

[97] B.C. Shang, Z.M. Yin, G. Wang, B. Liu, Z.Q. Huang, Investigation of quench sensitivity and transformation kinetics during isothermal treatment in 6082 aluminum alloy, Materials and Design 32 (2011) 3818-3822.

[98] G. Mrowka-Nowotnik, J. Sieniawski, Influence of heat treatment on the microstructure and mechanical properties of 6005 and 6082 aluminium alloys, Journal of Materials Processing Technology 162-163 (2005) 367-372.

[99] B. Milkereit, N. Wanderka, C. Schick, O. Kessler, Continuous cooling precipitation diagrams of Al-Mg-Si alloys, Materials Science and Engineering A 550 (2012) 87-96.

[100] J. Zrnik, L. Kraus, S. Scheriau, R. Pippan, M. Ciesar, Characterization of deformation behaviour of aluminium alloy AA6082 processed by HPT, Kovove Materialy 50 (2012) 319-325.

[101] J. Gandra, D. Pereira, R.M. Miranda, R.J.C. Silva, P. Vilaca, Deposition of AA6082-T6 over AA2024-T3 by friction surfacing – Mechanical and wear characterization, Surface & Coatings Technology 223 (2013) 32-40.

[102] U. Suhuddin, S. Mironov, H. Krohn, M. Beyer, J.F. dos Santos, Microstructural Evolution During Friction Surfacing of Dissimilar Aluminum Alloys, Metallurgical and Materials Transactions A 43 (2012) 5224-5231.

[103] E.A. El-Danaf, M.M. El-Rayes, Microstructure and mechanical properties of friction stir welded 6082 AA in as welded and post weld heat treated conditions, Materials and Design 46 (2013) 561-572.

[104] H.J. McQueen, Pressure welding, solid state: role of hot deformation, Canadian Metallurgical Quarterly 51/3 (2012) 239-249.

[105] S.L. Lemanski, N. Petrinic, G.N. Nurick, Experimental Characterisation of Aluminium 6082 at Varying Temperature and Strain Rate, Strain 49 (2013) 147-157.

[106] P. Brezina, Heat treatment of complex aluminium bronzes, International Metals Reviews 27/2 (1982) 77-115.

[107] K.P. Rao, A.V. Sreenu, H.K. Rafi, M.N. Libin, K. Balasubramaniam, Tool steel and copper coatings by friction surfacing – A thermography study, Journal of Materials Processing Technology 212 (2012) 402-407.

[108] S. Hanke, M. Beyer, J. dos Santos, A. Fischer, Microstructure and Properties of Self-Mating Coatings on Cold Work Tool Steel Generated by Friction Surfacing, in: Developing the World of Tooling, Proc. of the 9th Int. Tooling Conference, Leoben, Austria, (2012) 563-570.

[109] R. Kossowsky, Creep Behavior of Ni-Cr Lamellar Eutectic Alloy, Metallurgical Transactions 1/6 (1970) 1909-1919.

[110] G.M. Hamilton, Explicit equations for the stresses beneath a sliding spherical contact, Proc Instn Mech Engrs 197C (1983) 53-59.

[111] K. Kubota, T. Ohba, S. Morito, Frictional properties of new developed cold work tool steel for high tensile strength steel forming die, Wear 271 (2011) 2884-2889.

[112] M. Pereira, J. Duncan, W. Yan, B. Rolfe, Contact pressure evolution at the die radius in sheet metal stamping, Journal of Materials Processing Technology 209 (2009) 3532-3541.

[113] R. Zhou, I. Alali, J. Cao, Q. Wang, Experimental analysis of die wear in sheet metal forming, SAE Int. J. Mater. Manuf. 2/1 (2009) 465-471.